

Portland State University

PDXScholar

Dissertations and Theses

Dissertations and Theses

5-9-2001

Dynamic Characterization of Aluminum Softball Bats

Danny V. Lee

Portland State University

Follow this and additional works at: https://pdxscholar.library.pdx.edu/open_access_etds



Part of the [Mechanical Engineering Commons](#), and the [Sports Studies Commons](#)

Let us know how access to this document benefits you.

Recommended Citation

Lee, Danny V., "Dynamic Characterization of Aluminum Softball Bats" (2001). *Dissertations and Theses*. Paper 1727.

<https://doi.org/10.15760/etd.1726>

This Thesis is brought to you for free and open access. It has been accepted for inclusion in Dissertations and Theses by an authorized administrator of PDXScholar. Please contact us if we can make this document more accessible: pdxscholar@pdx.edu.

THESIS APPROVAL

The Abstract and thesis of Danny V. Lee for the Master of Science in Mechanical Engineering were presented May 9, 2001, and accepted by the thesis committee and the department.

COMMITTEE APPROVALS:



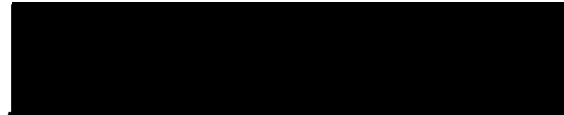
Dr. David Turcic, Chair



Dr. Graig Spolek



Dr. Gerrardo Lafferriere



DEPARTMENT APPROVAL:

Dr. Graig Spolek, Chair

Department of Mechanical Engineering

ABSTRACT

An abstract of the thesis of Danny V. Lee for the Master of Science in Mechanical Engineering presented May 9, 2001.

Title: Dynamic Characterization of Aluminum Softball Bats

On January 1, 2000, the Amateur Softball Association of America (ASA) imposed maximum bat performance limitations on commercial softball bats. The ASA adopted a testing standard defined by the American Society of Testing and Materials (ASTM) to determine the bat performance factor (BPF), a normalized coefficient of restitution that must be less than 1.2 for the bat to be eligible for ASA sanctioned events.

The ASTM standard requires that the softball strike the bat, which is free to rotate in the horizontal plane, at $26.8 \text{ m/s} \pm 0.3 \text{ m/s}$ ($88 \text{ ft/s} \pm 1 \text{ ft/s}$) with little or no spin. The central project goal was to develop the ASTM test apparatus, which consisted of a precision ball launcher, a pivoting stage for the bat, and instrumentation for velocity measurements. The key feature of the testing apparatus developed in this project was the ability to measure the rebound velocity of the ball directly—ASTM method derives the ball rebound velocity by assuming the bat behaves as a rigid body and applying conservation of angular momentum.

Tests revealed a discrepancy in the BPF between the ASTM method and an alternative method, termed the direct method, which uses the direct measurement of the ball rebound velocity. Furthermore, the ASTM method proved to be very sensitive to

parameter errors, demonstrated by magnification factors between 2.0 and 3.0. The direct method was insensitive to parameter variation with magnification factors between 0 and 1.0.

The ball rebound velocity discrepancy was also analyzed with mechanism simulation software. A three-degree-of-freedom model of the bat was used to test the effects of elasticity and pivot friction. The analysis determined that applying conservation of angular momentum on an elastic body caused transient errors in the derivation of the ball rebound velocity; and pivot friction significantly affected the motion of the bat and thus, the derived ball rebound velocity.

The experimental results show that the direct method was more accurate than the ASTM method in calculating the BPF; and the conclusion of the analytical model shows that the ASTM method can be corrected by precisely identifying external moments in the system.

DYNAMIC CHARACTERIZATION OF ALUMINUM SOFTBALL
BATS

by

DANNY V. LEE

A thesis submitted in partial fulfillment of the
requirements for the degree of

MASTER OF SCIENCE
in
MECHANICAL ENGINEERING

Portland State University
© 2001

Copyright © 2001 by Danny V. Lee

ACKNOWLEDGEMENTS

For technical, engineering questions or conversation about current events, Dr. Turcic's door was always open. On the project, Dr. Turcic gave me the freedom to pursue my ideas but stepped in to reestablish my focus when I began to stray. He guided me through the rigors of a research project with knowledge and patience, offering praise when things worked out and offering encouragement and insight when things failed. All these factors made Dr. Turcic an extraordinary advisor and mentor as well as a great friend.

I am also grateful to John Griffin for his work on the design and fabrication of the test apparatus, particularly the ball cannon. John's wealth of knowledge and practical experience proved invaluable to the project. Furthermore, John took the time to share his knowledge of machining with me, patiently explaining the advantages of the techniques he used.

I must also thank Jeff Lusardi and Dianne Park. Aside from the moral support, Jeff was a great resource for engineering problems. Jeff and Diane also allowed me to use their machine shop when the school shop was unavailable. This involved trusting me with their equipment as well as trusting me with the security code to their shop and their home. Their generosity allowed the progress of the fabrication to stay on course.

Finally, I want to thank McGuire Bearing, Pacific Machinery and Tool Steel, Familian Northwest, and Wink's Hardware. The sales staff at these Portland area vendors was extremely knowledgeable and showed a great deal of interest in my design problems.

DEDICATION

This thesis is dedicated to
My parents, Joe and Sharon, my sister Hanna, and Lara

TABLE OF CONTENTS

ACKNOWLEDGEMENTS	i
DEDICATION.....	ii
TABLE OF CONTENTS	iii
LIST OF TABLES.....	v
LIST OF FIGURES	vi
Introduction	1
Chapter 1: Design and Fabrication of Softball Bat Testing System.....	6
1.1 BALL LAUNCHER DESIGN	6
1.1.1 <i>Electromechanical Devices</i>	6
1.1.2 <i>Fluid-Actuated Devices</i>	8
1.2 DISCUSSION OF REVISION-1 CANNON.....	11
1.3 DISCUSSION OF REVISION-2 CANNON	15
1.4 DISCUSSION OF REVISION-3 CANNON.....	20
1.4.1 <i>Sabot Braking System</i>	25
1.4.2 <i>Air-Control System</i>	27
1.4.3 <i>Sabot</i>	32
1.5 BAT PIVOT STAGE	37
1.6 INSTRUMENTATION.....	43
1.7 BAT STOPPING DEVICE	48
1.8 RESULTS AND CONCLUSION.....	50
Chapter 2: Analysis and Experimental Methods.....	52
2.1 BAT CHARACTERISTICS AND EXPERIMENT SET UP.....	52
2.1.1 <i>Measurement of the Weight and Balance Point</i>	52
2.1.2 <i>Measurement of the Moment of Inertia</i>	55
2.1.3 <i>Center of Percussion (COP)</i>	59
2.1.4 <i>Equipment Layout</i>	61
2.2 MEASUREMENT OF THE COEFFICIENT OF RESTITUTION OF THE BALL	64
2.3 ASTM METHOD FOR CALCULATING THE BAT PERFORMANCE FACTOR	65
2.4 DIRECT METHOD FOR CALCULATING THE BPF	69
2.5 SENSITIVITY OF THE BPF TO MEASUREMENT AND PARAMETER ERRORS.....	75
2.6 RESULTS AND CONCLUSION	77

Chapter 3: Elastic Impact Dynamic Analysis	80
3.1 INTRODUCTION.....	80
3.2 CONJECTURES	82
3.3 IMPACT THEORY.....	82
3.4 SIMPLE MODEL.....	86
3.5 BAT MODEL	89
3.5.1 <i>Model Assembly</i>	89
3.5.2 <i>Rotational Stiffness</i>	93
3.5.3 <i>Material Damping</i>	94
3.5.4 <i>Model Verification</i>	95
3.5.5 <i>Model Simulation</i>	98
3.6 BAT MODEL WITH PIN FRICTION	105
3.6.1 <i>Friction Characterization</i>	105
3.6.2 <i>Friction Model Simulation</i>	108
3.7 ERROR AS A FUNCTION OF APPROACH VELOCITY	111
3.8 RESULTS AND CONCLUSIONS	115
Chapter 4: Summary and Conclusion	118
REFERENCES.....	122

LIST OF TABLES

Table 1.8- 1 Measured Ball Velocities.....	50
Table 2.1- 1 Balance Point Calculation for Easton Bat	54
Table 2.1- 2 Summary of Moment of Inertia Measurements	59
Table 2.1- 3 Center of Percussion of Easton Bat.....	60
Table 2.5- 1 BPF Magnification Factors for the ASTM Method	76
Table 2.5- 2 BPF Magnification Factors for the Direct Method	76
Table 2.6- 1 BPF Test Data for Easton Bat	78
Table 3.5- 1 Comparison of Experimental and Simulated Velocity Data.....	95
Table 3.6- 1 Rebound Velocity Error of Model with and without Friction	110
Table 3.8- 1 Rebound Velocity Error for Experimental and Analytical Results....	116
Table 3.8- 2 BPF Error from Experimental and Analytical Results.....	116

LIST OF FIGURES

Figure 1.2- 1 Revision-1 Cannon (foreground)	11
Figure 1.2- 2 Schematic of Revision-1 Cannon Layout.....	13
Figure 1.3- 1 Revision-2 Cannon (foreground)	15
Figure 1.3- 2 Sabot Sealing Region	16
Figure 1.3- 3 PETG Thermoformed Sabot.....	17
Figure 1.3- 4 Front End of Revision-2 Cannon.	18
Figure 1.4- 1 Revision-3 Cannon.....	20
Figure 1.4- 2 Schematic of Cannon Assembly	21
Figure 1.4- 3 Front and Back Views of Machined End -cap.....	22
Figure 1.4- 4 Rear Sealing Plate	23
Figure 1.4- 5 Jackscrew Mounting.....	24
Figure 1.4- 6 Sabot Braking System	25
Figure 1.4- 7 Cannon Shield.....	27
Figure 1.4- 8 Air Storage Tank.....	28
Figure 1.4- 9 Air Control System	29
Figure 1.4- 10 Timer Plus Relay Circuit Used for Cannon Trigger	30
Figure 1.4- 11 Solenoid Valve Trigger Console.....	31
Figure 1.4- 12 Preliminary Sabot Assembly	34
Figure 1.4- 13 Final Sabot Assembly.....	35
Figure 1.4- 14 Completed Sabot.....	36
Figure 1.5- 1 Bat Pivot Stage Diagram	37
Figure 1.5- 2 Bat Pivot Stage.....	38
Figure 1.5- 3 Pivot Shaft Assembly Diagram.....	39
Figure 1.5- 4 V-block Clamp Assembly	40
Figure 1.5- 5 Pivot Base Alignment Fence	41
Figure 1.5- 6 Pivot Base Set Up for Oscillation in Vertical Plane	42
Figure 1.6- 1 Ball Velocity Sensors.....	43
Figure 1.6- 2 Schematic of Ball Velocity Measurement.....	44
Figure 1.6- 3 Bat Velocity Sensors	45
Figure 1.6- 4 Angular Position Measurement	46
Figure 1.6- 5 Original Data Acquisition Instruments	47
Figure 1.7- 1 Bat Stopping Device	49
Figure 1.7- 2 Complete System	49

Figure 2.1- 1 Set Up for Determining Balance Point.....	53
Figure 2.1- 2 Bat Free Body Diagram.....	54
Figure 2.1- 3 Moment of Inertia of Bat Only	56
Figure 2.1- 4 Set Up for Measuring Moment of Inertia of Bat and Clamp.....	58
Figure 2.1- 5 Location of the Center of Percussion.....	60
Figure 2.1- 6 Experimental Set Up for Ball and Bat Velocity Measurements	61
Figure 2.1- 7 Ball Traveling Through the Photocells	62
Figure 2.1- 8 Typical Ball Photocell Signal	63
Figure 2.1- 9 Typical Bat Photocell Signal	64
 Figure 3.1- 1 Variation between Measured and Calculated Ball Rebound Velocity Versus Approach Velocity.....	 81
 Figure 3.4- 1 Schematic of Simple Impact Model.....	 86
Figure 3.4- 2 Screen Shot of Working Model Simulation of the Simple Impact Model.....	88
 Figure 3.5- 1 Partitioning the Bat for the Elastic Model.....	 89
Figure 3.5- 2 Working Model Vertical Swing Test Simulation	91
Figure 3.5- 3 Schematic of Elastic Bat Model.....	91
Figure 3.5- 4 Rotational Stiffness Beam Model	93
Figure 3.5- 5 Components of Angular Momentum in Elastic Model.....	97
Figure 3.5- 6 Difference in Angular Momentum of Elastic Model	97
Figure 3.5- 7 Bat Pivot Assembly Schematic.....	99
Figure 3.5- 8 Angular Momentum of Elastic Bat Model (frictionless pivot).....	100
Figure 3.5- 9 Angular Velocity of the Three Bat Sections.....	101
Figure 3.5- 10 Angular Velocity of Bat Sections at Steady State	102
Figure 3.5- 11 Comparison of Angular Position and Angular Velocity	103
 Figure 3.6- 1 Damping Calibration.....	 106
Figure 3.6- 2 Constraint Force for Fixed Axis Rotation	108
Figure 3.6- 3 Angular Momentum of Elastic Bat Model (with pin friction).....	109
 Figure 3.7- 1 Angular Velocity of Bat (with pin friction).....	 113
Figure 3.7- 2 Change in Rebound Velocity with Approach Velocity.....	114

Introduction

Since their introduction, aluminum bats have demonstrated a marked superiority to wooden bats. There were improvements in the batted ball speeds as well as batter comfort, characterized by reduced “stinging” in the hands from the impact. With competition among manufacturers, the performance of competition-grade bats continued to elevate. Bats boasted features like multiple tubing walls, internal damping layers, and lightweight composite materials. Consequently, the Amateur Softball Association of America (ASA) feared that the performance of a player would be based more on the sophistication of the player’s equipment than the player’s individual skill. The ASA was also concerned that increased batted ball speeds jeopardized the safety of softball players and spectators [2].

In response the ASA imposed a performance standard on all commercial softball bats, limiting batted ball speeds to 125 ft/s [2]. The batted ball speed is calculated from the pitch speed of the ball, the swing speed of the bat, and an additional quantity known as the bat performance factor (BPF). The BPF is the coefficient of restitution (COR) of the ball-bat system normalized by the COR of the ball alone. The bat-ball COR requires three measurements: the approach velocity of the ball, the rebound velocity of the ball, and the recoil velocity of the bat, which is initially stationary and free to pivot in the horizontal plane.

The ASA adopted a method for measuring the BPF devised by the American Society of Testing and Materials (ASTM) including prescriptions for a testing apparatus [1].

There are three main components of the testing apparatus: a high precision ball launcher, a pivoting bat-mounting stage, and instrumentation to measure the approach velocity of the ball and the recoil velocity of the bat. The principle requirements are summarized below.

- Generate a ball velocity of $26.8 \text{ m/s} \pm 3 \text{ m/s}$ ($88 \text{ ft/s} \pm 1 \text{ ft/s}$).
- Maximum ball aiming error of 3.12 mm (0.125 in.) at the point of impact.
- The ball launch device must not extinguish a match placed at the target when fired without the ball. (Avoid aerodynamic affects on the ball and bat.)
- Ball spin shall not exceed 10 rpm.
- Ball speed sensors capable of measuring an edge traveling in excess of 26.8 m/s (88 ft/s) with an accuracy of ± 1 percent.
- Bat speed sensors capable of measuring an edge traveling in excess of 4.6 m/s (15 ft/s) with an accuracy of ± 1 percent.

Currently, several commercial agencies have ASTM testing systems certified by the ASA [6]. Bat manufacturers must send prototype bats to these agencies for testing and certification. Once the testing agency verifies that the BPF of the bat is less than 1.2, the bat is stamped with an official ASA logo, deeming the bat eligible for ASA-sanctioned competition. This process is both time consuming and expensive, especially if the bat fails the BPF standard. The company that funded this project wanted an apparatus for their labs so that preliminary designs could be tested in-house. Although commercial testing systems were available, they were very expensive. Consequently, the

Portland State University Department of Mechanical Engineering was contacted to develop the apparatus for a reasonable cost.

Developing the testing apparatus was the first phase of the project, and the central design challenge was the ball launcher. The ASTM testing standard [1] did not specify the launching mechanism, but the standard did specify that conventional pitching machines—motor driven flywheels used for batting practice—were not suitable for the test. According to the funding company, agencies that perform the ASA certification use fluid-actuated cannon designs. Furthermore, a team of mechanical engineering students at Portland State University built a softball launcher for their senior project and had limited success with their pneumatic cannon design. This information indicated that a fluid-actuated cannon was an effective mechanism for the launcher.

However, fluid-actuated devices appeared to be difficult to control since the actuation involved an expansion process that varied with temperature and humidity [11]. An alternate solution would be an electromechanical system such as a linear motor or some type of conveyor system. These mechanisms could be controlled more directly by measuring the velocity and controlling the motor-generated force. Consequently, a literature search was started on electric linear actuators.

It was quickly discovered that commercially available electromechanical devices had conservative velocity limitations. Belt-driven linear motion devices were among the fastest machines with a rated top speed of 40 ft/s [16]. Additionally, wear on gears and belts could significantly affect the accuracy and repeatability of the system. More sophisticated devices, like linear motors, required complex control systems that were

out of the scope of this project, both in terms of time frame and expense. The presumed advantages of a control system were curtailed by speed limitations, complexity of the drive train, as well as complexity of the control system itself.

It was concluded that an electromechanical device was not an effective solution for the ball launcher, so the concept of a fluid-actuated cannon was revisited. A literature search on the IBM Patent Server [12] for fluid-actuated ball launchers returned only recreational, foam projectile launchers that were inappropriate for this project. General searches on the Internet returned various pneumatic cannons used for launching prizes like wadded-up t-shirts into the crowd at sporting events. Other devices included pneumatic projectile launchers employed by the military to penetrate barricades or tunnel into the earth. All these examples attested to the effectiveness of a cannon design to generate high velocities relatively quickly and with comparatively few moving parts.

The design procedure involved three revisions, with each design increasing in complexity. The first two revisions were fabricated with plastic barrels and fittings and other inexpensive, off-the-shelf parts. The purpose of the two prototypes was to get baseline statistics on the velocity variations, pressure requirements, and repeatability. The prototypes were also used to test concepts such as the effects of using a piston, or sabot, on speed and accuracy. The final revision combined the design knowledge from the first two revisions with precision materials and custom machining. The Revision-3 cannon was a fluid-actuated pneumatic cannon with the structural characteristics of

industrial hydraulic cylinders. The success of the launcher was attributable to the lightweight sabot used to cradle the ball during acceleration.

Aside from meeting all the specifications set by the ASTM standard [1], the apparatus with the Revision-3 cannon was able to measure the rebound velocity of the ball directly. Because devices currently in use are unable to measure the rebound velocity, the ASTM standard [1] utilizes conservation of angular momentum to derive the rebound velocity in terms of the other parameters. The ability to measure the rebound velocity directly revealed a discrepancy between the measured and calculated values. This discovery initiated a rigorous analysis of the ASTM procedure for calculating the BPF as well as an analytical model to study possible sources for the observed discrepancy.

Chapter 1: Design and Fabrication of Softball Bat Testing System

1.1 Ball Launcher Design

Two classes of machines were considered for the ball launcher: electromechanical devices and fluid-actuated devices. After examining the advantages and disadvantages of the two platforms, the fluid actuator proved to be a simpler and more effective solution. The final design consisted of a pneumatic cannon with the structural characteristics of a commercial hydraulic cylinder. The following discussion presents research on linear motion devices that could repeatedly and precisely generate the required velocity.

1.1.1 Electromechanical Devices

The advantage of an electromechanical device was the possibility of implementing an electronic control system. That is, the ball could be accelerated up to the desired speed, which the control system could maintain for a period of time before releasing the ball to the target, ensuring that the ball would exit the cannon at precisely 88 ft/s. Further, the entire process could be as simple as controlling the voltage sent to an electric motor. Initially, electromechanical systems demonstrated much potential. However, the performance limitations and high power requirements inhibited the viability of an electromechanical launcher.

The first electromechanical device investigated was the linear induction motor (LIM). LIMs have been used predominately for light-rail train systems, but many amusement parks have employed this technology for high-speed thrill rides. *Superman: The Escape*, designed by Intamin of Zurich, Switzerland, was the first amusement park ride to travel 100 mph, reaching this speed in only seven seconds. *Superman* used linear synchronous motors on a straight 900-foot-long track, allowing riders feel 4.5 g's when it reached the maximum speed [18]. This application demonstrated the potential of LIMs.

On a smaller scale, many factories have implemented LIMs in production lines. However, three restrictions limit their prevalence: They cannot generate as much force as other linear motion devices such as ball screws; implementing braking systems is more difficult than with conventional rotary-to-linear systems; and costs are higher than conventional rotary-to-linear devices [15]. Another factor that is not a major restriction for production lines but was important for this project is the speed limitation. LIMs operating on commercial 60 Hz AC power from a wall outlet generally have speeds in the 10 to 30 ft/s range [3].

The main reasons for dismissing LIMs as a solution were cost and time. The cost of the motor, control system, and supporting electronics would have exceeded the budget of this project. Furthermore, the time required to understand LIMs well enough to reconfigure and boost velocity would also have exceeded the scope of the project.

A simpler solution to linear motion was conveyor machines often used in manufacturing or assembly lines. These machines include conveyor belts, chain drives, wheel-rail systems, and rack and pinion systems. Manufacturer catalogs indicated,

however, that 88 ft/s was out of the working range for commercially available devices. Lead screws and ball screws have top speeds on the order of inches per second. The fastest commercially available unit was a belt-drive system with a maximum operating velocity of 40 ft/s [16]. For most applications, precise positioning of appreciable loads was a greater concern than top-end speed.

Another factor that limited the maximum speed of a device was deceleration after the ball was launched. This factor disqualified wheel-rail systems and rack and pinion systems as possible solutions. Like trains, these devices have stationary tracks and an engine that moves with the load, in contrast to belt- or chain-driven conveyors in which the engine is stationary and the belt or chain moves the load. The mass that had to be accelerated and decelerated was significantly higher in the former configuration and therefore not preferable.

Besides the performance limitations of commercially available units, these devices had the added complexity of gears or belts that could degrade over time, especially at the high speeds required for this project. Consequently, electromechanical systems had too many ambiguous factors to be considered a viable solution for the ball launcher.

1.1.2 Fluid-Actuated Devices

The attractive qualities of fluid-actuated devices were the tremendous potential energy stored in compressed fluids like air or oil and the rapid rate at which such energy can be released and transferred into useful work.

The first concept pursued involved a ball carriage mounted on the stage of a linear bearing system and accelerated by a piston-cylinder system. The appeal of this design was that all the components were commercially available, minimizing the amount of custom machining. According to a representative from Parker-Hannifin [7], a manufacturer of fluid actuators, pneumatic cylinders offered faster actuation and simpler operation than hydraulic cylinders, which are generally reserved for high-load applications.

As with electromechanical devices, commercial pneumatic cylinders had conservative speed ratings. According to a representative from SMC Pneumatics Inc. [8], the speed of that company's line of standard high-speed cylinders falls in the range of 20-50 ft/s. However, speeds can be increased somewhat by enlarging the diameter of the air-supply port and increasing the length of the cylinder. The former essentially increases the volumetric flow rate of air entering the cylinder chamber, while the latter increases the available acceleration distance. The penalty for lengthening the cylinder is that the rod must also be lengthened,¹ thus increasing the inertia to be accelerated and decelerated. Since the required speeds were higher than manufacturer ratings, the effectiveness of standard impact bracing devices, such as rubber bumpers or springs, was questionable [13]. It was concluded that a standard, commercially available, piston-cylinder system was not a viable platform for the launcher.

¹ Most piston rods are made from chromed or polished stainless steel, or other corrosion resistant steel. For example, a pneumatic cylinder with a 2-inch diameter bore and 4-foot stroke has a rod 1 inch in diameter. The total moving mass, including the aluminum piston is 13 pounds [Parker-Hannifin Actuators Catalog].

Other options were explored through patent searches on pneumatic projectile launchers. The result was an array of patents pertaining to air-powered rifles and pneumatic weapons used by the military. In these devices, the projectile itself is in direct contact with the fluid. The concept is analogous to an artillery cannon but with compressed air as the working fluid instead of the combustion of gunpowder.

The advantages to and reasons for pursuing a design based on compressed air were convenience and safety. Most laboratories have air supply lines; if not, a compressor can be purchased for \$200 to \$300. Therefore handling the fluid is relatively simple and inexpensive. Because the apparatus was to be used indoors, combustion gases could be a health risk; air, on the other hand, is harmless.

1.2 Discussion of Revision-1 Cannon

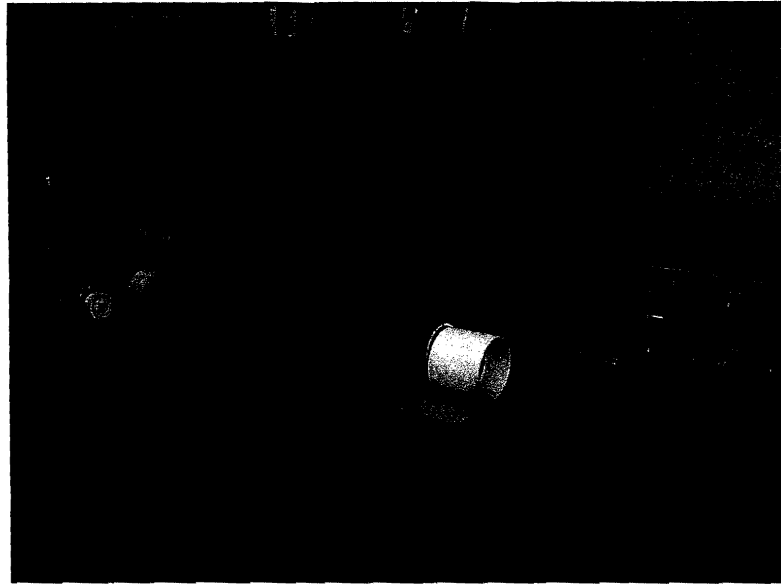


Figure 1.2- 1 Revision-1 Cannon (foreground)

The Revision-1 cannon was significantly smaller than the Revision-3 cannon shown in the background.

The Revision-1 cannon was a simple prototype used to get baseline statistics on pressure requirements, velocity variations, and reliability. The device was a pneumatic cannon similar to a design built by a team of students for their senior project at Portland State University. The design relied on finding a barrel structure with a bore that was a sliding fit for the outside diameter of a standard softball. If the bore was too large, air would leak past the ball, causing spin and velocity variation; if the bore was too small, the ball could become lodged firmly in the barrel. Revision 1 was made from schedule 80 PVC pipe with a nominal diameter of 4 inches and an actual inner diameter of 3.786

inches. Due to the variations in ball diameters, as well as variations along the length of the pipe, only certain balls would properly fit in the barrel.²

The back of the cannon was sealed with an end-cap and fitted with a 0.75-inch-port solenoid valve³ to control the airflow. A 12-volt battery with a momentary switch activated the solenoid. The system is illustrated in figure 1.2-2. Once the ball was forced down the barrel into position, the switch was triggered and the air was allowed to rush into the chamber. When the pressure behind the ball exceeded the holding force, the ball began to accelerate down the barrel. After leaving the barrel, the ball crossed a pair of photocells for velocity measurement. The speed of the ball was calculated from the distance between the photocells and the elapsed time was measured on the oscilloscope.

The Revision-1 cannon required 90 psi to reach 88 ft/s and exhibited velocity variations as high as 16 ft/s. The standard deviation over 12 shots was approximately 5 ft/s. Despite the large fluctuations, the required 50-percent success rate [1] was achieved for several testing sessions.

² A standard softball has an outside diameter of 3.75 inches with an average variation of 0.125 inches.

³ A solenoid valve uses a conductive coil (solenoid) to open/close the valve gate.

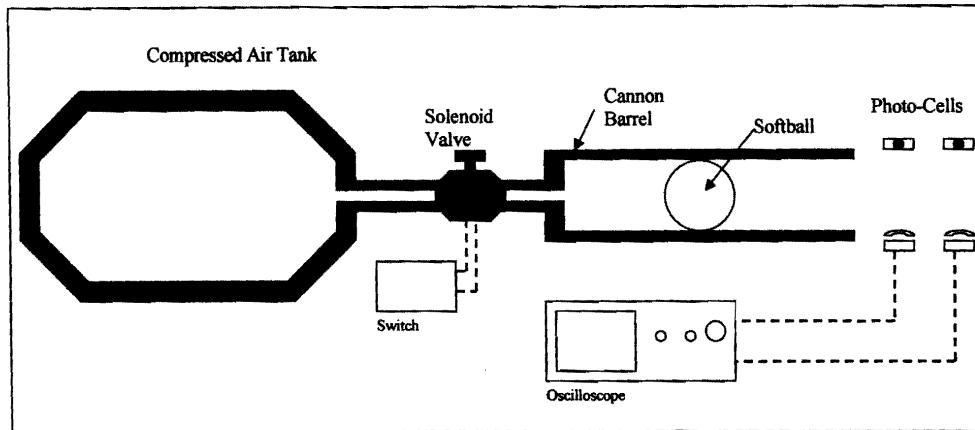


Figure 1.2- 2 Schematic of Revision-1 Cannon Layout

When the solenoid valve is opened, compressed air from the tank rushes into the barrel. The air expands forcing the ball to accelerate down the barrel. When the ball leaves the barrel, it crosses a pair of photocells where the velocity measurement is made.

These tests were done with the muzzle of the cannon approximately 1 foot from the first photocell. However, firing the cannon without the ball was equivalent to blowing air through a straw, causing the Revision-1 cannon to fail the ASTM specification that the cannon not extinguish a match, placed at the location of the bat, when the cannon is fired without a ball [1]. The Revision-1 cannon had to be positioned 8 feet from the target to prevent the exhaust air from extinguishing the match at the target. Assuming the ball maintains 88 ft/s over the 8 feet to the target, the ball drops nearly 2 inches by the time it reaches the bat due to gravity. This drop makes it more difficult to position and align the ball with the center of the bat.

Revision 1 illustrated the simplicity and functionality of a pneumatic cannon design and provided a baseline for design improvements. In summary, following issues needed to be addressed:

- The prototype could not accommodate varying ball diameters.
- The velocity variations were out of the specified tolerance.
- The cannon failed the match test; moving the cannon away from the target to satisfy the match test introduced complexity in aiming.
- The necessary working pressure of 90 psi was near the supply limit of 100 psi with the cannon stationed 1 foot from the target.

1.3 Discussion of Revision-2 Cannon



Figure 1.3- 1 Revision-2 Cannon (foreground)

The Revision-2 cannon was much larger than the Revision-3 cannon shown in the background.

To address the issues associated with Revision 1, the Revision-2 design incorporated the use of a piston, or sabot, to contain the air in the barrel after the ball exited the barrel. This allowed the cannon to be placed closer to the target, while still satisfying the match test. The sabot provided a better seal than the ball alone. A ball makes contact with the barrel only along its centerline, but a sabot makes contact with the barrel over its entire cylindrical surface area; *see* figure 1.3-2. Further, a sabot that cradled the ball eliminated contact between the ball surface and the barrel surface. This

attribute was important because relative motion between the ball and the barrel could result in rotation as well as variable friction.

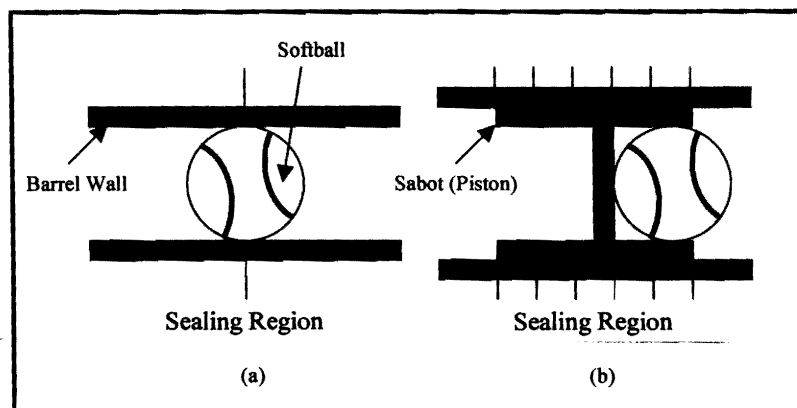


Figure 1.3- 2 Sabot Sealing Region

Comparison of effective sealing region between a ball and a cylindrical sabot. The schematic shows a longitudinal cross section of the barrel. In (a) only the equator of the ball effectively contacts or seals the chamber. In (b) the entire outer skin of the sabot contacts the barrel wall.

For an effective seal, the sabot was thermoformed using the PVC pipe as a mold. Polyethylene terephthalate glycol (PETG) was used as the forming material. The finished sabot and the mold are shown in figure 1.3-3. According to a representative from Multi-Craft Plastics, PETG is the most commonly used polymer for thermal or vacuum forming. The material has good impact resistance and is very light; the finished sabot weighed about 6 oz. The result was a cup-shaped structure with an outside diameter conforming to the pipe bore.

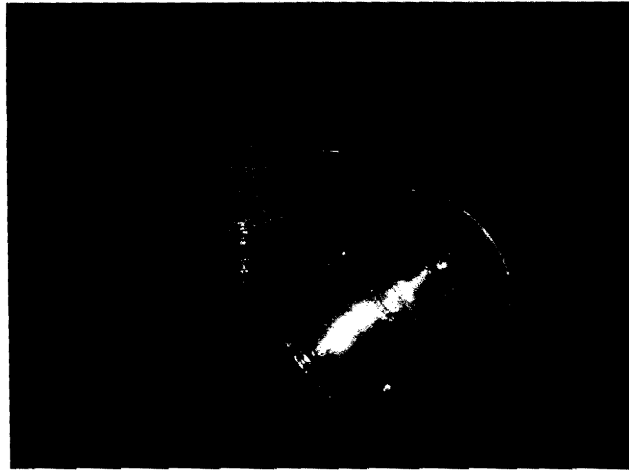


Figure 1.3- 3 PETG Thermoformed Sabot

Photograph of PETG sabot with the mold in the background. The sabot was essentially two “cups” glued bottom-to-bottom. The lower tier of the mold was a vacuum chamber.

The Revision-2 barrel was made from schedule 80 PVC with a nominal inner diameter of 6 inches and an overall length of 72 inches. As in Revision 1, the back of the barrel was sealed with a PVC end-cap and fitted with a similar 0.75-inch port solenoid valve. A threaded coupler was cemented onto the front of the barrel to accept a threaded end-cap. A hole was bored into the front of the end-cap, creating a shoulder to catch the lip of the sabot, but allow the ball to exit. Figure 1.3-4 shows a close-up of the front end of the Revision-2 cannon.

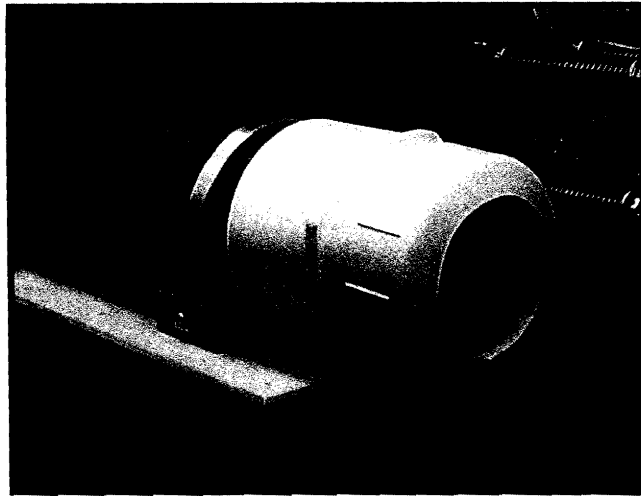


Figure 1.3- 4 Front End of Revision-2 Cannon.

Note the threaded end-cap with 4-inch bore. The end-cap served as a shoulder to stop the sabot at the mouth of the barrel. The sabot contained the air in the cannon preventing the exhaust air from reaching the target. This effectively addressed the match test.

For the first tests the front end-cap was removed, and the sabot was allowed to exit the cannon with the ball. The repeatability of Revision 2 showed significant improvement for the majority of the testing sessions, with a standard deviation of just over 3 ft/s. The larger chamber volume with the same solenoid-valve-port diameter used in Revision 1 limited the ball speed to 60 ft/s at 100 psi. To increase the flow rate, the 0.75-inch solenoid valve was replaced with a 1-inch solenoid valve, but there was no appreciable change in top speed. It was discovered that the port of the tank was still 0.75 inches. Since the smallest cross sectional area through which the air must pass limits the flow rate, larger fittings had to be installed, stemming from the outlet port of the supply tank.

Next, the cannon was tested with the front end-cap in place. After the ball left the barrel the air continued to decompress, building up pressure behind the sabot. This caused the pliable, plastic sabot to balloon out and tear. Venting was critical. It was important that vents be positioned far enough downstream to avoid hindering acceleration and far enough upstream to provide ample time for the air to exhaust.

With the insight gained from Revision 2, work on the third and final design began. The following were the conclusions from the second prototype:

- Use of a sabot provided significant improvement on repeatability.
- The deformation of the thermoformed sabot due to the pressure build-up indicated that PETG was too fragile for this application.
- A larger cylinder bore necessitated a greater flow rate. Consequently larger ports and fittings must be used stemming from the outlet port of the tank to the cannon.
- The use of a sabot necessitated air vents in the barrel, and the position of the vents must be carefully planned.
- The PVC pipe should be replaced with a precision barrel material.

1.4 Discussion of Revision-3 Cannon

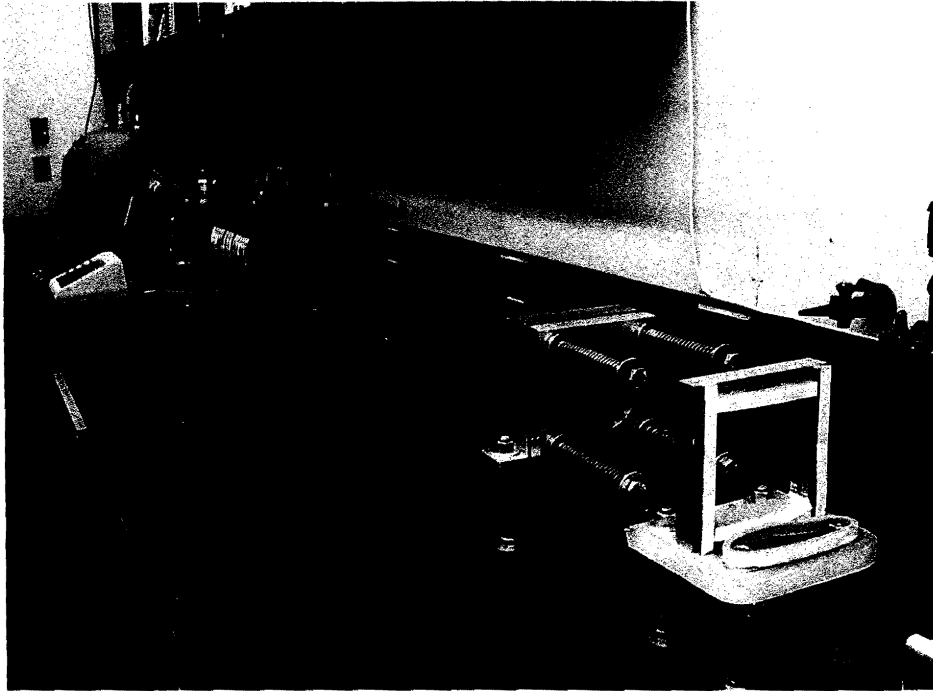


Figure 1.4- 1 Revision-3 Cannon

Note the steel and aluminum construction, a departure from the plastic material used in Revisions 1 and 2.

The Revision-3 design incorporated all the design knowledge from the first two revisions with extensive structural improvements based on commercial hydraulic cylinders. Because Revision 3 was to be the final design, the layout had to incorporate adjustability with sufficient strength and rigidity. Fine vertical adjustability was necessary to align the impact of the ball with the centerline of the bat to within ± 0.125 inches. Strength and rigidity were necessary to ensure that the alignment of the cannon

would not change during actuation, thereby altering the path of the ball. Revision 3 also boasted a precision-machined sabot, a spring-damped braking system, and a controlled, pulse width trigger.

The structural design began with finding a precision barrel material. The chosen material was honed-steel tubing from Pacific Machinery and Tool Steel [4], which had a 0.25-inch wall thickness and a tolerance of ± 0.02 inches on the inner diameter. The ends of the barrel slid into machined, aluminum end-caps, *see* figure 1.4-2, and fastened together with four tie-rods that ran the length of the barrel. The end-caps, shown in figure 1.4-3, provided planar surfaces to attach sealing plates and mounting hardware to secure the cannon to the bench top.

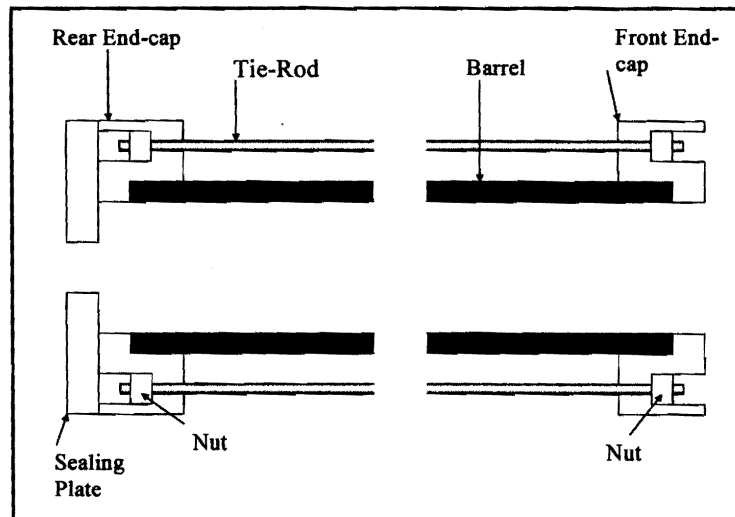


Figure 1.4- 2 Schematic of Cannon Assembly

The barrel is sandwiched between the two end-caps and fastened together with the tie-rods. The barrel sits in a counter bore machined into the aluminum end-cap. The tie-rods are secured with nuts that sit in counter bores at opposite ends of the cannon.



Figure 1.4- 3 Front and Back Views of Machined End -cap

Note the 5-inch to 4-inch shoulder on the bottom figure. This is where the barrel sits. In the top figure, the counter bores on four corners accommodate the nuts for the tie-rods, leaving the face of the end-cap flush to mount other components.

To seal the back of the barrel, a 6x6x1-inch aluminum plate was fastened to the end-cap with eight $\frac{1}{4}$ -20 bolts on each face; *see* figure 1.4-4. A 1.5-inch national pipe thread port was machined into the rear sealing plate to accommodate the solenoid valve.

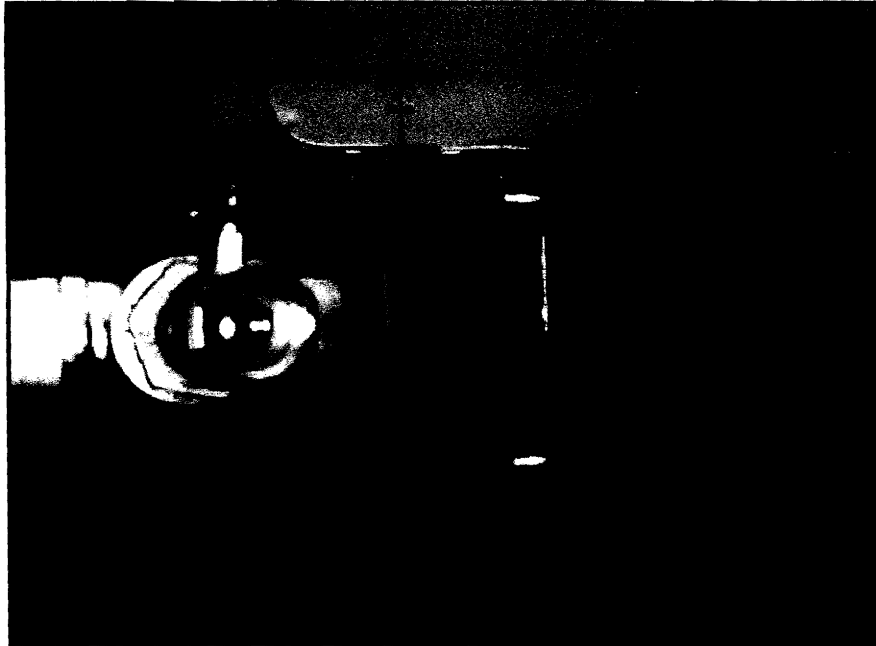


Figure 1.4- 4 Rear Sealing Plate

The photograph shows the rear sealing plate unbolted from the end-cap. The plate has a 1.5-inch national pipe thread port in the center and 8 $\frac{1}{4}$ -20 clearance holes around the edges for mating with the end-cap.

The cannon was mounted to the bench with a jackscrew design; *see* figure 1.4-5. The 0.5-inch, grade-5 all-thread had a national coarse threading of 13 threads per inch. This translated to an advancing rate of 0.0769 inches per revolution. This resolution was important in adjusting the elevation of the cannon since the bench top was not perfectly

level. Further, the jackscrews provided precise height adjustment for aligning the cannon with the center of the bat.

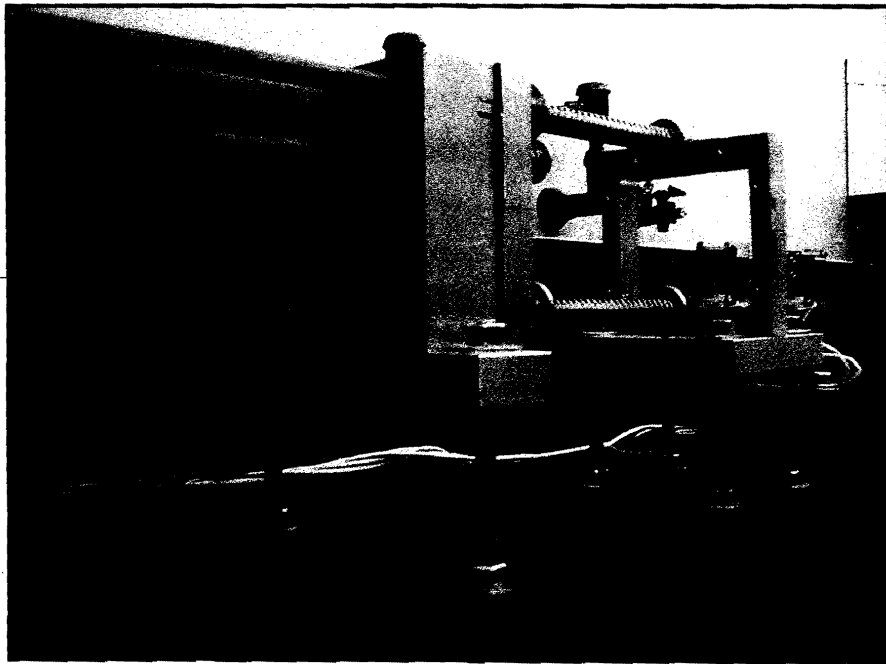


Figure 1.4- 5 Jackscrew Mounting

The block beneath the end flanges out to accommodate the all-thread. Besides fixing the cannon to the bench top, the jackscrew provides fine elevation adjustments.

1.4.1 Sabot Braking System

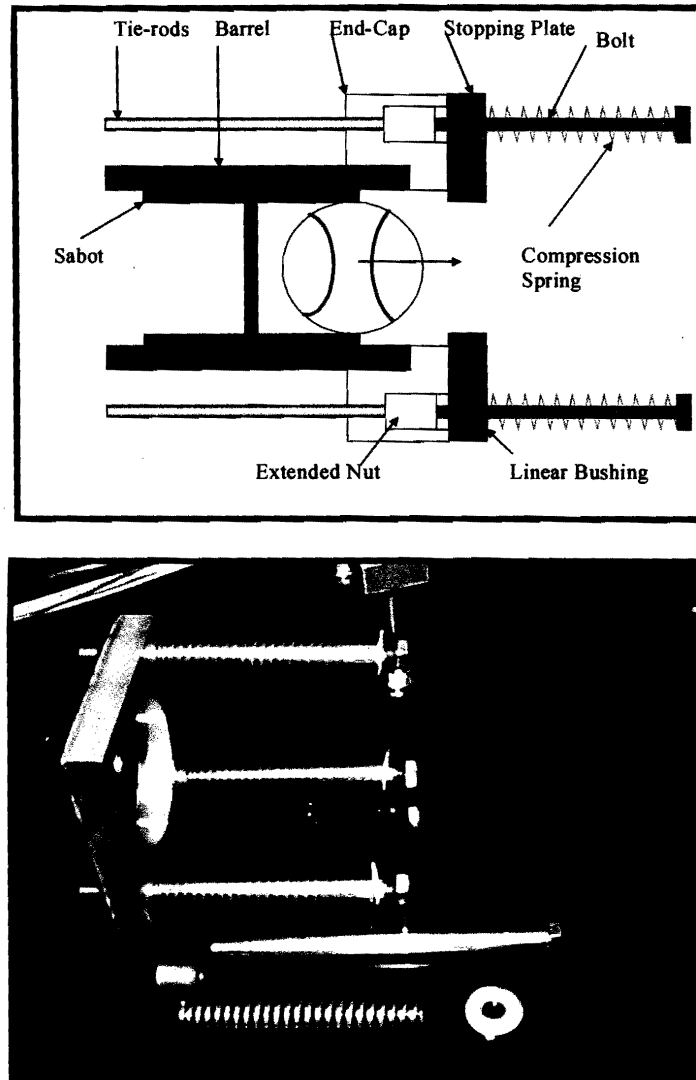


Figure 1.4- 6 Sabot Braking System

The schematic illustrates the second revision for a recoiling device. 6-inch long $\frac{1}{4}$ -20 bolts were used as the shafts and compressions springs were added to provide cushioning. This design improved the life of the sabot somewhat, but the bolts deformed from the impact.

The braking system required replacing the standard nuts at the end of the tie-rods with 1.5-inch long extended nuts. This provided four 0.5-inch threaded mounting holes to accommodate 0.5-inch bolts used for the shafting. A new stopping plate was machined to accommodate 0.5-inch bronze linear bushings, allowing the stopping plate to slide smoothly over the bolts. The braking system is shown in figure 1.4-6.

Upon testing the system with a standard, inexpensive softball bat the braking device seemed to work effectively. By the time the ball rebounded from the bat surface, the sabot was safely inside the barrel and the stopping plate was, again, resting against the end-cap. Since the stopping plate was 1-inch thick aluminum, impact by the rebounding ball caused no problems. With a high performance bat, however, the ball rebounded from the bat with such a high velocity that it struck the stopping plate before it was able to return to its initial position against the end-cap. The impact caused the plate to cock, thereby deforming the bushings and damaging the sabot. To protect the components an adjustable shield was placed in front of the cannon; *see* figure 1.4-7.

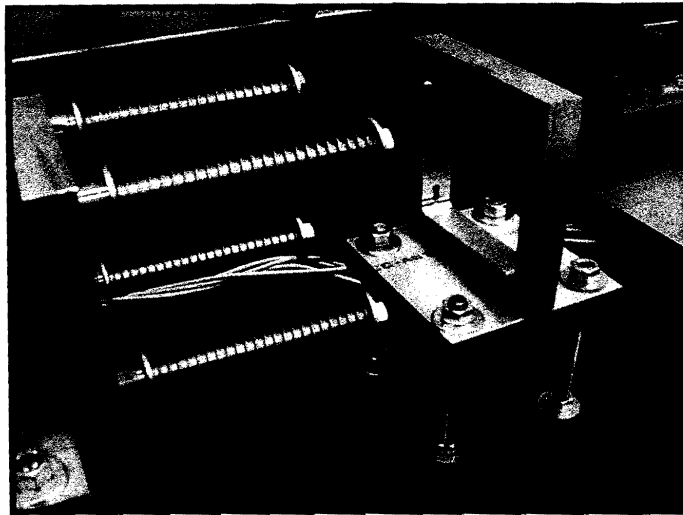


Figure 1.4- 7 Cannon Shield

The ball rebounding from a high-performance bat had tremendous velocity, striking the stopping plate before it has a chance to return to its rest position. The shield shown in the photograph deflects the ball from the cannon. The base has the same jackscrew design as the cannon for elevation adjustments.

In the final version of the braking system the bronze bushings were replaced with recirculating linear ball bearings. This reduced the friction of the sliding plate and improved the overall reliability. Further, the 7-inch bolts were replaced with 9-inch bolts, providing 6 inches of travel. These modifications eliminated the preload on the stopping plate, increased the deceleration distance, and softened the impact for the sabot.

1.4.2 Air-Control System

The compressed air was controlled with a solenoid valve from the irrigation industry. Although there are solenoid valves designed specifically for pneumatics, they required

pressure on both sides of the valve, and a 140-psi pilot pressure to actuate the valve. So far, the irrigation solenoid valve has worked flawlessly and costs one-fifth that of pneumatic valves. Since the solenoid valve was an electrical device there was the possibility of accidental triggering. As a safety precaution a 1.5-inch ball valve was fitted to the outlet port of the tank; *see* figure 1.4-8. The ball valve ensured that the outlet port was absolutely closed off whenever work was done at the muzzle.



Figure 1.4- 8 Air Storage Tank

The 30-gallon tank had a 1.5-inch front outlet port. A ball valve was fitted to the port for safety.

With the hose anchored by the tank and the solenoid valve anchored by the cannon, a flanged coupler was needed to make the final connection between these components; *see* figure 1.4-9.

The outlet port of the solenoid valve was connected to a T-fitting. The perpendicular branch of the T led to a 1-inch ball valve that connected the cannon to a vacuum system, which was used to draw the sabot back to the starting position. The in-line branch of the T led to the cannon barrel and threaded into the sealing plate. The center of the fluid circuit is shown in figure 1.4-9.



Figure 1.4- 9 Air Control System

The photograph shows the back of the cannon and the air-control system. In the center of the photo is the T-fitting. The perpendicular branch is connected to the hose of the shop-vac. The in-line branch is connected to the solenoid valve. Behind the gauge is the regulator, which is connected to the building air-supply line.

For Revision 1 and Revision 2 the solenoid valve was connected to a 12-volt battery regulated by a momentary on/off switch. With this set up, the duration the switch was depressed determined the duration the solenoid valve was open. Consequently, the

longer the longer the solenoid valve is open, the faster the sabot went. In an effort to add repeatability a fixed pulse trigger was used to actuate the solenoid valve. The circuit design came from the Engineer's Handbook on the Radio Shack website [10].

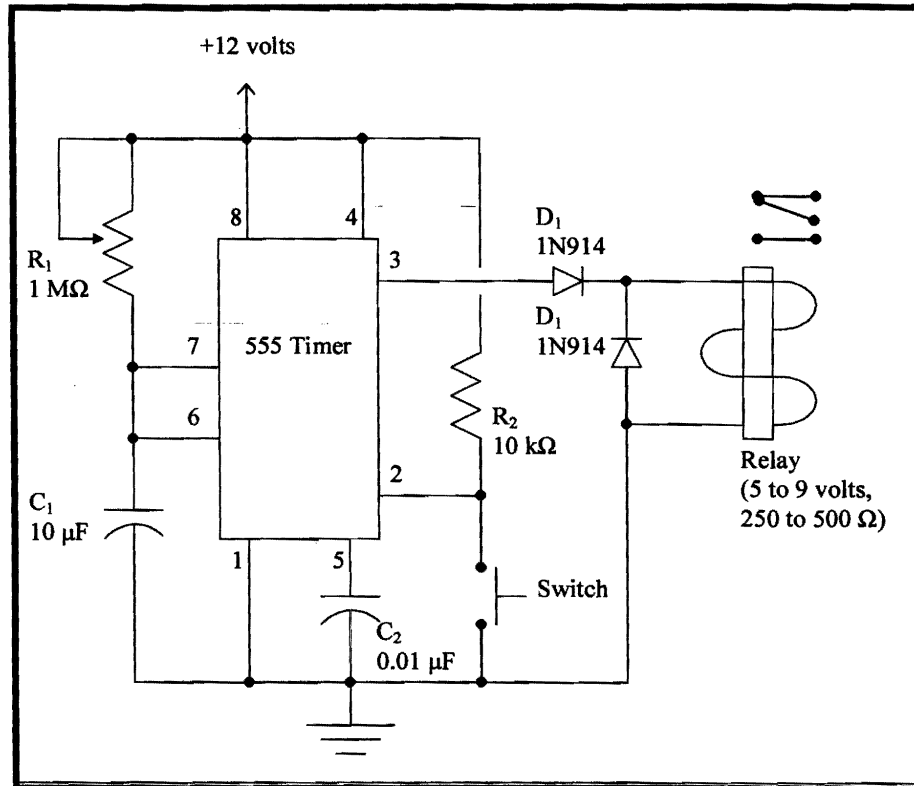


Figure 1.4- 10 Timer Plus Relay Circuit Used for Cannon Trigger

This diagram illustrates the relay circuit used to trigger the solenoid valve. By adjusting the potentiometer R1, the width of the pulse could be precisely controlled. The width of the pulse effectively controlled how long the solenoid valve was open.

The trigger consisted of a timer circuit to generate the pulse and a relay to regulate the current from a 12 VDC 500 mA adapter; see figure 1.4-10. The result was a trigger

that sent a square pulse of a fixed width to the solenoid valve when the circuit was triggered. The pulse width was adjusted by changing the resistance value of the circuit with a 100 k Ω potentiometer. After some tuning the pulse width was dialed to 200 ms.

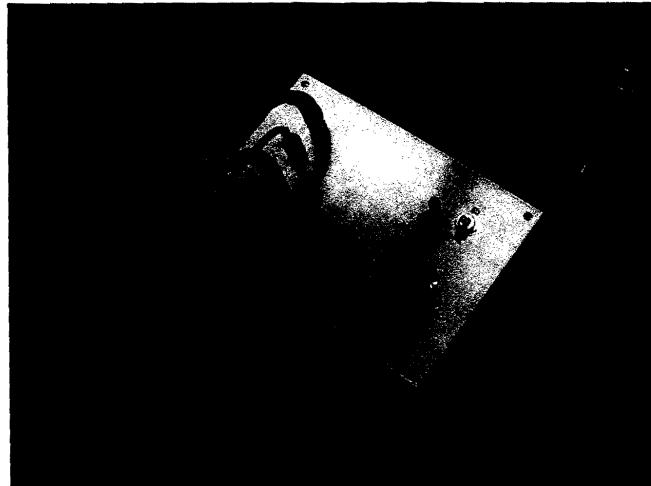


Figure 1.4- 11 Solenoid Valve Trigger Console

This console contains the relay trigger circuit. On the panel are the main power switch, the circuit trigger button, and a LED indicator.

The trigger circuit was housed in a console box to protect the wiring. The control panel consisted of a main power switch, a LED indicator, and a momentary switch to trigger the circuit. The main power was switched off until the moment before firing. The completed trigger is shown in figure 1.4-11.

With 1.5-inch fittings that stemmed from the outlet port of the tank to the sealing plate of the barrel, Revision 3. generated 88 ft/s at roughly 37 psi. This result demonstrated that the flow rate rather than the pressure of the system limited the sabot

speed. Besides the performance potential, the lower pressure requirement made the cannon safer for the operator and reduced the load on seals and other hardware.

1.4.3 Sabot

The first machined sabot was made from schedule 80 PVC piping with a nominal diameter of 4 inches and an actual outside diameter of 4.5 inches. Through trial and error, the pipe was turned down on a lathe to a diameter that slid smoothly in the barrel. To seal one end of the sabot, a PVC disk was turned down on a lathe and attached to the lip of the sabot with standard PVC cement. A bolt was threaded through the disk, providing a shank to mount the disk in the chuck of the lathe. This bolt was left in the disk after machining to seal the hole.

When this sabot was fired the bolt tore itself out, fracturing the disk.⁴ The difference in density between the steel bolt and the PVC disk probably led to the failure. Aside from the sealing disk fracture, the PVC sabot, which weighed about 1 pound, shook the entire structure when it impacted the shoulder. It was concluded that PVC was too dense for this application. The next step in designing the sabot involved searching for a lighter material with good impact characteristics.

Among the listed, high-impact plastics found in materials handbooks [5], ABS had the best combination of properties including low density, high impact resistance, low cost, and availability. In fact ABS tubing is sold at Home Depot stores for just over \$1 a foot.

The inner diameter of the honed steel tubing was measured with a pair of calipers to be 4.477 inches and the outer diameter of the ABS pipe was measured to be 4.5 inches. This meant 0.0115 inches needed to be removed from the radius to match the diameters. However, due to the irregularity of the ABS, the sabot was machined to a final outer diameter of 4.45 inches. From experience the closer the fit between the sabot and the barrel the better the durability of the sabot. The fit determined the amount of air leakage, as well as play, or rattle; a close fit reduced the possibility of cocking of the sabot as it traveled down the barrel.

Another important design problem with the sabot was attaching the sealing plate to the hollow ABS tube; *see* figure 1.4-12. With 0.25-inch ABS sheet material, the desired diameter was cut oversized on the band saw. The ABS disk was placed on a PVC template that had the correct outer diameter. Heavy-duty, two-sided tape and the tailstock held the disk to the template while it was turned down to the desired diameter.

⁴ For the preliminary sabot tests, the spring-damped braking system was not used. The sabot impacted the shoulder created by the aluminum stopping plate fastened to the end-cap.

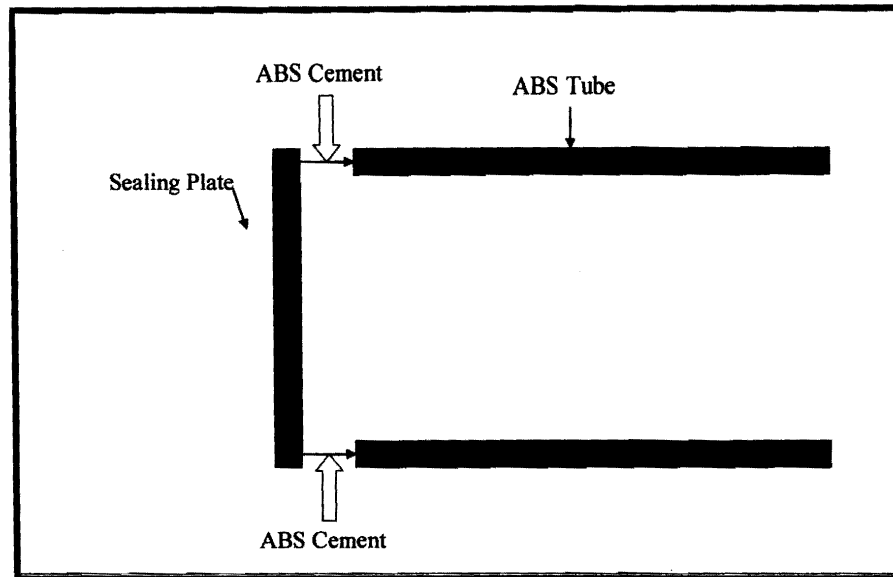


Figure 1.4- 12 Preliminary Sabot Assembly

This schematic illustrates how the sealing plate was attached to the ABS tubing. The cement was applied along the lip of the tube, the sealing plate was pressed on, and the assembly was clamped for the curing period of the cement. The failure of the technique was attributed to the small contact area.

Initially the disk was attached to the pipe with Weld-On ABS Cement from Multi-Craft Plastics. However, when the sabot impacted the shoulder, the disk fractured from the pipe body, tearing with it material from the pipe. The failure was probably attributable to the small contact area and the cement may possibly have had a brittling effect on the ABS. Despite this failure the ABS sabot, which weighed one-third that of the PVC, caused considerably less shock to the cannon.

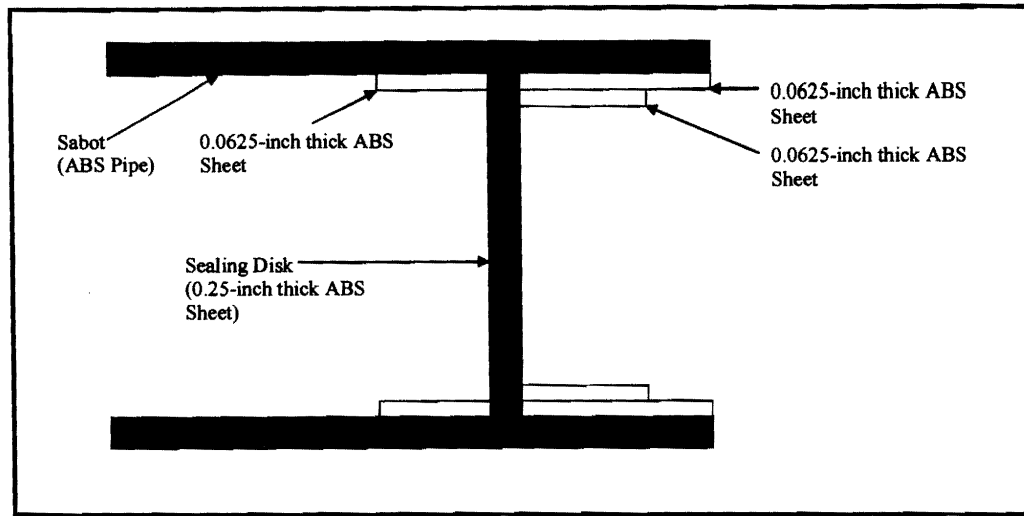


Figure 1.4- 13 Final Sabot Assembly

This schematic shows a cross section of the completed sabot. The sealing disk is placed a distance of half the ball diameter (1.875 inches) from the lip. The 0.0625-inch sheet material is used to change the inner diameter of the pipe. Layer 1 brings the pipe diameter within a few thousandths of an inch to the ball diameter. Layer 2 prevents the ball from sliding back into the sabot during acceleration. The retaining ring prevents the sealing disk from sliding backwards. The disk itself is elastically held by silicone adhesive, while the 0.0625-inch sheets are cemented on.

The solution involved machining the disk to fit inside the sabot body; *see* figure 1.4-13. Then, a 2-inch wide strip of 0.0625-inch ABS sheet material was cemented along the cylindrical surface at one end of the sabot. This layer created a shoulder inside the sabot, where the disk would rest. The disk itself was glued in with a silicone adhesive that provided a flexible bond. Finally, another strip of 0.0625-inch thick strip of ABS was cemented to the sabot behind the disk to prevent the disk from moving or rotating backwards. With this construction, the success of the sabot relied on the strength of

the front strip. Fortunately, the 2-inch wide rings made from the ABS strips provided adequate cementing surface area, thereby creating a solid bond.

Another attribute of this design was that the ABS sheets could be layered to match the ball diameter. For the softball, two layers were used. For other types of balls like baseballs or golf balls, additional layers of material can be added. By changing the diameter in steps, that is, by shortening the width of each subsequent layer, a single sabot could be used to test all balls smaller than a standard softball; *see* figure 1.4-14.



Figure 1.4- 14 Completed Sabot

The left photograph shows the sabot. The white region is the 0.0625-inch thick sheet that adjusts the inner diameter of the sabot. The right photograph shows the sabot inside the barrel with the brake assembly removed.

It was concluded that the final design satisfied all the requirements. The sabot was made from inexpensive, readily available ABS tubing; the structure demonstrated good reliability and durability; and finally, the design was versatile, able to accommodate different sized balls.

1.5 Bat Pivot Stage

The ASTM standards [1] were more specific for the pivoting stage; consequently, this component was significantly easier to develop than the ball launcher. Figure 1.5-1 shows a schematic of the stage and figure 1.5-2 shows a photograph of the stage.

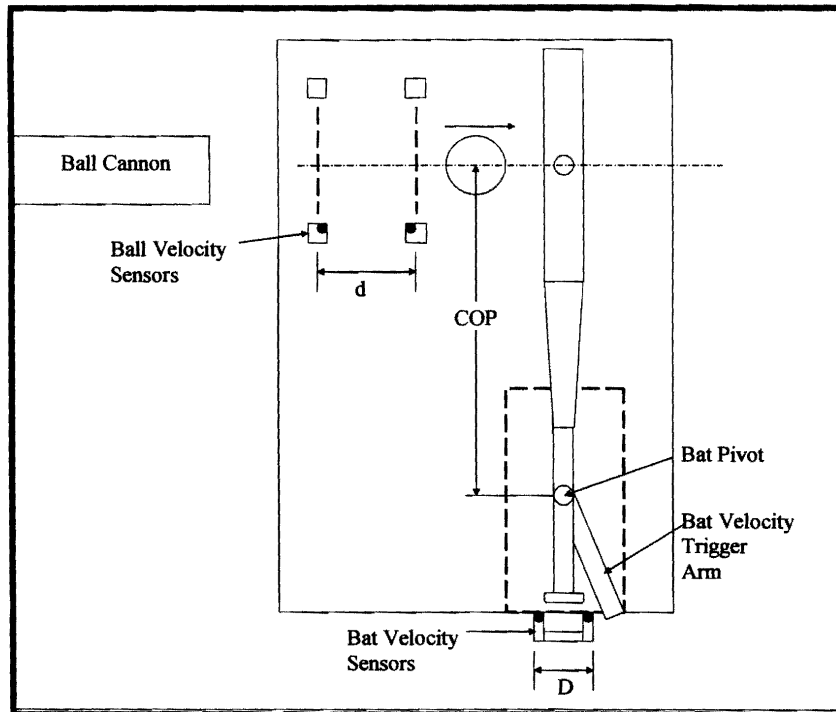


Figure 1.5- 1 Bat Pivot Stage Diagram

This schematic shows the layout of the bat pivot stage. All the velocity sensors are transmissive photocells. The ball exits the cannon and passes through the ball velocity sensors before impacting the bat. As the bat recoils the bat velocity trigger arm passes through the bat velocity sensors. The COP is the center of percussion of the bat. This dimension defines the distance between the bat pivot and the point of impact. D is the distance between bat photocells; d is the distance between the ball photocells.

The only major obstacle was coming up with a good way to clamp the bat into the pivot, while meeting the weight and inertia specifications of the standard. For the most part, the stage was designed with a strong emphasis on structural integrity. Consequently, this section essentially outlines the material and parts selection to create a robust design.

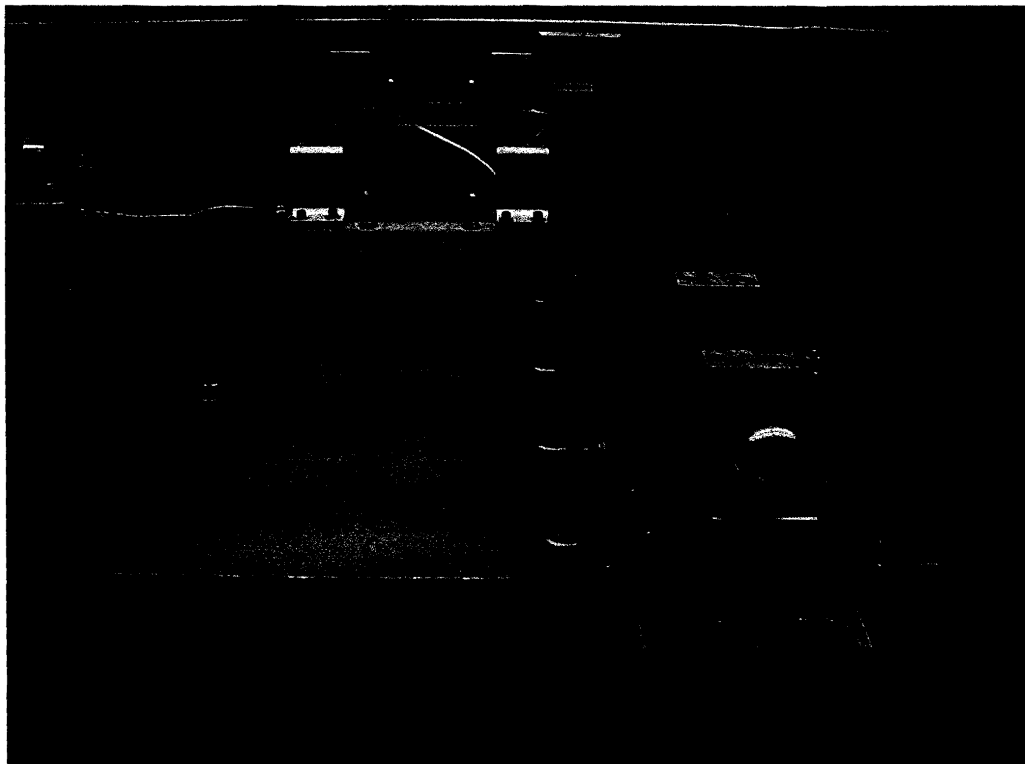


Figure 1.5- 2 Bat Pivot Stage

The 1x24x36-inch stage plate made mounting and aligning the components very simple.

For a stable foundation, the main stage was machined from a 1x24x36-inch aluminum plate that weighed about 90 pounds. This large work surface facilitated the

mounting of other components such as the pivot assembly and the ball and bat speed sensors. Plus, having all the components on the same plane made alignment easier. The only difficulty with the large plate was mounting it on the milling machine to drill the mounting holes for the other components.

The first item bolted to the stage was the pivot assembly. This structure consisted of a 3x6x12-inch aluminum block with a 1.25-inch hole bored through the center to position the shaft. The shaft was supported by a pair of 1-inch ball bearings and was secured to the block by custom-machined housings. Precision machining was critical in ensuring that the bearings had press fit into the housings, and the shaft had an interference fit with the inner raceway of the bearings; *see* figure 1.5-3.

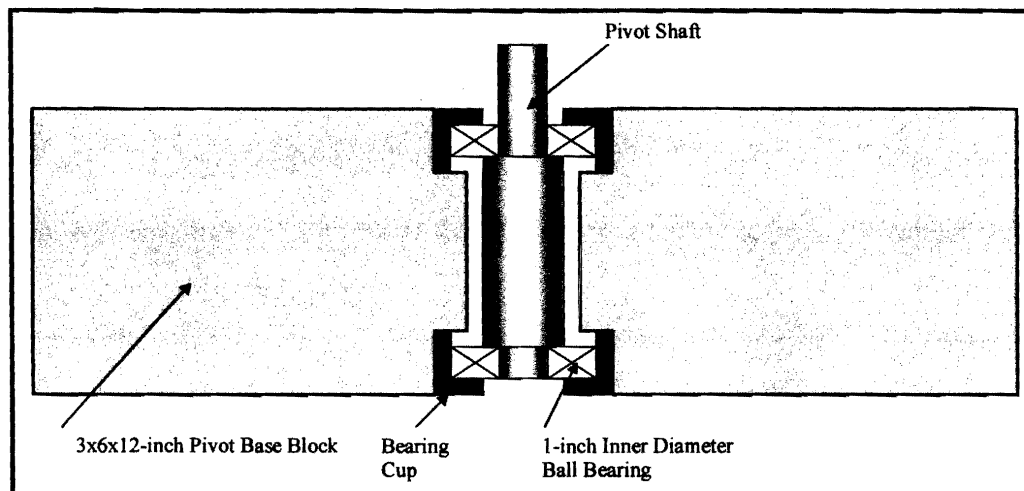


Figure 1.5- 3 Pivot Shaft Assembly Diagram

This schematic shows a cross section of the pivot assembly. The base was machined with a 1.25-inch bore through the center and counter bores on each side to accommodate the bearing cups and ball bearings. The shaft is sandwiched between the inner raceways of the bearings.

The shaft itself was custom machined with shoulders that rested on the inner raceways of the bearings. Consequently, the lower bearing also supported the shaft and pivot assembly in the vertical direction. This was where the precision machining was critical. A few degrees of play at the shaft translated to deflections of nearly 0.5 inch at the end of the 30- to 34-inch bat. At the end of the shaft was 1 inch of material to mount the trigger arm for the bat speed sensors and the base plate for the V-shaped clamping blocks.

The bat clamp consisted of four rectangular blocks with 90-degree grooves. The grooves were oriented in the vertical plane. The upper blocks forced the bat deeper into the grooves of the lower blocks. A pair of $\frac{1}{4}$ -20 screws that went through the upper blocks and threaded into the lower blocks generated the clamping force. The clamps are shown in figure 1.5-4.



Figure 1.5- 4 V-block Clamp Assembly

This photograph shows the revised bat clamping system for the pivoting stage. The four rectangular blocks effectively support the bat, and were easier to manufacture than cylindrical V-blocks.

The pivot assembly mounted in the 3x6x12-inch block was positioned and aligned by a pair of fences machined from 3x3-inch aluminum angle stock; *see* figure 1.5-5. Channels were milled into the vertical legs that line up with 0.4375-inch threaded holes on the pivot assembly block. This provided lateral positioning to align the center of percussion of the bat with the axis of the cannon. When the system was aligned, the bolts were tightened into the block and the assembly was rigidly fixed.



Figure 1.5- 5 Pivot Base Alignment Fence

The fence, which aligns and supports the pivot assembly, was machined from 0.375-inch thick aluminum angle stock.

An attribute of this design was the ability to stand the pivot base vertically, allowing the bat to rotate in the vertical plane. This feature facilitated the measurement of the period of oscillation of the bat-pivot assembly to get the natural frequency, which was used to calculate the moment of inertia of the bat and the bat-holding fixture together. By attaching a rotary potentiometer to the center of the pivot, the angular position of the bat could be recorded as a function of time. This method was more accurate and less time consuming than counting oscillations while keeping track of time on a stopwatch, the process used in the ASTM standard [1]. The standing pivot base and potentiometer are shown in figure 1.5-6.

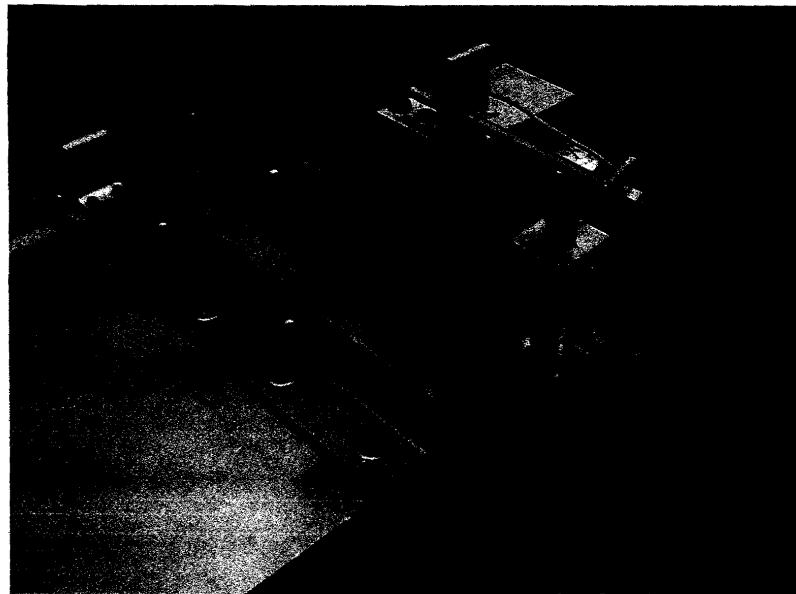


Figure 1.5- 6 Pivot Base Set Up for Oscillation in Vertical Plane

In this orientation the bat was able to swing in the vertical plane. The telescoping arm held the potentiometer, which provided angular position data. This set up facilitated the measurement of the natural frequency of oscillation of the bat, which was used to calculate the moment of inertia of the bat.

1.6 Instrumentation

The velocities of the ball and the bat were calculated with elapsed time data from pairs of photocells. The ball velocities were measured with Omron E3S-AT86 General Purpose Photoelectric Sensors, which have response times of 0.0005 seconds; *see* figure 1.6-1. Since a ball traveling at 88 ft/s covers its own diameter in about 0.003 seconds, a sensor with a response time shorter than 0.003 seconds was needed to ensure that the event was not missed. Figure 1.6-2 illustrates how the velocity measurements were made with the photocells. The sensors register an interruption in their signal when an object crosses their beam paths. The time between the interruptions denoted the time it took the ball to travel the distance between the sensors.

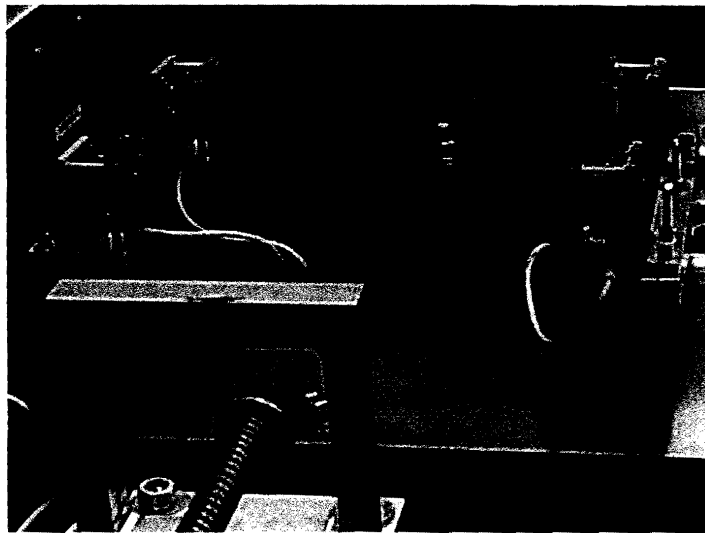


Figure 1.6- 1 Ball Velocity Sensors

Two sensor-emitter pairs comprise the photocells for velocity measurements.

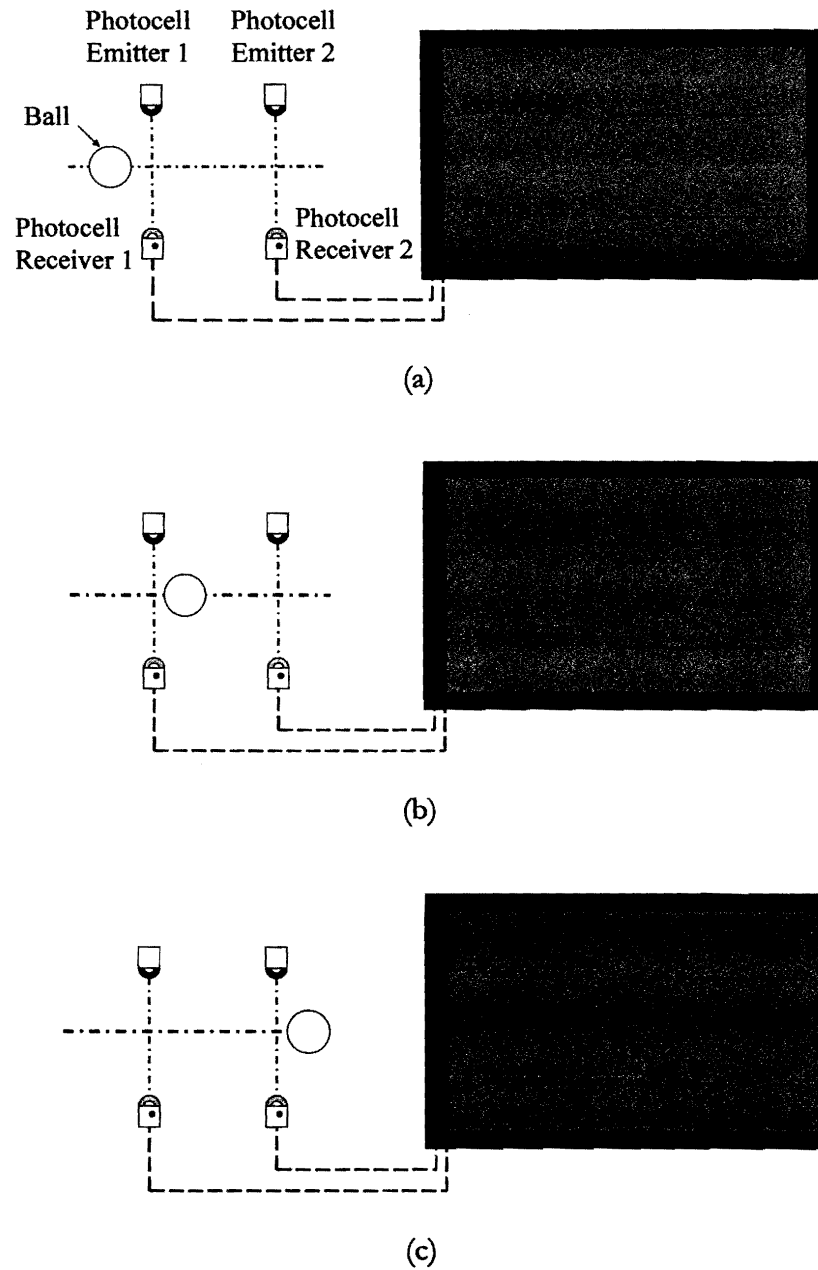


Figure 1.6- 2 Schematic of Ball Velocity Measurement

Figure (a) illustrates the lay out of the photocell emitters and receivers. The window on the right shows the signals of the photocells on an oscilloscope. Figure (b) shows the signals after the ball passes the first photocell. Figure (c) shows the signals after the ball passes the second photocell.

To measure the velocity of the recoiling bat a different type of arrangement was used; *see* figure 1.6-3. As noted in section 1.5, a 6-inch arm cantilevered from the shaft was used to trigger the sensors. Since the arm was only 0.125-inches thick, Omron EE-SX673A slotted photomicroswitches were ideal for this application. These photocells had a response time of 0.001 seconds. Assuming that the bat-pivot assembly behaves as a rigid body, the arm and the bat should rotate at the same angular velocity. As the trigger arm interrupts each photocell the oscilloscope signal peaks in a fashion similar to what is shown in figure 1.6-2 for the ball velocity measurement.



Figure 1.6- 3 Bat Velocity Sensors

The sensors are slotted photomicroswitches. When the trigger arm enters the slot, the signal is interrupted. The result is a pair of interruption pulses with the time between the pulses equal to the time required for the bat to move the distance between the sensors.

A potentiometer was installed to measure the angular position of the bat as it recoils, *see* figure 1.6-4. By numerically differentiating the angular position data that varied with time, it was possible generate a signal showing velocity of the bat as function of time. This provided useful insight about the response of the bat. Furthermore, the potentiometer facilitated the vertical swing test, described in the ASTM standard [1], used for determining the moment of inertia of the bat. This process is described in chapter 2.



Figure 1.6- 4 Angular Position Measurement

In-line with the pivot axis is the rotary potentiometer. This instrument provides angular position data as a function of time.

Initially, the outputs of the four photocells were sampled with a pair of 2-channel oscilloscopes; *see* figure 1.6-5. After each test shot the times corresponding to the interruption pulses were manually recorded. This technique was inefficient and did not allow for the data to be stored. With the addition of the potentiometer signal, another oscilloscope would be necessary. Rather than purchasing another oscilloscope, and to facilitate the data acquisition, the five signals were sampled with Labview software that interfaced with an analog-to-digital converter board. With this set up, data from the 5 signals for each shot were sampled and written to a spreadsheet file. The data file was then loaded into Matlab where a program extracted the pertinent times and performed all the necessary calculations.



Figure 1.6- 5 Original Data Acquisition Instruments

On the left are the two 2-channel oscilloscopes. On the far right is the electronics console housing the circuit that powers the sensors and connects the output signals to the oscilloscopes. In the center is the power supply.

1.7 Bat Stopping Device

The final detail about the pivoting stage involved stopping the bat after the impact occurred and the measurements had been made. Since the cannon was so close to the pivoting bat, it was imperative that the bat stopping device be simple and not prone to failure. The most reliable stopper would be a passive cushioning device such as a punching bag. The first design consisted of a heavy-duty recreational storage pouch filled with sand. This worked relatively well; the sand effectively absorbed all the energy of the impact. The bat came to a full stop at the bag and did not recoil or bounce off the bag.

Since the sand was relatively dense, there was a concern of damaging the bat with repeated hits. As a simple remedy, dense foam sheeting was wrapped around the sand bag. This material turned out to be too elastic. The bat bounced off the foam with significant velocity and swung back toward the photocells. The challenge involved finding a substance with the same dissipative characteristics, but with a lower density to provide more cushioning for the bat. As rudimentary as it may sound, birdseeds provided the ideal consistency. The final design consisted of a cylindrical bag with sand at the base and filled with birdseeds to stop and cushion the bat; *see* figure 1.5-7.

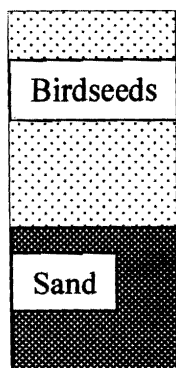


Figure 1.7- 1 Bat Stopping Device

The bat stopping device was a polymer bag with a layer of sand on bottom and a layer of birdseeds on top. The sand keeps the bag from moving while the birdseeds provide a softer cushion for the bat.

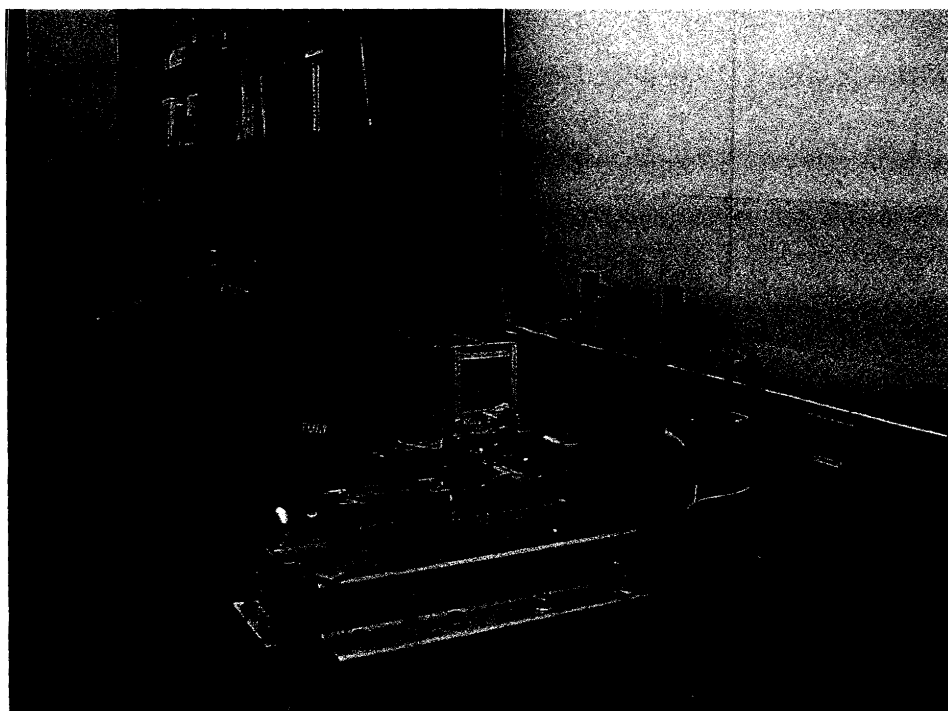


Figure 1.7- 2 Complete System

The cylindrical object is the stopping device, a polymer bag with the base filled with sand, and the rest of the space filled with birdseeds.

1.8 Results and Conclusion

Once all the instrumentation was installed the tank pressure was calibrated to launch the ball at 88 ft/s. This was done by setting the pressure, firing the ball, measuring the resulting velocity, and then adjusting the pressure up or down to dial in the desired velocity. Table 1.8-1 shows eight consecutive shots during the calibration period.

Shot No.	1	2	3	4	5	6	7	8	Average	Standard Deviation
Velocity [ft/s]	85.57	89.03	86.69	85.57	89.03	90.25	89.03	86.69	87.73	1.81

Table 1.8- 1 Measured Ball Velocities

This table shows the velocities of eight consecutive shots after calibration at 37.5 psi.

No explicit tests were carried out to quantify the aiming accuracy of the cannon. The ASTM standard [1] outlines a measurement process in which an aluminum plate is mounted in place of the bat. The desired center of impact is marked on the aluminum plate and a sheet of carbon paper is taped to the plate. The aiming accuracy was then quantified by measuring the eccentricity of the carbon smudge, presumed to be a circle, from the center of impact mark. This procedure seemed inaccurate and painstaking. Consequently, quantifying the aiming accuracy was postponed.

However, the fact that the ball had a tendency to fly back into the cannon after rebounding off the bat demonstrated that the ball was striking the center of the bat. If the ball impacted the bat above the centerline, the ball would have a tendency to

rebound with an upward trajectory. If the ball struck the bat below its centerline the ball would tend to rebound with a downward trajectory.

Through the three revisions an apparatus was developed that provided the precision and accuracy necessary to make BPF measurements. The velocity variation was within 2 ft/s and, although the aiming accuracy was not quantified, the tendency for the ball to reenter the barrel indicated that the ball was striking the center of the bat. Furthermore, with 1.5-inch fittings stemming from the tank port the desired velocity was reached with a tank pressure of 37 psi.⁵

The design and fabrication of the cannon and the pivoting stage incorporated precision materials with custom machining to create a robust product with high adjustability and repeatability. The careful planning and layout enabled this device to directly measure the rebound velocity of the ball—a quantity that current devices are unable to measure

⁵ The funding partner was impressed by this specification because some testing agencies have launchers with operating pressures as high as 240 psi.

Chapter 2: Analysis and Experimental Methods

The ASTM standard [1] provided specific guidelines to calculate the bat performance factor (BPF), a process involving precise measurements of the properties of the bat and ball as well as the pertinent velocity data. This chapter presents the development of the BPF equation from the conservation of angular momentum equation. This development is presented with an alternative method of calculating the BPF, the direct method. The direct method calculates the coefficient of restitution (COR) of the bat-ball system with a direct measurement of the rebound velocity of the ball. This chapter also includes a sensitivity analysis of the variables in the BPF equation, illustrating that the ASTM method magnifies measurement errors of geometric and inertial properties of the bat as well as errors of the measured velocities.

2.1 Bat Characteristics and Experiment Set Up

This section describes the methods used to measure the bat's weight (W_{bat}), balance point (BP) or center of gravity (CG), moment of inertia (I), and center of percussion (COP).

2.1.1 Measurement of the Weight and Balance Point

The weight of the bat was determined using a triple beam balance, which has an accuracy of 0.1 grams or 0.0036 ounces. The location of the balance point or center of gravity is determined using the set up shown in figure 2.1-1.

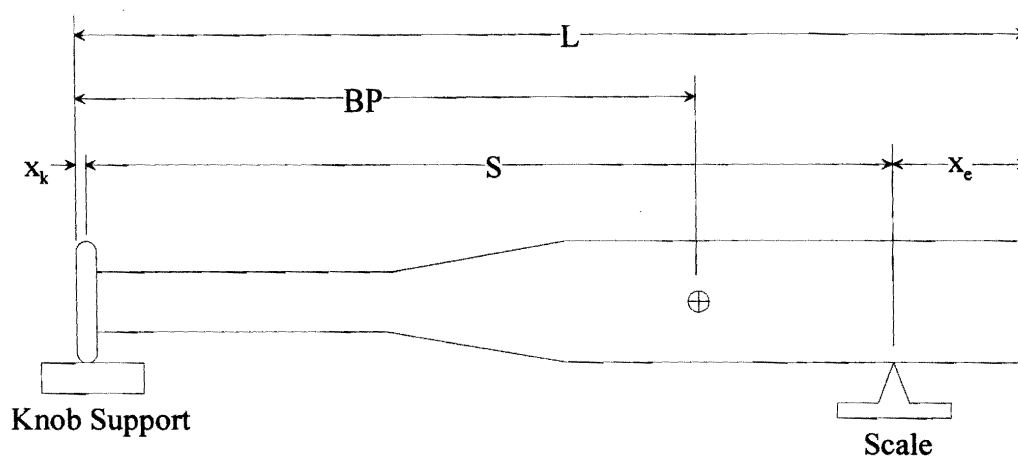


Figure 2.1- 1 Set Up for Determining Balance Point

This diagram shows the various dimensions needed to determine the balance point or center of gravity.

L	bat length
x_k	distance from the end of the bat to the contact point
S	distance between the two points of support
x_e	distance from the scale to the end of the bat
BP	distance from knob base to the balance point
W_{bat}	total bat weight
W_{scale}	weight at scale support

The location of the balance point (BP) is determined by summing moments about point o as shown in figure 2.1-2.

$$\sum M_o = -W_{bat} (BP - x_k) + W_{scale} S = 0$$

$$BP - x_k = \frac{W_{scale} S}{W_{bat}} \quad (2.1.1)$$

Substituting $S = (L - x_e - x_k)$ and solving for BP yields

$$BP = \frac{W_{scale} (L - x_e - x_k)}{W_{bat}} + x_k. \quad (2.1.2)$$

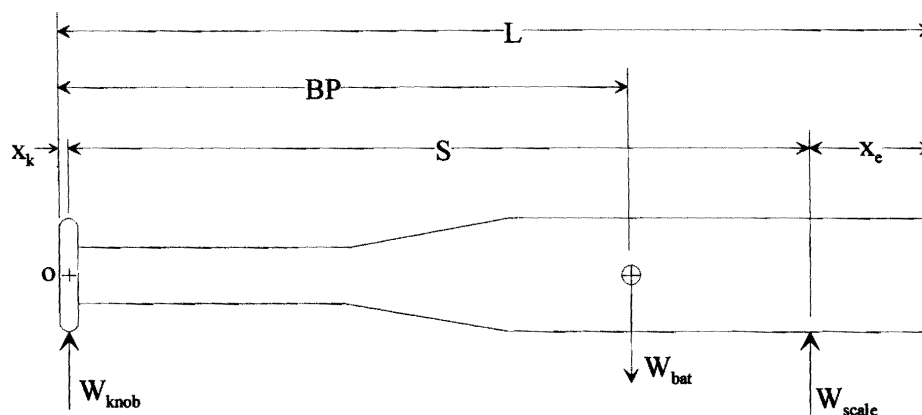


Figure 2.1- 2 Bat Free Body Diagram

The diagram shows reaction moments used to determine the balance point. W_{knob} is the reaction force at the knob. Since this force does not generate a moment, it does not appear in equation (2.1.2).

For accuracy, the BP was measured at three different values of x_e . The results for the Easton bat are shown in Table 2.1-1.

x_e (in)	W_{scale} (oz)	W_{bat} (oz)	BP (inch)
1.00	16.00	26.60	19.39
6.00	19.00	26.60	19.38
11.00	23.40	26.60	19.39
Average BP	19.39		

Table 2.1- 1 Balance Point Calculation for Easton Bat

This table shows the calculated balance point for different scale locations.

It was not possible to use the triple beam balance to determine the weight values for the BP calculation. The scale yielded weights that were approximately 3 percent lower than those determined on the beam balance. Since the weights appear as a ratio in the BP calculation this difference did not cause an inaccuracy in the BP calculation.

2.1.2 Measurement of the Moment of Inertia

The moment of inertia was measured experimentally by measuring the period of oscillation of the bat. The bat was clamped in a shaft collar and the collar was supported at two points by ball-bearing pivots; *see* figure 2.1-3 (inset). The bat was given a maximum 15-degree deflection, and the time for 10 or more cycles was measured with a stopwatch. This period was measured three times, and the average period was calculated.

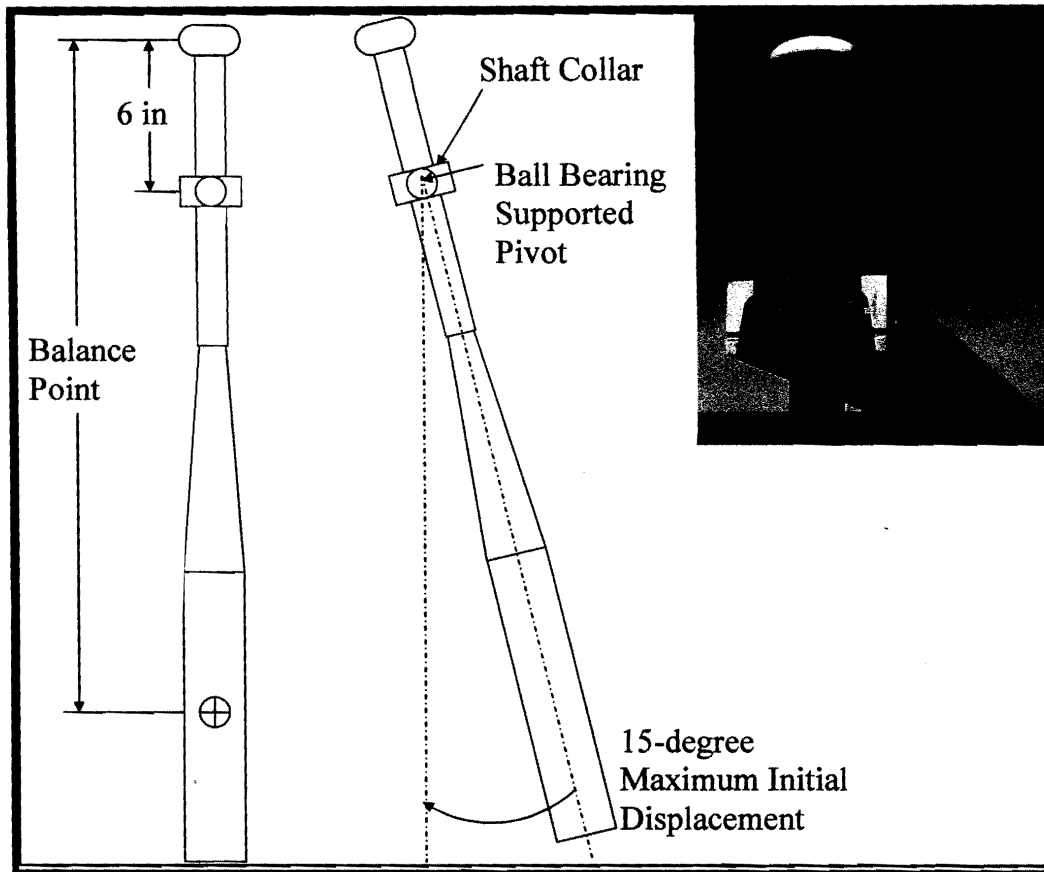


Figure 2.1- 3 Moment of Inertia of Bat Only

The schematic shows the set up for measuring the moment of inertia of the bat. It is assumed that the moment of inertia of the shaft collar is negligible compared to that of the bat. The inset picture shows the shaft-collar pivot.

A simple pendulum that oscillates with a small angle (less than 15 degrees) has a natural frequency and period shown in the equation (2.1.3).

$$\omega_n = \sqrt{\frac{(BP - 6)M_{bat}g}{I}}$$

$$Period = \frac{2\pi}{\omega_n} = \frac{2\pi}{\sqrt{\frac{(BP - 6)M_{bat}g}{I}}} \quad (2.1.3)$$

ω_n	natural frequency (rad/sec)
Period	oscillation period (sec)
BP	location of the balance point (BP) (inch)
M_{bat}	bat mass (oz)
g	gravitational constant (386 in/sec²)
I	bat moment of inertia about the pivot point (oz-in²)

Solving for the Moment of Inertia (I):

$$I = Period^2 \left(\frac{g}{4\pi^2} \right) M_{bat} (BP - 6). \quad (2.1.4)$$

Substituting for the acceleration of gravity and π yields

$$I = Period^2 (9.779) M_{bat} (BP - 6). \quad (2.1.5)$$

The moment of inertia calculated in equation (2.1.5) represents the moment of inertia of the bat alone because the moment of inertia of the shaft collar was negligible compared to the moment of inertia of the bat. However, the moment of inertia of the V-block clamp assembly of the bat pivoting stage, used in the BPF test, is more substantial. Consequently, the pendulum test shown in figure 2.1-3 had to be run again with the clamp assembly. The moment of inertia calculated in this test would be the moment of inertia of the bat plus the moment of inertia of the pivoting stage.

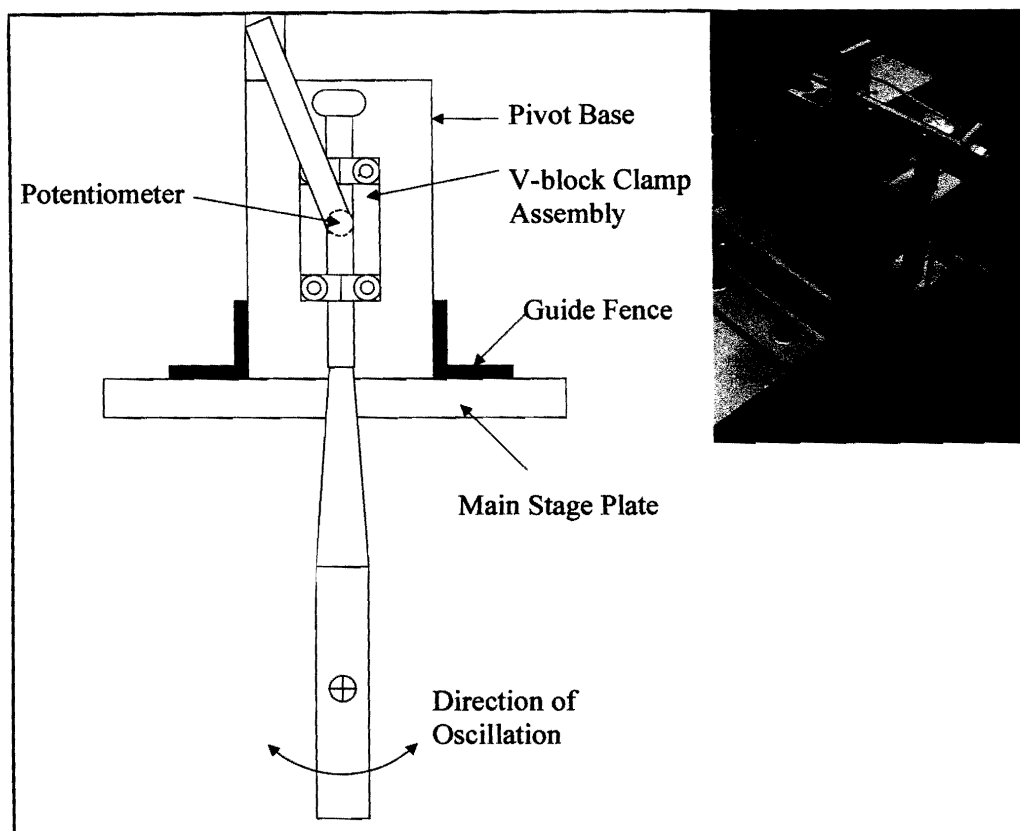


Figure 2.1- 4 Set Up for Measuring Moment of Inertia of Bat and Clamp

The schematic shows the pivot assembly rotated 90 degrees, allowing the bat to rotate in the vertical plane. The potentiometer is used to measure the period of oscillation. The inset photograph shows the actual swing test set-up.

The pendulum test with the V-block clamp assembly involved rotating the entire pivot assembly 90 degrees such that the bat is free to rotate in the vertical plane. Measurement of the period of oscillation was facilitated by the installation of the potentiometer. A schematic of the measurement layout is shown in figure 2.1-3.

Table 2.1-2 summarizes the moment of inertia information from the pendulum test for the Easton bat.

Bat Type	Mbat (oz)	BP (in)	Period (sec)	I (oz - in ²)	Period (sec)	I (oz - in ²)
			(Bat Only)	(Bat Only)	(Bat plus Pivot)	(Bat plus Pivot)
Easton	26.81	19.39	1.46	7498.52	1.49	7740.28

Table 2.1- 2 Summary of Moment of Inertia Measurements

This table shows the moment of inertia of bat with and without the clamp assembly.

2.1.3 Center of Percussion (COP)

The center of percussion (COP) of a body rotating about a fixed axis, has the unique property that the sum of all moments about the COP is always 0 ($\sum M_{COP} = 0$). This means that if the ball strikes a bat, mounted to rotate about a fixed axis, at the COP the reaction forces at the pivot are 0.

The equation that locates the COP is

$$COP = \frac{I}{M_{bat}(BP - 6)}. \quad (2.1.6)$$

The variables are shown in figure 2.1-5.

BP	location of the balance point (in)
M_{bat}	bat mass (oz)
I	bat moment of inertia about the pivot point (oz-in ²)

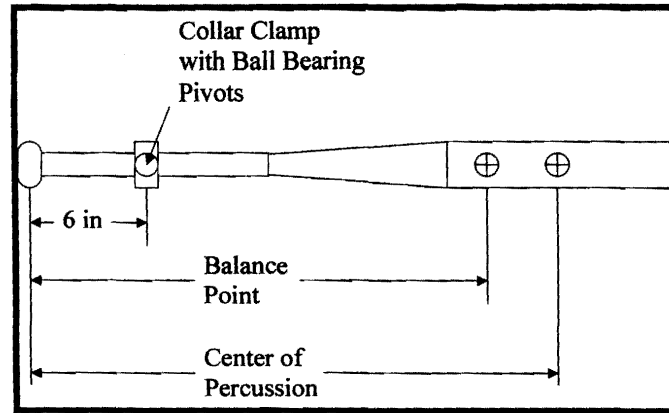


Figure 2.1- 5 Location of the Center of Percussion

This schematic shows the pivot point, balance point, and the center of percussion.

Substituting for the value of I yields

$$COP = \frac{Period^2 \left(\frac{g}{4\pi^2} \right) M_{bat} (BP - 6)}{M_{bat} (BP - 6)}$$

$$COP = Period^2 \left(\frac{g}{4\pi^2} \right)$$

$$COP = Period^2 (9.779) \quad (2.1.7)$$

Table 2.1-3 summarizes the COP measurement for the Easton bat.

Bat Type	Period (sec)	COP (in)
Easton	1.46	20.78

Table 2.1- 3 Center of Percussion of Easton Bat

2.1.4 Equipment Layout

This section outlines the experimental set up. Several diagrams in the ASTM standard [1] illustrate the layout of the sensors and the pivoting stage. Figure 2.1-6 shows the placement of the cannon, pivoting stage, and the ball and bat velocity sensors. As the ball exits the cannon, it passes through the ball photocells where its approach velocity is measured. After impact, the bat recoils and the trigger arm passes through the slotted photocells, thereby measuring the velocity of the bat. At the same time, the ball rebounds off the bat and passes back through the ball photocells, providing a measurement of the ball rebound velocity.

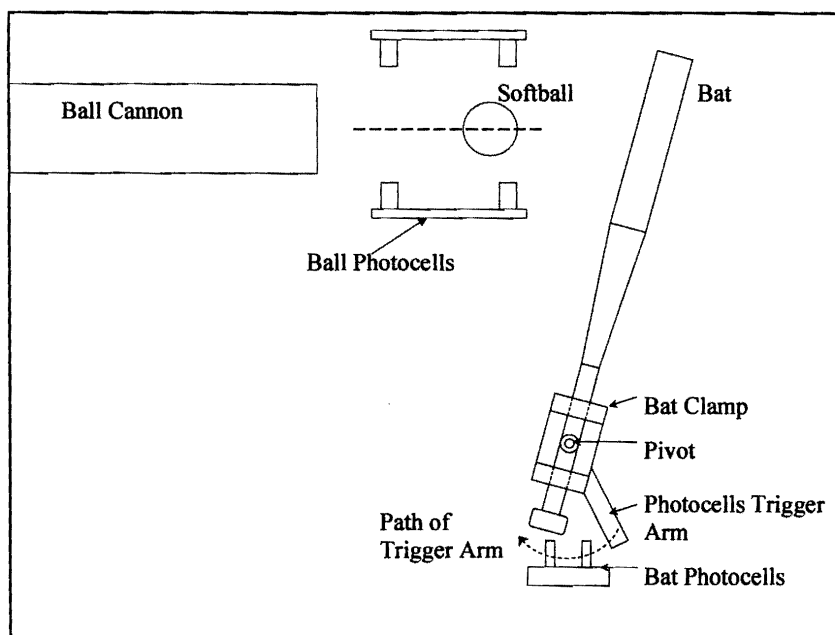


Figure 2.1- 6 Experimental Set Up for Ball and Bat Velocity Measurements

Measurement of the bat recoil velocity is made with the trigger arm close to the pivot center.

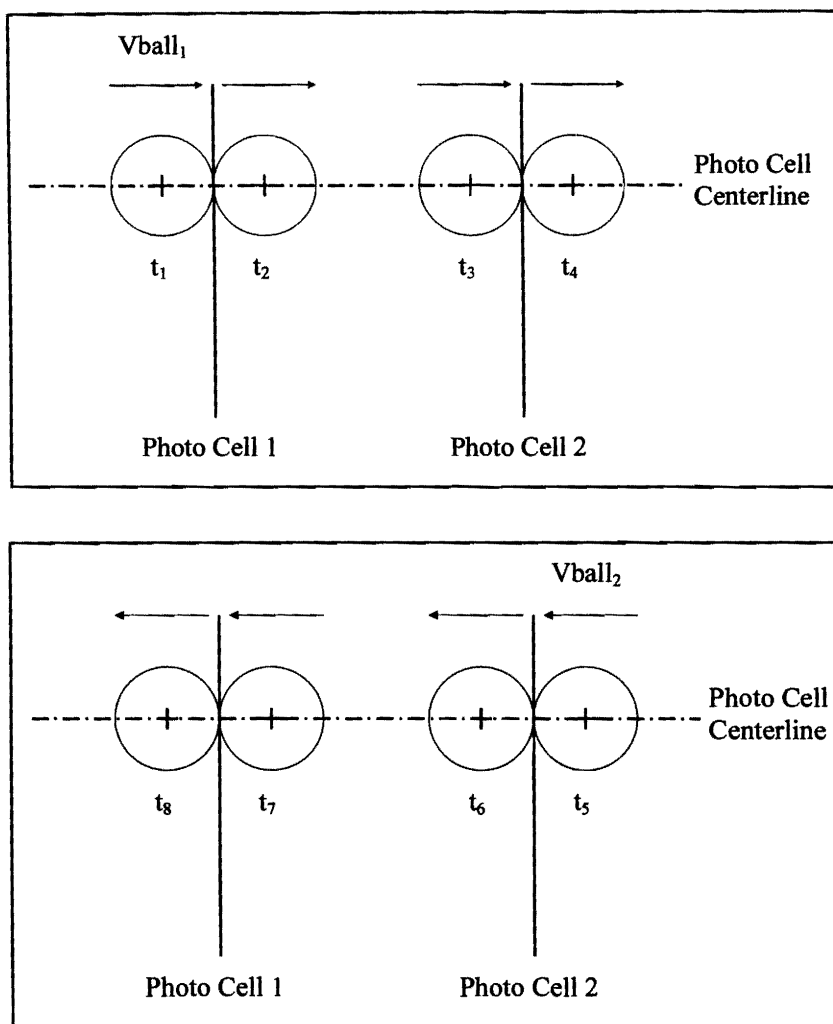


Figure 2.1- 7 Ball Traveling Through the Photocells

The top figure shows the ball traveling towards the bat and the bottom figure shows the ball rebounding off the bat. At each photocell, the lower of the subscripted time corresponds to the instant the leading edge of the ball interrupts the signal and the larger subscript indicates the instant the ball passes and the signal is reestablished.

Figures 2.1-7 and 2.1-8 show the path of the ball through the ball photocells. The times correspond to the instances when the ball enters and exits the line of sight of the photocells. The corresponding signals are shown in figure 2.1-9, which is a typical data

set for a single test shot. Figure 2.1-10 shows a typical signal of the trigger arm passing through the slotted, bat photocells. The square pulses on both figures correspond to the duration the ball, or the trigger arm, is interrupting the photocell transmission from the emitter to the receiver.

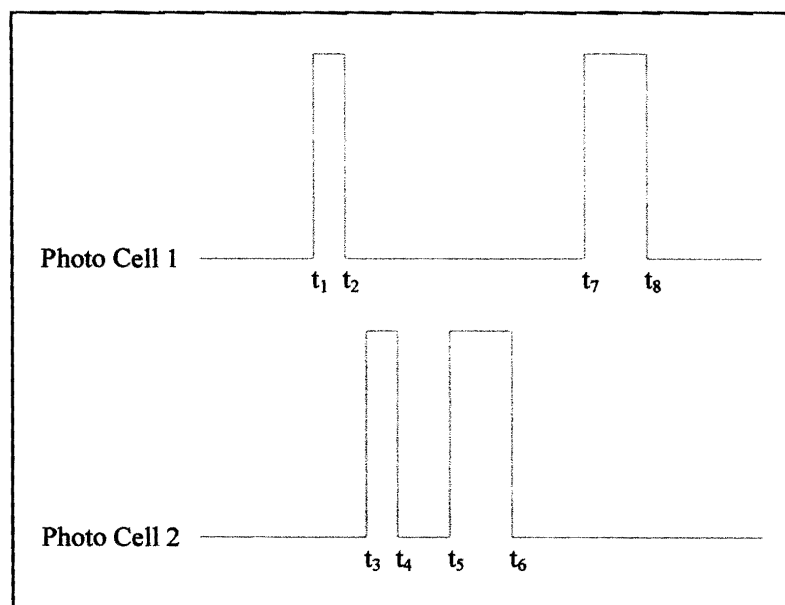


Figure 2.1- 8 Typical Ball Photocell Signal

This schematic shows the photocell signals as the ball passes through the sensors on its approach and rebound.

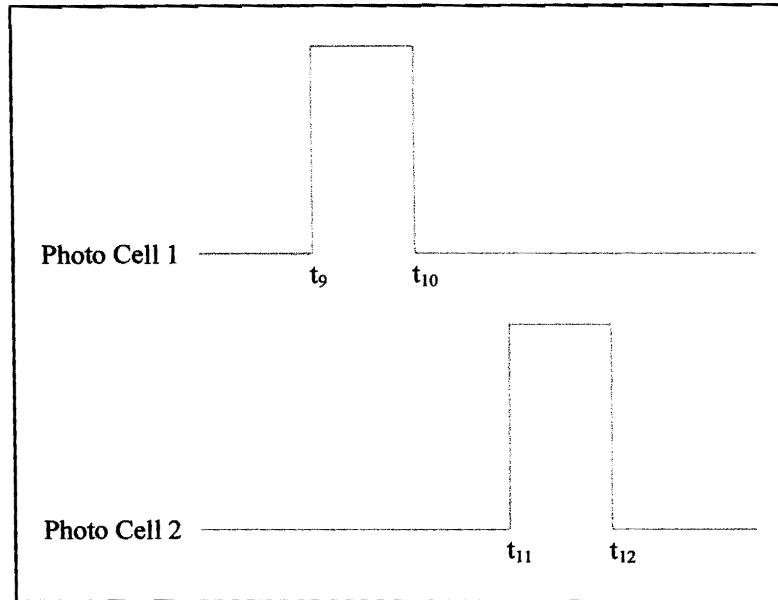


Figure 2.1- 9 Typical Bat Photocell Signal

This schematic shows the photocell signal as the trigger arm passes through the bat photocells.

2.2 Measurement of the Coefficient of Restitution of the Ball

The basic test involved firing the ball at 88 ft/sec at a rigid block and measuring the ball inbound speed (V_{ball_1}) and the ball rebound speed (V_{ball_2}). The ball coefficient of restitution is

$$COR_{ball} = \frac{V_{ball_2}}{V_{ball_1}}. \quad (2.2.1)$$

V_{ball_1} was measured as the ball passed through the photocells toward the rigid block. V_{ball_2} was measured as the ball passed back through the photocells after rebounding

from the rigid block. The rigid block was 16x11.5x11-inch solid oak plywood laminate with a 1-inch thick aluminum faceplate. The block was bolted to the table with eight 0.5-inch bolts and a 0.5-inch thick backer plate. For the balls tested, the average COR_{ball} was found to be 0.43, somewhat less than the manufacturer's value of 0.47.

2.3 ASTM Method for Calculating the Bat Performance Factor

Two methods will be presented to calculate the bat performance factor (BPF). The first, presented in this section, is the method required by the ASTM standard [1]. The second method is presented in section 2.4. The variables defined below will be used in the development that follows.

COP	center of percussion
R	distance between the bat pivot point and the COP (point of impact)
COR	coefficient of restitution
$COR_{Bat-Ball}$	coefficient of restitution of the bat-ball system
COR_{Ball}	coefficient of restitution of the ball only
BPF	$COR_{Bat-Ball} / COR_{Ball}$
ω_{bat_1}	angular velocity of the bat about the bat pivot point before impact
ω_{bat_2}	angular velocity of the bat about the bat pivot point after impact
ω_{ball_1}	angular velocity of the ball about the bat pivot point before impact
ω_{ball_2}	angular velocity of the ball about the bat pivot point after impact
V_{bat_1}	velocity of the bat at the COP before impact
V_{bat_2}	velocity of the bat at the COP after impact
V_{ball_1}	velocity of the ball before impact
V_{ball_2}	velocity of the ball after impact
I	moment of inertia of the bat about the bat pivot point
M_{ball}	mass of the ball

Figure 2.3-1 shows the bat and ball velocities before and after impact.

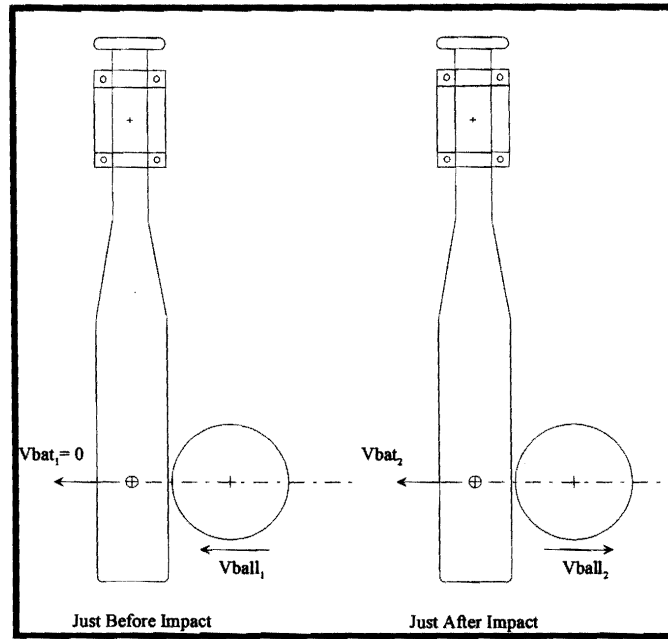


Figure 2.3- 1 Velocities before and after Impact

The coefficient of restitution (COR) is defined as:

$$COR = \frac{\text{Velocity of Separation (after impact)}}{\text{Velocity of Approach (before impact)}} \quad (2.3.1)$$

For the bat-ball system it is convenient to first express the COR in terms of angular velocity about the bat pivot point.

$$COR_{\text{Bat-Ball}} = \frac{\text{Angular Velocity of Separation (after impact)}}{\text{Angular Velocity of Approach (before impact)}} \quad (2.3.2)$$

$$COR_{Bat-Ball} = \frac{\omega_{bat_2} - \omega_{ball_2}}{\omega_{ball_1} - \omega_{bat_1}} \quad (2.3.3)$$

$$V = R\omega \rightarrow \omega = \frac{V}{R} \quad (2.3.4)$$

$$COR_{Bat-Ball} = \frac{\frac{V_{bat_2}}{R} - \frac{V_{ball_2}}{R}}{\frac{V_{ball_1}}{R} - \frac{V_{bat_1}}{R}} = \frac{V_{bat_2} - V_{ball_2}}{V_{ball_1} - V_{bat_1}} \quad (2.3.5)$$

For the bat-ball system $V_{bat_1} = 0$.

$$COR_{Bat-Ball} = \frac{V_{bat_2} - V_{ball_2}}{V_{ball_1}} \quad (2.3.6)$$

The ASTM method for calculating the BPF measures V_{ball_1} and V_{bat_2} and determines V_{ball_2} from the conservation of momentum as shown below. Conservation of momentum is first written in terms of angular momentum.

Angular momentum (about the bat pivot) before impact = Angular momentum (about the bat pivot) after impact

$$I(\omega_{bat_1}) + (M_{ball})(V_{ball_1})R = I(\omega_{bat_2}) + (M_{ball})(V_{ball_2})R \quad (2.3.7)$$

Solving for V_{ball_2} and noting that $\omega_{bat_1} = 0$ and $\omega_{bat_2} = \frac{V_{bat_2}}{R}$ yields

$$V_{ball_2} = \frac{(M_{ball})(V_{ball_1})R - I\left(\frac{V_{bat_2}}{R}\right)}{(M_{ball})R} \quad (2.3.8)$$

$$V_{ball_2} = V_{ball_1} - I \frac{V_{bat_2}}{M_{ball} R^2} \quad (2.3.9)$$

The expression for V_{ball_2} can now be substituted into the $COR_{Bat-Ball}$ equation.

$$COR_{Bat-Ball} = \frac{V_{bat_2} - V_{ball_2}}{V_{ball_1}} = \frac{V_{bat_2} - V_{ball_1} + I \frac{V_{bat_2}}{M_{ball} R^2}}{V_{ball_1}}$$

$$COR_{Bat-Ball} = \frac{V_{bat_2}}{V_{ball_1}} - 1 + I \frac{V_{bat_2}}{V_{ball_1} M_{ball} R^2}$$

$$COR_{Bat-Ball} = \left(1 + \frac{I}{M_{ball} R^2}\right) \frac{V_{bat_2}}{V_{ball_1}} - 1 \quad (2.3.10)$$

V_{ball_1} and V_{bat_2} can be expressed in terms of the following variables.

- D distance between the bat speed sensors (in)
- d distance between the ball speed sensors (in)
- r radius to the bat speed sensors (in)
- R distance between the bat pivot point and the COP (Point of Impact)
- T time for the bat to travel through the bat speed sensors
- t time for the ball to travel through the ball speed sensors

$$V_{ball_1} = \frac{d}{t} \quad V_{bat_2} = \frac{RD}{rT} \quad (2.3.11)$$

$$\frac{V_{bat_2}}{V_{ball_1}} = \frac{DRt}{drT} \quad (2.3.12)$$

Substituting the expression above into the $COR_{Bat-Ball}$ equation yields

$$COR_{Bat-Ball} = \left(1 + \frac{I}{M_{ball} R^2} \right) \left(\frac{DRt}{drT} \right) - 1. \quad (2.3.13)$$

The BPF is defined as follows.

$$BPF = \frac{COR_{Bat-Ball}}{COR_{Ball}} = \frac{\left(1 + \frac{I}{M_{ball} R^2} \right) \left(\frac{DRt}{drT} \right) - 1}{COR_{Ball}}. \quad (2.3.14)$$

Equation (2.3.14) represents the ASTM method for calculating the BPF. As will be discussed below, the BPF calculated using the ASTM method is very sensitive to measurement or parameter errors.

2.4 Direct Method for Calculating the BPF

As noted in section 2.3, the ASTM method for calculating the BPF measures V_{ball_1} and V_{bat_2} and determines V_{ball_2} from the conservation of momentum equation. With the ability of the test apparatus, with the Revision-3 cannon, to measure the rebound velocity, a more direct method of calculating the BPF was possible. The bat-ball COR

can be calculated as a simple ratio of approach and rebound velocities. Recall the relation for $COR_{bat-Ball}$:

$$COR_{Bat-Ball} = \frac{V_{bat_2} - V_{ball_2}}{V_{ball_1}} \quad (2.4.1).$$

When the ball rebounds from the bat after impact there may be a small upward or downward velocity in addition to the primary horizontal velocity. This is due to the fact that the ball may strike the bat slightly above or slightly below the bat centerline. The cannon design allowed for very precise control of the ball position. In fact it was not uncommon for the ball to rebound off the bat and reenter the cannon barrel; *see* section 1.4.3.

Nevertheless the following analysis takes into account that the ball may slightly rise or fall after it rebounds off the bat. Figure 2.4-1 shows the ball passing through the two photocells after rebounding from the bat. The list below identifies the variables in the figure.

t_5	time at which the ball enters photocell 2
t_6	time at which the ball leaves photocell 2
t_7	time at which the ball enters photocell 1
t_8	time at which the ball leaves photocell 1
Db_1	diameter of the ball as it passes through photocell 2
Db_2	diameter of the ball as it passes through photocell 1
D_{ball}	ball diameter
d	distance between photocells
$L_1, L_2, L_3,$ and L_4	distances identified in the figure

The goal is to find an expression for the ball rebound velocity (V_{ball_2}) as well as diameters Db_1 and Db_2 . Start by defining the following time differences.

$$\Delta t_0 = t_6 - t_5$$

$$\Delta t_1 = t_7 - t_6$$

$$\Delta t_2 = t_8 - t_7$$

The following lengths can be expressed in terms of the ball diameters:

$$L_1 = \frac{D_{ball}}{2} - \frac{Db_1}{2}$$

$$L_2 = \frac{D_{ball}}{2} - \frac{Db_2}{2}$$

$$L_4 = D_{ball} - \left(\frac{D_{ball}}{2} - \frac{Db_2}{2} \right) = \frac{D_{ball}}{2} + \frac{Db_2}{2}$$

$$L_3 = d - L_4 + L_1 = d - \left(\frac{D_{ball}}{2} + \frac{Db_2}{2} \right) + \left(\frac{D_{ball}}{2} - \frac{Db_1}{2} \right) = d - \frac{Db_2}{2} - \frac{Db_1}{2}$$

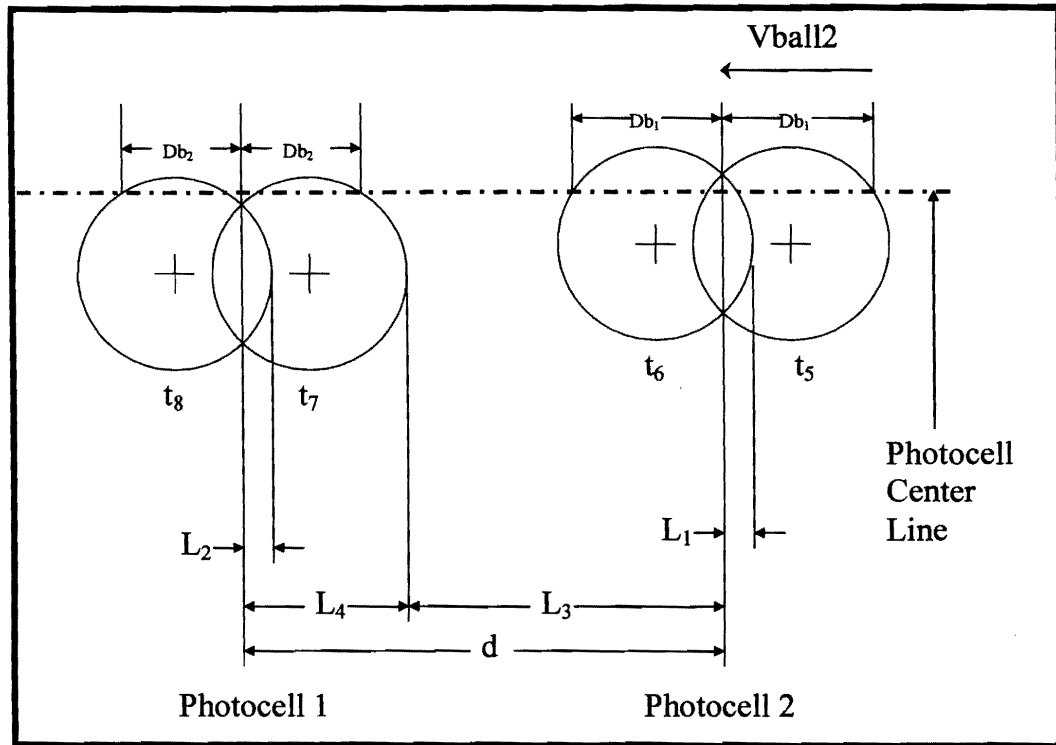


Figure 2.4- 1 Ball Translating through Photocells after Rebounding from Bat

The schematic shows the motion of the ball back through the photocells after rebounding from the bat. Although the path of the ball can be controlled so precisely that it reenters the barrel of the cannon, the figure shows a method to account for any vertical displacement.

The ball rebound velocity (V_{ball_2}) can be written in three ways:

$$V_{ball_2} = \frac{Db_1}{\Delta t_0} \quad \text{ball velocity across photocell 2}$$

$$V_{ball_2} = \frac{L_3}{\Delta t_1} \quad \text{ball velocity between photocells}$$

$$V_{ball_2} = \frac{Db_2}{\Delta t_2} \quad \text{ball velocity across photocell 1}$$

These three equations can be solved for V_{ball_2} , Db_1 and Db_2 .

$$V_{ball_2} = \frac{d}{\Delta t_1 + \frac{\Delta t_0}{2} + \frac{\Delta t_2}{2}}$$

$$Db_1 = \frac{d(\Delta t_0)}{\Delta t_1 + \frac{\Delta t_0}{2} + \frac{\Delta t_2}{2}}$$

$$Db_2 = \frac{d(\Delta t_2)}{\Delta t_1 + \frac{\Delta t_0}{2} + \frac{\Delta t_2}{2}}$$

The equations above can be used to find the ball rebound velocity (V_{ball_2}) as well as Db_1 and Db_2 . The values of Db_1 and Db_2 are useful in determining whether the ball is rising or falling after rebounding from the bat. This information can be used to align the cannon with the center of the bat.

Note that in the analysis above it was assumed that the ball diameters, as the ball passes the photocells (Db_1 and Db_2), were equal on the right and left intersection points of the photocell. When the ball is rising or falling these diameters will be slightly different. The diameters Db_1 and Db_2 are the average value of the diameters as the ball passes photocells 1 and 2 respectively. Since the angle that the ball can come off the bat and still pass through both photocells is quite small (less than 7 degrees) this assumption did not cause any significant error in the velocity measurement.

The equation for the BPF using the direct method is as follows:

$$Vball_1 = \frac{d}{t} \quad Vball_2 = -\frac{d}{\Delta t_1 + \frac{\Delta t_0}{2} + \frac{\Delta t_2}{2}} \quad Vbat_2 = \frac{RD}{rT}$$

$$BPF_{vel} = \frac{\left(\frac{RD}{rT} + \frac{d}{\left(\Delta t_1 + \frac{\Delta t_0}{2} + \frac{\Delta t_2}{2} \right)} \right) t}{d COR_{ball}}$$

$$BPF_{vel} = \frac{t RD}{d (COR_{ball}) r T} + \frac{t}{COR_{ball} \left(\Delta t_1 + \frac{\Delta t_0}{2} + \frac{\Delta t_2}{2} \right)}$$

$$BPF_{vel} = \frac{t(2RD\Delta t_1 + RD\Delta t_0 + D\Delta t_2 + 2drT)}{d COR_{ball} r T (2\Delta t_1 + \Delta t_0 + \Delta t_2)} \quad (2.4.2)$$

The advantage of the direct method of calculating the BPF is that there are far fewer variables in the calculation and each of those variables is directly measured. As will be seen in section 2.5 the variation in the BPF calculated using the direct method (BPF_{vel}) is much smaller than the BPF calculated using the ASTM method.

2.5 Sensitivity of the BPF to Measurement and Parameter Errors

The magnification factor, defined below, is a normalized representation of how much the BPF function changes for a given small change in one of the variables.

$$\text{magnification factor} = \frac{\text{percentage change in the BPF function}}{\text{percentage change in the variable}}$$

$$\text{percent change in function} = \frac{\left(\frac{\partial f}{\partial x} \right)_0 \Delta x}{(f)_0} (100) \quad (2.5.1)$$

For example, assume the sensitivity analysis was based on the variable I , the moment of inertia, with a percent change of Δ . Equation (2.5.1) would be

$$\text{magnification factor} = \frac{\left(\frac{\left(\frac{\partial (BPF)}{\partial I} \right)_0 \Delta I_0}{(BPF)_0} \right)}{\Delta} (100). \quad (2.5.2)$$

Table 2.5-1 summarizes the magnification factors for the variables in the BPF equation. As can be seen in table 2.5-1 most of the magnification factors are above 2.0. This indicates that the BPF equation is very sensitive to changes in the variables. For example if the measured time t was 1 percent high and the moment of inertia was also 1

percent high, the BPF value would be approximately 6 percent high. This would increase the BPF from 1.20 to 1.27. This effect is amplified because so many variables in the BPF equation have a high magnification factor.

Variables	Units	Nominal Values	MF ASTM
I	oz-in ²	7740.28	2.12
Mball	oz	6.64	-2.12
R	in	20.77	-1.36
r	in	5.69	-2.87
D	in	3.00	2.87
d	in	7.91	-2.87
T	ms	26.80	-2.87
t	ms	7.80	2.87
CORball	none	0.43	-1

Table 2.5- 1 BPF Magnification Factors for the ASTM Method

Table 2.5-2 summarizes the magnification factor for the variables in the BPF_{vel} equation.

Variables	Units	Nominal Values	MF Direct
R	in	20.77	0.98
r	in	5.69	-0.98
D	in	3.00	0.98
d	in	7.91	-0.98
T	ms	26.80	-0.98
t	ms	7.80	1.00
CORball	none	0.43	-1.00
dt0	ms	36.40	-0.0046
dt1	ms	48.20	-0.012
dt2	ms	36.00	-0.0045

Table 2.5- 2 BPF Magnification Factors for the Direct Method

As seen in table 2.5-2 the magnification factor was less than or equal to 1.0 for all of the variables. In addition these variables are directly measured thus further minimizing any errors. This result was consistent with the measured BPF values that showed the BPF_{vel} having a much smaller variation (standard deviation = 0.0099) than the BPF results (standard deviation = 0.0427).

2.6 Results and Conclusion

Below is a table containing the data of a typical BPF test session. The bat used for the test was a standard inexpensive aluminum softball bat. Immediately following the table is a list of variables as well as figures describing the photocell time measurements used to calculate the ball and bat velocities.

time pt1 to time pt12	time points (milli-seconds) see figures 2.1-7 to 2.1-8 below for identification
time Ball	time for the ball to pass through the photocells ($t_3 - t_1$) (milli-seconds) (t)
time Bat	time for the bat extension arm to pass through the photocells ($t_{11} - t_9$) (milli-seconds) (I)
BPF	bat performance factor calculated using the ASTM method
BPF_{vel}	bat performance factor calculated using the direct method of measuring V_{ball_2}
V_{ball_2}	velocity of the ball after rebounding from the bat (V_{ball_2})
V_{bat_2}	velocity of the bat after impacting with the ball (V_{bat_2})
V_{ball_1}	velocity of the ball after leaving the cannon (V_{ball_1})

D (in)	r(in)	d(in)	I (oz-in ²)	Mball (oz)	
3.00	5.69	7.91	7740.28	6.64	
R	CORball	g (in/sec ²)			
20.78	0.43	386.64			
	Data Set 1	Data Set 2	Data Set 3	Data Set 4	Data Set 5
time pt1	0.00	0.00	0.00	0.00	0.00
time pt2	3.60	3.50	3.40	3.40	3.40
time pt3	7.80	7.60	7.80	7.60	7.80
time pt4	11.40	11.10	11.40	11.20	11.20
time pt5	24.40	21.60	26.20	23.80	24.20
time pt6	60.80	50.40	63.20	60.00	60.00
time pt7	109.00	99.00	111.00	104.00	104.00
time pt8	145.00	111.00	134.00	134.00	139.00
time pt9	0.00	0.00	0.00	0.00	0.00
time pt10	9.00	9.40	9.00	9.00	9.00
time pt11	26.80	26.80	26.80	26.60	26.80
time pt12	36.20	36.20	36.20	35.80	36.20
time Ball	7.80	7.60	7.80	7.60	7.80
time Bat	26.80	26.80	26.80	26.60	26.80
BPF	1.14	1.06	1.14	1.08	1.14
BPF_vel	1.15	1.17	1.17	1.15	1.17
Delta_BPF	0.01	0.11	0.03	0.07	0.02
Vball_2	7.81	9.55	8.47	8.55	8.30
Vbat_2	34.08	34.08	34.08	34.34	34.08
Vball_1	84.47	86.69	84.47	86.69	84.47
DB1	3.41	3.30	3.76	3.71	3.56
DB2	3.37	1.38	2.34	3.08	3.49
D_out	3.65	3.64	3.65	3.75	3.45
	%Change	Average	St. Deviation		
BPF	8.43	1.11	0.04		
BPF_vel	1.83	1.16	0.01		

Table 2.6- 1 BPF Test Data for Easton Bat

The experimental apparatus and methods were presented to measure the bat performance factor for softball bats. The main components of the experimental

apparatus were the ball cannon, the bat pivoting stage, and the photocell arrangement. The designed experimental apparatus met all of the ASTM requirements, providing accurate and repeatable measurements of the bat performance factor.

Two methods of calculating the BPF were presented. The ASTM method and the direct method, which used a direct measurement of the ball rebound velocity—the ASTM method derived the ball rebound velocity by applying conservation of angular momentum. It was found that the direct method was much less sensitive to measurement errors, and had a smaller measured variation, than the BPF calculated using the ASTM method.

Chapter 3: Elastic Impact Dynamic Analysis

3.1 Introduction

Recall that the bat performance factor (BPF) was the ratio of the bat-ball coefficient of restitution (COR) to the COR of the ball impacting a rigid surface. Calculation of the bat-ball COR required three quantities: the approach velocity of the ball, the rebound velocity of the ball, and the recoil velocity of the bat. The testing apparatus developed in this project allowed the BPF to be calculated by two different methods: the ASTM method and the direct method.

$$BPF_{ASTM} = \frac{\left(1 + \frac{I}{M_{ball} R^2}\right) \left(\frac{D R t}{d r T}\right) - 1}{COR_{ball}} \quad (3.1.1)$$

$$BPF_{Direct} = \frac{\left(\frac{R D}{r T} + \frac{d}{\left(\Delta t_1 + \frac{\Delta t_0}{2} + \frac{\Delta t_2}{2} \right)} \right) t}{d COR_{ball}} \quad (3.1.2)$$

The primary difference between the two methods was determination of the ball rebound velocity. In the ASTM method, equation (3.1.1), the ball rebound velocity was derived by applying conservation of angular momentum. Consequently, the bat-ball

COR was calculated with the ball approach velocity, the bat recoil velocity and their corresponding inertias. In the direct method, equation (3.1.2), the ball rebound velocity was measured directly and the bat-ball COR was calculated with the three independent velocities.

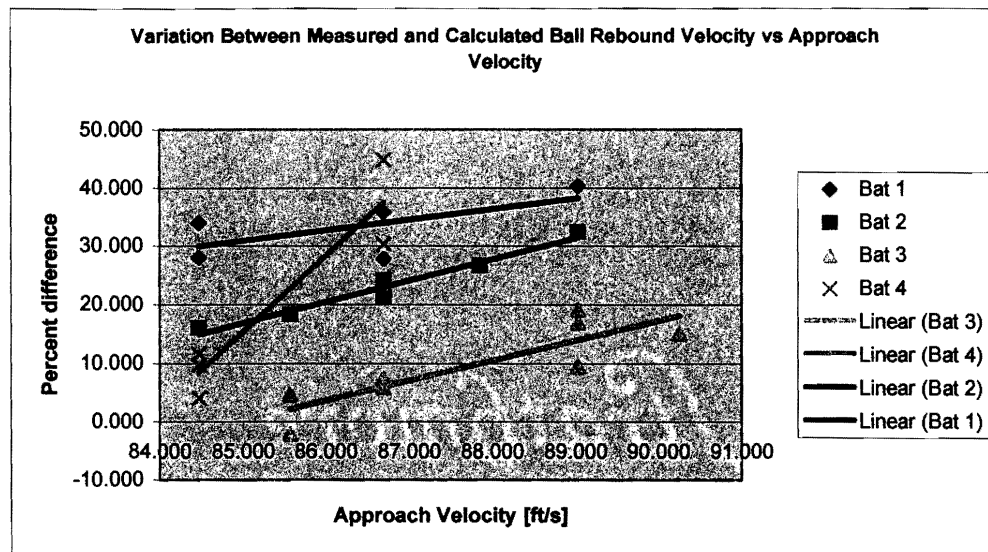


Figure 3.1- 1 Variation between Measured and Calculated Ball Rebound Velocity Versus Approach Velocity

The plot shows the variation between the measured and calculated rebound velocities plotted against the corresponding approach velocity. The regressions are Excel trend lines set for a linear fit.

The test results revealed that the rebound velocity of the ball calculated using the ASTM method was lower than the directly measured value. Consequently, the BPF calculated using the ASTM method was lower than the BPF calculated from the direct method. Furthermore, this discrepancy in the rebound velocity between the calculated and measured values increased with increasing approach velocity. Figure 3.1-1 shows

the percent difference between the calculated and measured ball rebound velocities plotted against the approach velocities, which ranged from 85 ft/s (25.9 m/s) to 91 ft/s (27.7 m/s). Note that the trend was consistent for four different bats and 24 test shots.

3.2 Conjectures

Two conjectures were made to account for the discrepancy in the rebound velocities. The first conjecture attributed the error to elastic deformation of the bat. It was presumed that the impact caused local deformation at the point of contact as well as transverse bending along the length of the bat. It was further presumed that energy was dissipated through vibration attenuation due to material damping. The second conjecture attributed the error to pin friction at the pivot. Although ball bearings were used, the pivot was not frictionless. It was presumed that a dissipative friction force caused the bat to decelerate immediately after the impact, thereby changing the momentum of the bat. The following sections investigate these two different possible explanations for the discrepancy in the rebound velocities.

3.3 Impact Theory

The motion of colliding bodies, or particles, is completely defined by conservation of momentum the coefficient of restitution (COR) [9]. The mathematical representations

of these principles are shown in equations (3.3.1) and (3.3.2), respectively, and the variables are defined in figure 3.3-1.

$$m_1 v_1 + m_2 v_2 = m_1 v_1' + m_2 v_2' \quad (3.3.1)$$

$$COR = \frac{v_2' - v_1'}{v_1 - v_2} \quad (3.3.2)$$

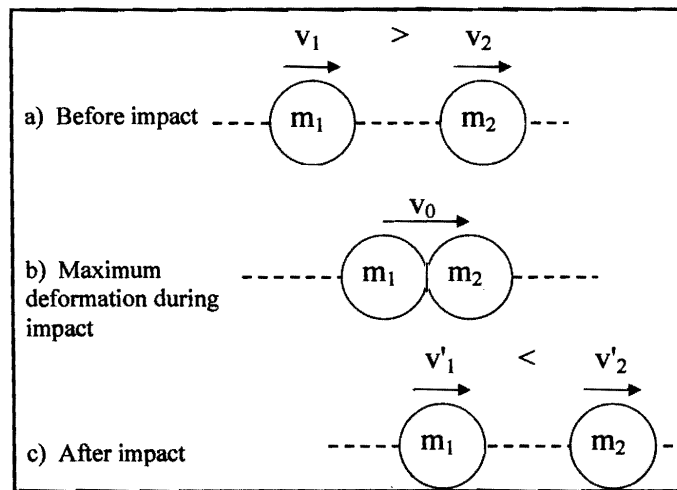


Figure 3.3- 1 Definition of Direct Central Impact of Particles

Direct central impact is defined as impact in which the magnitude of particle velocities are as shown in the figure and the contact forces are directed along the line of centers [9].

Equation (3.3.1) is the equation for the conservation of linear momentum and states that the momentum of the particles before impact must equal the momentum of the particles after impact. This is true only in the absence of external forces. In an impact

all contact forces are equal and opposite and internal to the system. Consequently no external forces exist and momentum is conserved [9].

Equation (3.3.2) is the equation for the COR and reflects the capacity of the colliding bodies to recover from the deformation caused by the contact forces. A COR value of 1.0 exemplifies a perfectly elastic impact in which the capacity for the particles to recover equals their capacity to deform. A COR value of 0 exemplifies an inelastic or plastic impact in which particles cling together after collision. In other words, a perfectly elastic impact represents zero energy loss while a plastic impact represents maximum energy loss [9].

The analysis in this chapter was done using mechanism simulation software called Working Model from Knowledge Revolution; a screen shot is shown in figure 3.3-2. This graphics based analysis tool allows mechanisms to be assembled using simple, geometric shapes such as circles and rectangles. Each enclosed area, called a body, invokes a dialogue box where inertial and material properties can be defined. A common method to assemble a mechanism from multiple bodies is to connect the bodies with pin joints. This is done by defining points on adjacent bodies and then joining these points.

Once a mechanism is completed, inputs such as forces or initial velocities can be assigned to the bodies or the defined points on the bodies. During the simulation Working Model calculates the kinematic and kinetic variables for each body and defined

point. These include position, velocity, acceleration, as well as reaction forces and torques. These variables can be used in equation boxes to calculate other quantities. Furthermore, the time response of all the variables can be viewed numerically or in the form of graphs. When more complex calculations are required, the simulation data can be exported as text files and processed with Matlab. This facilitated lengthy or repetitive calculations.

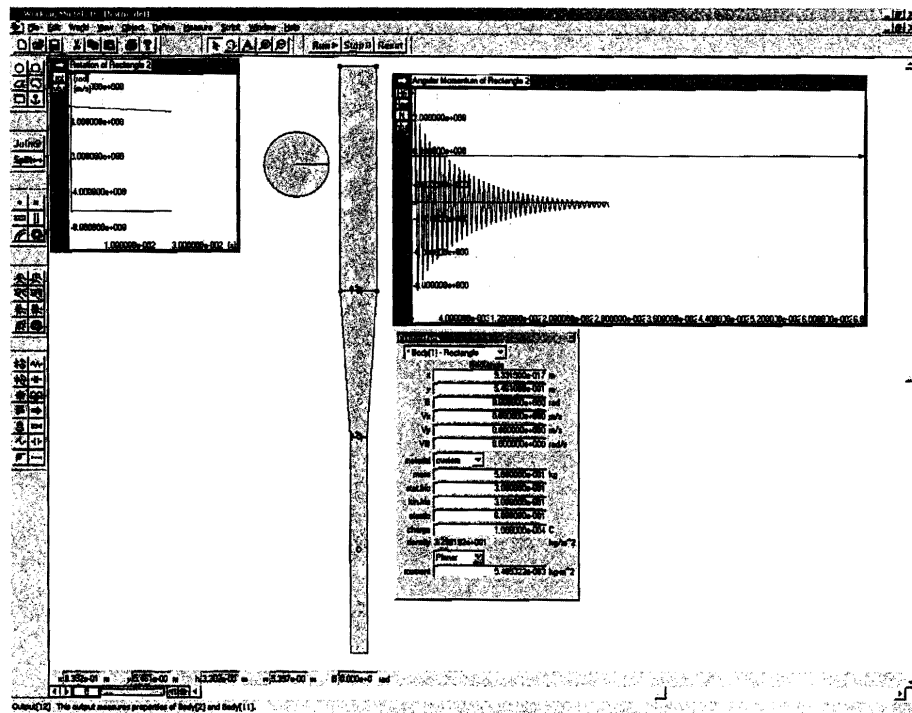


Figure 3.3- 2 Screen Shot of Working Model Environment

The figure shows the model of the bat, a graph of the response, and the dialogue box used to define the properties of the bodies.

3.4 Simple Model

Before simulating the bat-ball system a simpler model was tested to verify the impact theory in Working Model as well as provide insight on the effects of springs and dampers on the system response. The simple model consisted of two, 2-kg blocks with their centers connected with a spring and a damper. With gravity deactivated, a 1-kg mass was fired at the initially stationary blocks with a velocity of 20 m/s. The model is shown in figure 3.4-1.

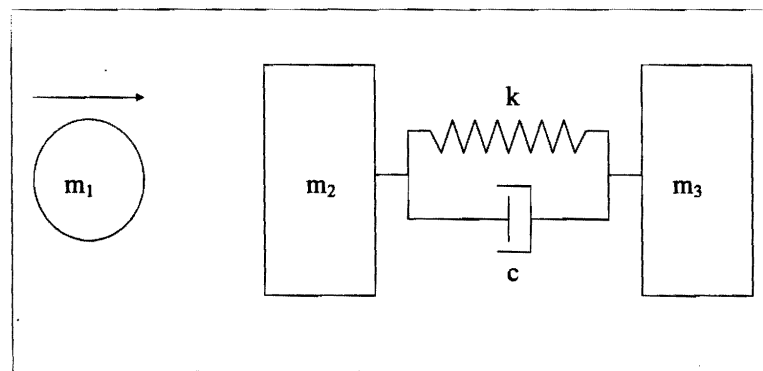


Figure 3.4- 1 Schematic of Simple Impact Model

The simple impact model was used to test the effects of spring, k , and damper, c , on the motion of the masses.

It is important to note that in Working Model a COR was defined for each body in the system; however, Working Model takes the smaller COR value of the two colliding bodies as the COR of the system. The default COR value of 0.5 was defined for all of the bodies in the system. The COR and the initial and final linear momentum were calculated in the Working Model with the generated velocity data.

Given that:

$$m_1 = 1 \text{ kg} \quad m_2 = 2 \text{ kg} \quad m_3 = 2 \text{ kg} \quad v_1 = 20 \text{ m/s} \quad v_2 = 0 \text{ m/s} \quad COR = 0.5$$

Equations (3.3.1) and (3.3.2) are as follows:

$$m_1 v_1 + m_2 v_2 = m_1 v_1' + m_2 v_2' \Rightarrow 20 \text{ kg m/s} = v_1' + 2v_2'$$

$$COR = \frac{v_2' - v_1'}{v_1 - v_2} \Rightarrow 10 \text{ m/s} = v_2' - v_1'$$

$$\boxed{v_1' = 0 \quad v_2' = 10 \text{ m/s}}$$

Calculating the velocities using the COR and the conservation of momentum equations resulted in a final velocity of 0.0 m/s for m_1 and 10 m/s for m_2 . According to the theory, the impact happens so quickly that there was no time for the impulse to be transferred to m_3 . These results were verified with Working Model. Figure 3.4-2 shows a screen shot of the simulation. The first plot shows the calculated COR, which is constant at the defined value of 0.5. The second plot shows the initial and final linear momentum plotted on the same axis. Note that they are exactly equal. The third plot shows the velocity of m_1 going to zero immediately after impact. The fourth plot shows the velocity of m_2 (blue line), the velocity of m_3 (red line), and their average velocity (black line).

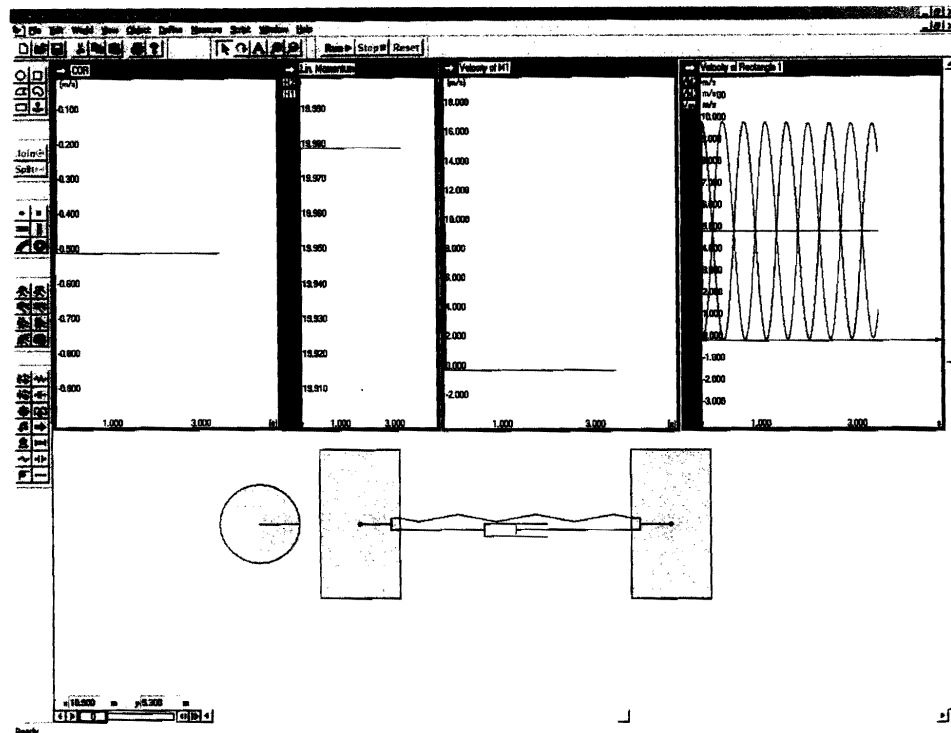


Figure 3.4- 2 Screen Shot of Working Model Simulation of the Simple Impact Model

The model essentially verified that all the principles of impact were obeyed in Working Model.

The response illustrated that immediately after impact m_2 attained the expected velocity of 10 m/s. However, the spring and damper transferred its momentum to m_3 . As the plot shows, m_2 and m_3 were exactly 180 degrees out-of-phase. Consequently, the velocity of their centers of gravity was constant at 5 m/s.

The simulation also verified that the COR was constant and the linear momentum was conserved for all time. The only effects of the spring and damper were to change the period of oscillation of m_2 and m_3 and the decay rate, respectively.

3.5 Bat Model

3.5.1 Model Assembly

The bat model was composed of three sections, or bodies: the barrel section, the tapered section, and the handle section. The mass of each section was determined by tuning their relative magnitudes—subject to the total mass—until the correct moment of inertia about the pivot was achieved.

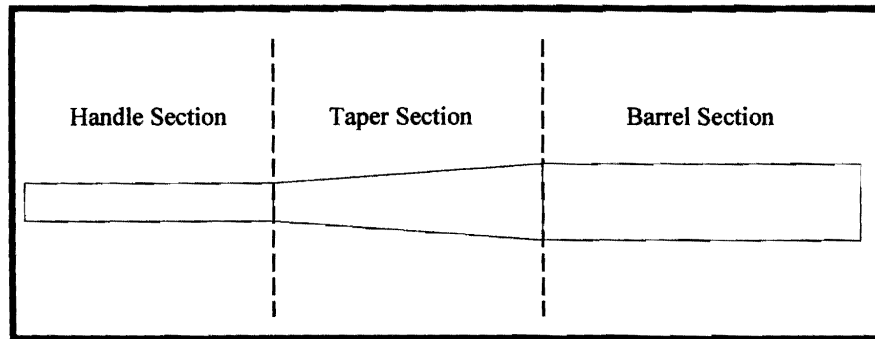


Figure 3.5- 1 Partitioning the Bat for the Elastic Model

This partitioning of the bat was done to allow for relative motion between the sections, thus representing elasticity.

In the ASTM standard [1] the moment of inertia of the bat was determined by measuring the natural frequency of the bat oscillating in the vertical plane. The resulting natural frequency was then used with the center of mass of the bat and the acceleration of gravity to calculate the moment of inertia of the bat about the pivot. The geometric terms used in this section as well as the method used to determine the moment of inertia can be found in section 2.1.2. Equation (3.5.1) relates the period of oscillation in

vertical plane to the mass and moment of inertia of the bat. To verify the model of the bat, the vertical swing test was simulated in Working Model; *see* figure 3.5-2. Comparing the natural frequency of the simulated data with the natural frequency of the actual data provided a direct indication of correspondence of the moment of inertia of the model and the actual bat.

$$Period = \frac{2\pi}{\omega_n} = \frac{2\pi}{\sqrt{\frac{(BP-6)M_{bat}g}{I}}} \quad (3.5.1)$$

ω_n	natural frequency (rad/s)
Period	oscillation period (s)
BP	location of the balance point (in)
M_{bat}	bat mass (oz)
G	gravitational constant (386 in/sec ²)
I	bat moment of inertia about the pivot point (oz-in ²)

The three sections of the bat were connected with pin joints to simulate an elastic body. At the pin between adjacent bodies rotational springs and dampers were attached; *see* figure 3.5-3. These elements generated reaction torques proportional to the relative angular rotation and relative angular velocity, respectively. This construction was analogous to the spring and damper between the two blocks in the simple model. A pin joint was placed at the location corresponding to the pivot of the actual structure. This pin joint initially had no damping.

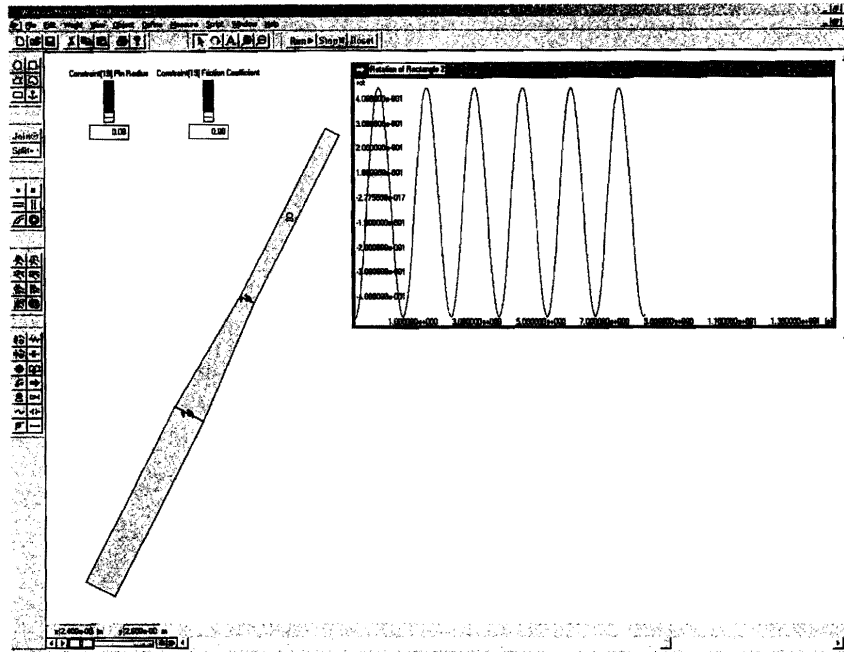


Figure 3.5- 2 Working Model Vertical Swing Test Simulation

The figure shows the bat in its displaced initial position. When the simulation is started, the bat swings in the vertical plane due to gravity. The oscillation is recorded in the plot to the right. With this data the natural frequency of oscillation could be calculated.

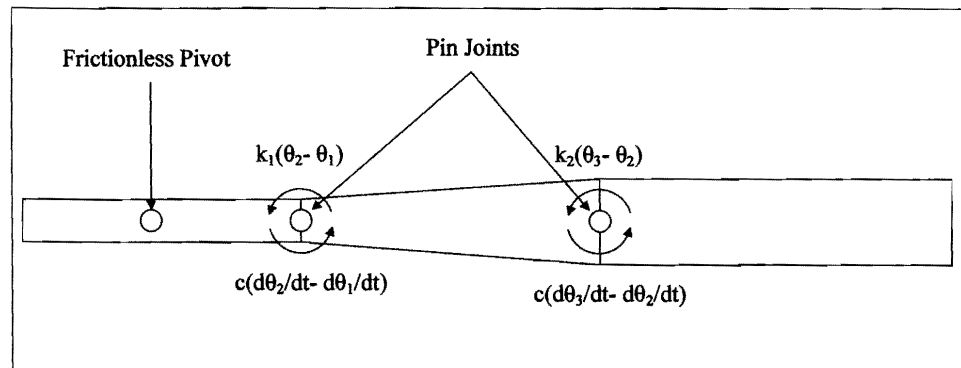


Figure 3.5- 3 Schematic of Elastic Bat Model

The bat was divided into three sections then reassembled with pin joints, rotational springs and dampers.

Section 3.5.2 shows the development of the rotational stiffness and damping coefficient used in the model. It should be noted that the resulting parameters were purely characteristic values and not intended to perfectly model the actual bat. The Working Model bat model was a two-dimensional, three-degree-of-freedom representation of a three-dimensional, continuous body with complex material properties.

The generated velocity data will be strictly used to compare the direct rebound velocity and the rebound velocity calculated using the ASTM method. In Working Model, the direct ball rebound velocity is based on the theoretical impact theory. That is, Working Model calculates the rebound velocity of the mass of the ball, the mass of the barrel section of the bat, the coefficient of restitution defined in the properties box, and the defined ball approach velocity. This statement was proven with the simple impact model and was based upon the fact that no forces were transferred through the spring or damper during impact. Consequently, the impact involves only the ball and the barrel section. To represent the ASTM method, the rebound velocity will also be calculated by applying conservation of angular momentum with the bat recoil velocity from the simulation. Therefore, velocity comparisons are based exclusively on simulation data.

Comparison of the analytical model with experimental data will be limited to percent differences in the rebound velocity and BPF between the direct method and the ASTM method.

3.5.2 Rotational Stiffness

As a first approximation the rotational stiffness of the springs was calculated using the flexural equation for a cantilevered beam; *see* figure 3.5-4. Differentiating the expression for vertical deflection gave an expression for the angular rotation as a function of the distance from the applied load. The relation for the rotational stiffness was the applied torque divided by the angular rotation. Carrying out this operation provided an expression for the rotational stiffness as a function of the distance from the applied load. This expression was only an approximation for the bat stiffness that took into account spatial and cross sectional geometry; *see* equation (3.5.2) [14].

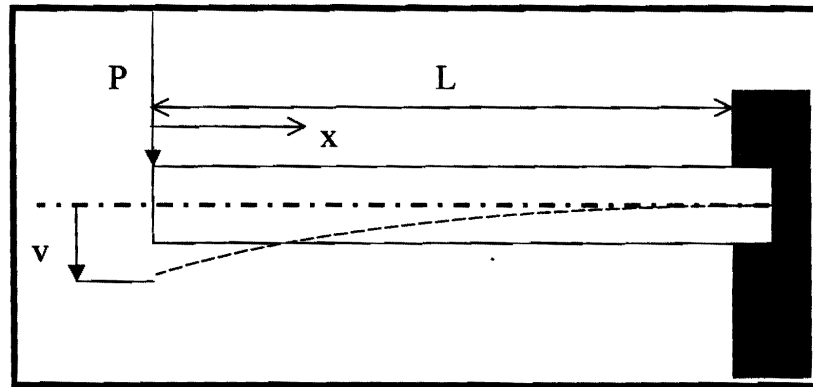


Figure 3.5- 4 Rotational Stiffness Beam Model

The schematic shows cantilevered beam subject to a load P. Note that distance x is measured from the point of application of the load.

$$v = \frac{P}{6EI} (2L^3 - 3L^2x + x^3) \quad (3.5.2)$$

$$\theta = \frac{dv}{dx} = \frac{P}{6EI} \frac{d}{dx} (2L^3 - 3L^2x + x^3) = \frac{P}{6EI} (-3L^2 + 3x^2) \quad (3.5.3)$$

$$k_{\theta} = \frac{T}{\theta} = \frac{PL}{\frac{P}{6EI} (-3L^2 + 3x^2)} = \frac{6EIL}{(-3L^2 + 3x^2)} \quad (3.5.4)$$

- v vertical deflection
- θ angular rotation
- T toque
- P load
- I area moment of inertia
- L distance from the load to origin
- X distance from load
- k_{θ} rotational stiffness
- E modulus of elasticity

Below is the calculation for the two rotational spring stiffnesses. The calculation used the elastic modulus of aluminum and the inertia expression for a solid cylinder.

$$E = 200 \text{ MPa}$$

$$d_1 = 0.0269875 \text{ m}; d_2 = 0.0127 \text{ m}$$

$$x_1 = 0.1854; x_2 = 0.4014$$

$$L = 0.56642 \text{ m}$$

$$I = \frac{\pi d^4}{4}$$

$$k_{\theta}(d_1, x_1) = 2.153 \cdot 10^6 \text{ Nm/rad}$$

$$k_{\theta}(d_2, x_2) = 0.158 \cdot 10^6 \text{ Nm/rad}$$

- d_1 diameter of barrel section
- d_2 diameter of handle section
- x_1 distance from load to beginning of taper
- x_2 distance from load to end of taper

3.5.3 Material Damping

The material damping was solved for through an iterative process. With an arbitrary value for the damping constant, the logarithmic decrement was determined from the

velocity time response and the damping ratio was calculated. The damping constant was tuned to provide a damping ratio of 0.01, which was a characteristic value for aluminum [17]. The iterative process yielded a damping ratio of 0.0089 for a damping constant of 0.6 Nms/rad.

3.5.4 Model Verification

To verify that the model was a reasonable representation of the actual system, the ball rebound velocity and the bat recoil velocity of the model were compared to experimental data. This information is summarized in table 3.5-1.

	Experimental Data	Simulation Data	% difference
Ball Approach Velocity [m/s]	26.30	26.30	0.00
Ball Rebound Velocity [m/s]	6.33	5.46	13.74
Bat Recoil Velocity [m/s]	9.43	9.81	-4.03

Table 3.5- 1 Comparison of Experimental and Simulated Velocity Data

The results show how well the model represented the actual data.

Table 3.5-1 shows good agreement for the bat recoil velocity, but the simulated ball rebound velocity was about 14 percent smaller than the measured value. However, the model was sufficient for the purposes of this analysis.

As in the simple model, conservation of momentum was verified by comparing the final angular momentum with initial angular momentum. Here, the total final angular

momentum was the sum of the final angular momentum of the three sections of the bat along with the angular momentum of the rebounding ball; *see* equation (3.5.3).

$$H_{final} = \sum \bar{I}_i \bar{\omega}_i + \sum m_i \bar{v}_i d \quad (3.5.3)$$

\bar{I} moment of inertia of bat section, or ball, about its center of gravity

$\bar{\omega}$ angular velocity of bat section, or ball, about its center of gravity

m mass of bat section or ball

\bar{v} center of mass velocity of bat section or ball

d distance from the center of pivot to the center of mass of bat section or ball

Figure 3.5-5 shows the plot of the individual components of angular momentum. For the initial and final angular momentum to equal each other, all components of angular momentum must be accounted for and defined in the proper direction. The simulation data showed that the rebounding ball had a small lateral component of velocity as well as a rotation about its center of mass. The equations below show all the necessary terms that must be accounted for in equation (3.5.3).

$$H_{Barrel} = \bar{I}_{Barrel} \bar{\omega}_{Barrel} + m_{Barrel} \bar{v}_{Barrel} d_{Barrel}$$

$$H_{Taper} = \bar{I}_{Taper} \bar{\omega}_{Taper} + m_{Taper} \bar{v}_{Taper} d_{Taper}$$

$$H_{Handle} = \bar{I}_{Handle} \bar{\omega}_{Handle} + m_{Handle} \bar{v}_{Handle} d_{Handle}$$

$$H_{ball} = \bar{I}_{ball} \bar{\omega}_{ball} + m_{ball} v_{ball,x} d_{ball,y} + m_{ball} v_{ball,y} d_{ball,x}$$

$$H_{final} = H_{Barrel} + H_{Taper} + H_{Handle} + H_{ball}$$

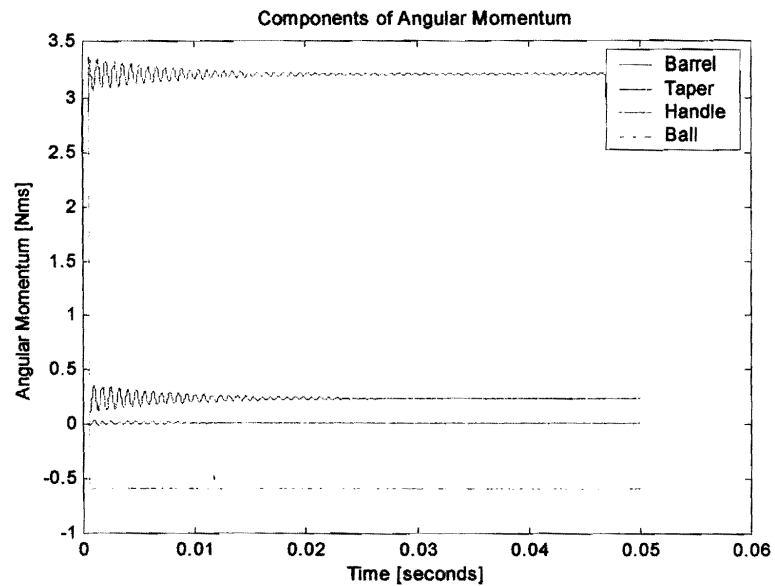


Figure 3.5- 5 Components of Angular Momentum in Elastic Model

The graph shows the initial and final angular momentum of the elastic bat model through 0.05 seconds after impact.

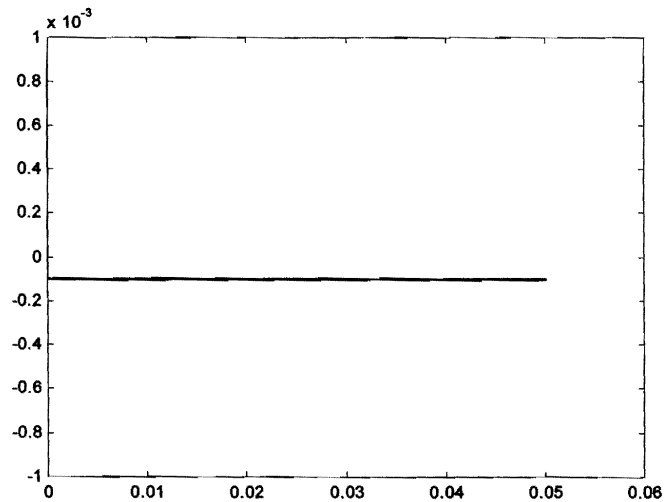


Figure 3.5- 6 Difference in Angular Momentum of Elastic Model

The graph shows a plot of the difference between the initial and the final angular momentum through 0.05 seconds after impact.

In figure 3.5-6 the difference between the initial and final angular momentum are plotted on the same axis. There appears to be a static offset on the order of 10^{-4} that was most likely attributable to insufficient numerical accuracy. Overall, the error between the initial and final angular momentum was 0.0035 percent.

3.5.5 Model Simulation

If a bat were perfectly rigid, every point of the bat would have the same angular velocity after impact. In which case the angular velocity could be measured anywhere along the bat. However, if a bat flexes, or exhibits elastic behavior, the velocity near the pivot would not equal the velocities at other locations on the bat. In section 3.5.4 spatial variations in velocity were accounted for by determining the angular momentum of each body separately before summing them together. That is, the final angular momentum of the model was calculated with the three independent angular velocities and three independent tangential velocities corresponding to the three bodies. Conversely, in the actual experiment, the final angular momentum of the bat was calculated with a single angular velocity defined by a 6-inch radial arm protruding from the pivot; *see* figure 3.5-7.

Therefore, to more accurately represent the measurement geometry of the actual experiment, the angular velocity of the handle section alone was used to define the angular velocity of the entire bat. That is, the final angular momentum of the bat was calculated with the moment of inertia of the full bat about the pivot and the angular velocity of the handle section. This simulation essentially analyzed the affects of

applying a rigid body analysis on an elastic member. If the bat was sufficiently rigid, the error in making this assumption should be small.

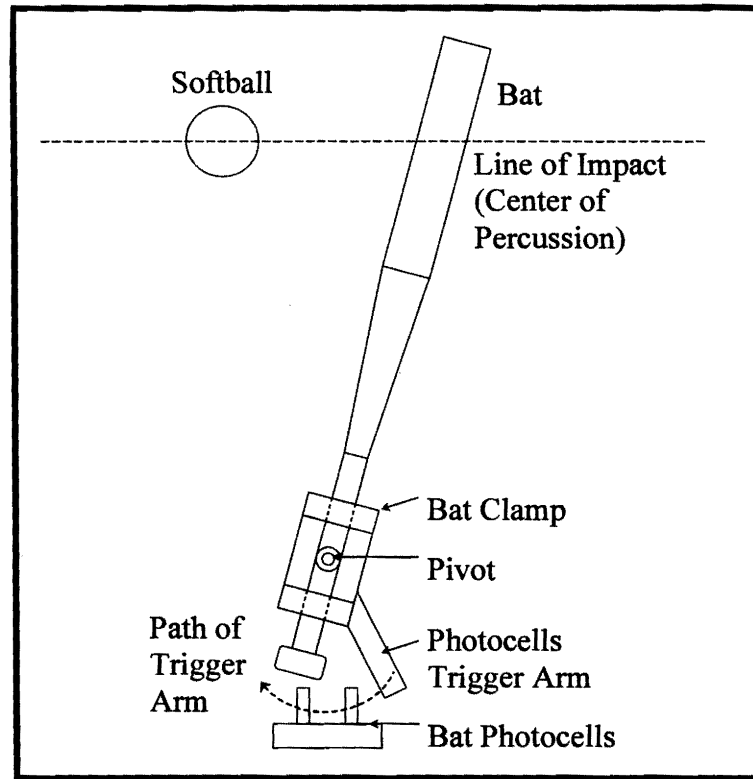


Figure 3.5- 7 Bat Pivot Assembly Schematic

The important feature is location of the velocity measurement. If the bat does not behave as a rigid body, there may be variations in angular velocity along its length.

For comparison, the initial and final angular momenta were plotted on the same chart. The response is shown in figure 3.5-8. The simulation revealed that the final angular momentum oscillated about an equilibrium value that coincided with the initial and final angular momentum. As the vibrations were attenuated the final angular

momentum settled towards the equilibrium value. At steady state, the angular momentum was perfectly conserved—the plots of the initial and final angular momentum overlapped exactly.

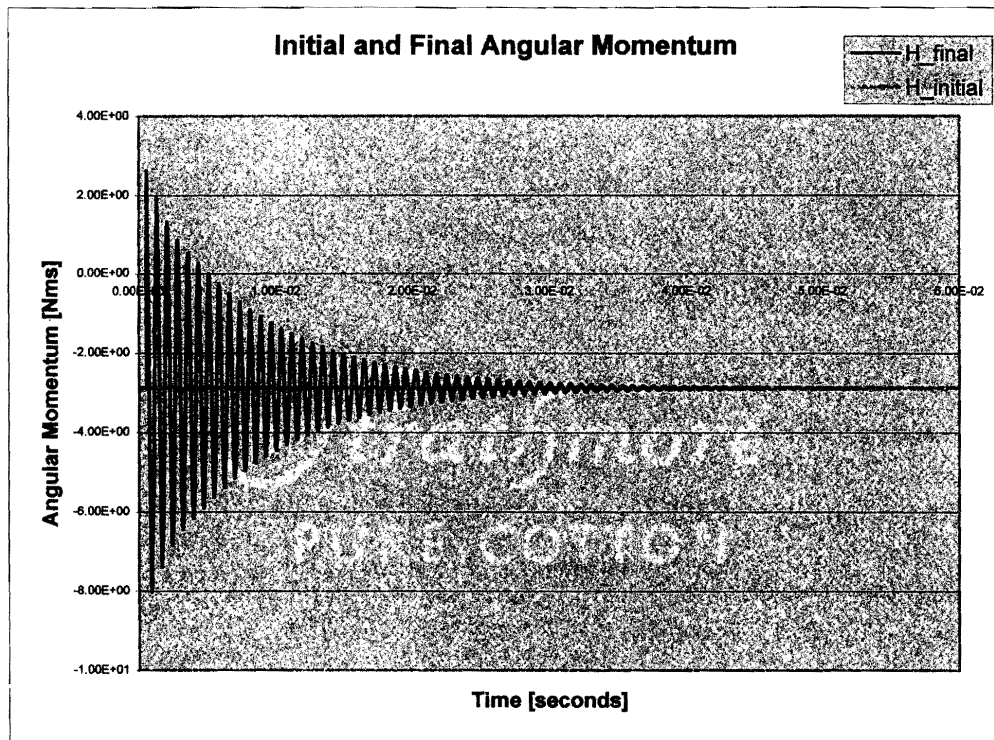


Figure 3.5- 8 Angular Momentum of Elastic Bat Model (frictionless pivot)

The plot shows the initial and final angular momentum of the system, using the angular velocity of the handle section to represent the angular velocity of the bat. Note the large error immediately after impact. At steady state, angular momentum was perfectly conserved.

The error between the initial and final angular momentum stemmed from the elasticity of the model. During the transient period after impact, the angular velocity of

The blue line is the barrel, the red line is the taper, and the black line is the handle. Note that handle section is 180 degrees out of phase with the other sections.

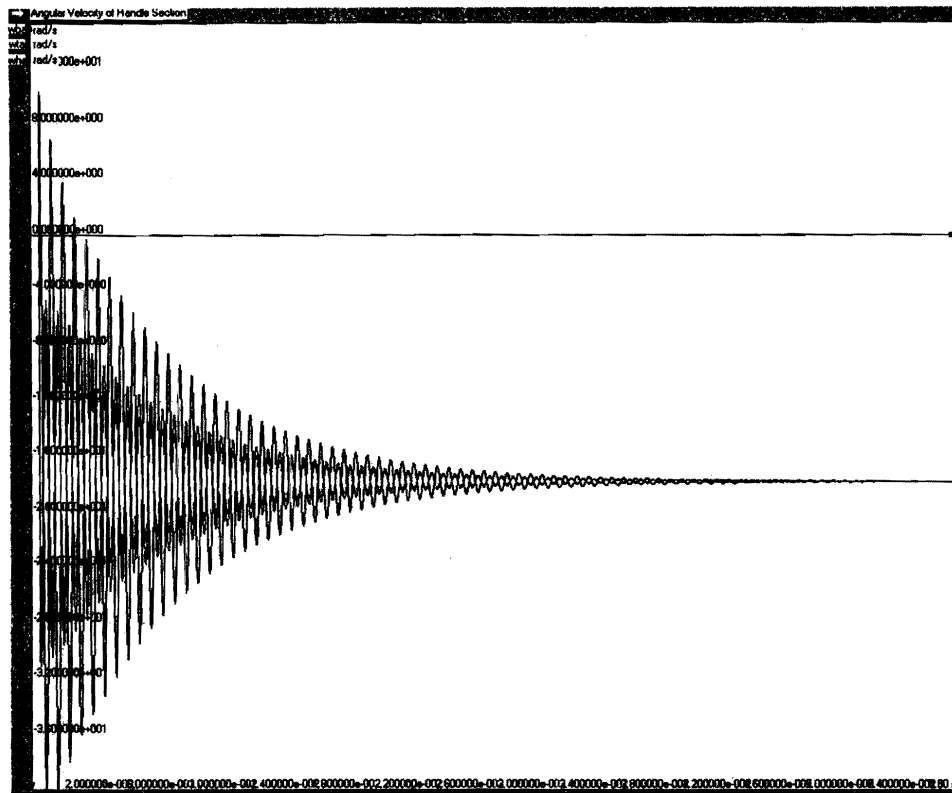


Figure 3.5- 10 Angular Velocity of Bat Sections at Steady State

This is the same signal as figure 3.5-9 but allowed to run to steady state. Note that three signals converge to the same angular velocity.

In section 3.5.4, the momentum of each body was calculated from the measured velocity of the body and then summed together. This effectively accounted for the distribution of angular momentum during the transient period.

However, while the angular velocities of the bodies exhibited large oscillations, the angular position of the bodies remained relatively stable; *see* figure 3.5-10. Note that the motion of the sections oscillated about a constant, equilibrium value that they converged to at steady state. This shows that the radial center of mass of the bat

rotated about the pivot at a relatively constant angular velocity. Figure 3.5-11 shows the angular position of the handle section (top) and the angular velocity of the handle section (bottom) after impact. The angular position is relatively smooth slope, which signifies a constant angular velocity.

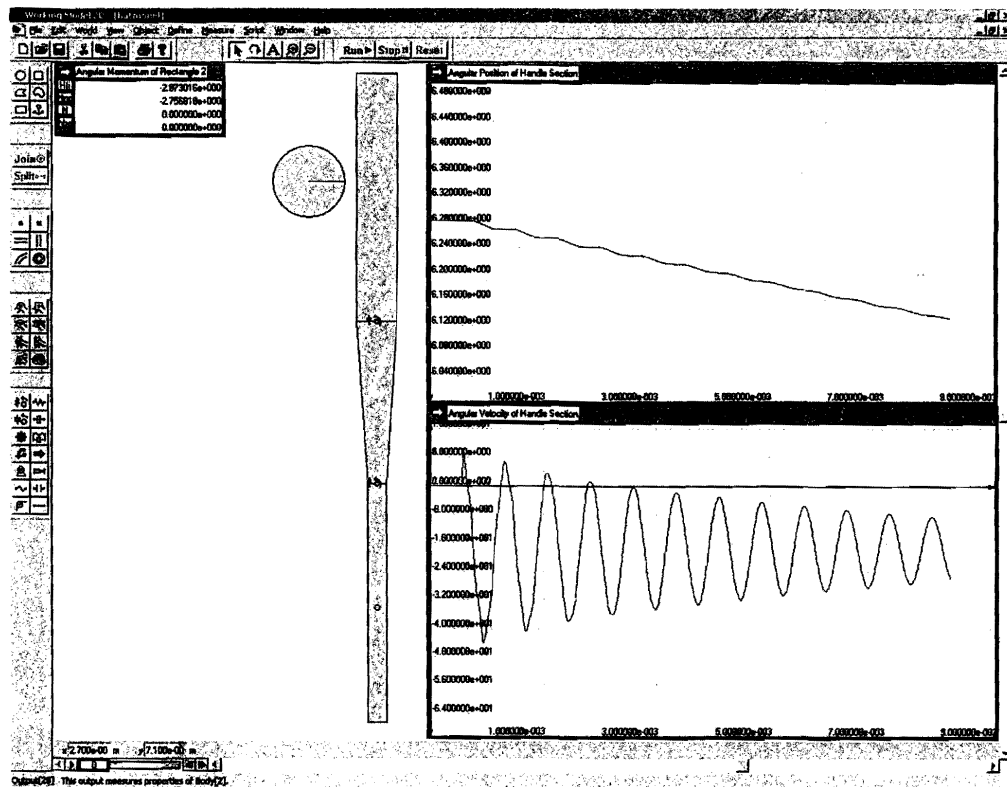


Figure 3.5- 11 Comparison of Angular Position and Angular Velocity

The upper plot shows the angular position of the handle section and lower plot shows the angular velocity of the handle section. The angular position has significantly smaller amplitude oscillations.

Consequently, using the angular position data to calculate an average velocity bypassed the transient error associated with the instantaneous velocity data.

$$\omega_{Bat} = \frac{\theta(t_2) - \theta(t_1)}{t_2 - t_1}$$

$$t_1 = 0.02s \quad \theta(t_1) = 5.919 \text{ radians}$$

$$t_2 = 0.05s \quad \theta(t_2) = 5.369 \text{ radians}$$

$$\omega_{Bat} = 18.33 \text{ rad/s}$$

This velocity was then compared to the steady state velocity of the system when all the oscillations had been damped out.

$$(\omega_{Bat})_{Steady-State} = 18.37 \text{ rad/s}$$

Using the angular position data to calculate the angular velocity the bat only caused a 0.2-percent error from the steady state angular velocity, where angular momentum was perfectly conserved.

In summary, introducing elasticity into the system caused the sections of the bat to oscillate at a high frequency but the displacements of these oscillations were small. Consequently, using the angular velocity of the handle section to define the angular momentum of the bat introduced transient errors. However, because the amplitude of the body oscillations was small, angular position of the sections proved to be a stable quantity even immediately after impact. Calculating the average angular velocity from

displacement data significantly diminished the error associated with the high frequency oscillation of the velocity data.

The difference in the BPF, calculated with the simulation data, between the two methods was only a few tenths of a percent. Consequently, the first conjecture accounting for the discrepancy in the BPF between the ASTM method and direct method was disproved. Vibrations of the bat were not the cause for the discrepancy in the BPF between the ASTM method and the direct method.

3.6 Bat Model with Pin Friction

3.6.1 Friction Characterization

For the next analysis damping was added to the pivot, creating an external friction force that would change the momentum of the system. The first step involved analyzing the nature of the friction force; that is, it was necessary to determine whether the ball bearings in the pivot generated coulomb damping or viscous damping. Once the type of damping was determined, the corresponding damping constant had to be extracted. The damping was analyzed with the set up used in determining the moment of inertia of the bat—using the potentiometer to measure the free-decay response from the vertical swing test.

To accurately represent this damping force, the vertical swing test was simulated with a pin friction applied to the pivot. Both viscous damping and coulomb damping were compared to the experimental data. The comparison plot is shown in figure 3.6-1.

Through an iterative process, the friction coefficients were tuned until the first peak matched the amplitude of the experimental data. The final value for the coulomb friction coefficient was 0.46 and the final viscous damping coefficient was 0.09 Nms/rad. Figure 3.6-1 shows that coulomb damping was a closer match to the experimental data.

This method of determining the friction coefficient provided a sufficient approximation to the actual system. Although a more rigorous derivation was possible, a precise value was not necessary for this level of analysis.

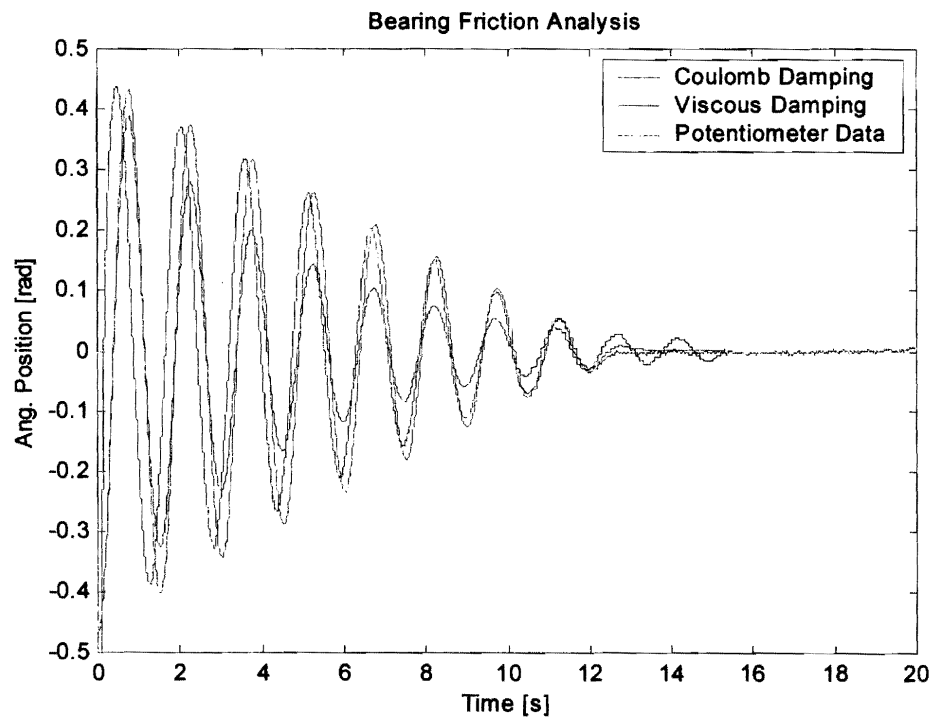


Figure 3.6- 1 Damping Calibration

This plot shows the experimental damped, free-response and the simulated damped, free-responses with viscous and coulomb damping. The coulomb damping better represents the actual decay.

In Working Model, the coulomb damping torque was calculated with the constraint force at the pin and the defined friction coefficient; *see* equation (3.6.1).

$$T_{friction} = -r_{pin} \mu |F_{constraint}| \frac{\omega_{rel}}{|\omega_{rel}|} \quad (3.6.1)$$

r_{pin}	radius of pivot
μ	friction coefficient
$F_{constraint}$	constraint force at the pivot
ω_{rel}	relative angular velocity between the pivot and the bat handle

$\frac{\omega_{rel}}{|\omega_{rel}|}$ is essentially the sign function, which, along with the minus sign, causes the friction torque to always oppose the motion of the bat. Further, the constraint force at the pin of a rigid body under fixed-pivot rotation is proportional to the square of the angular velocity of the inertia; *see* equation (3.6.5) [9].

$$\bar{F}_{constraint} = \bar{F}_x + \bar{F}_y \quad (3.6.2)$$

$$\bar{F}_n = \bar{F}_x + \bar{F}_y \quad (3.6.3)$$

$$F_n = mR\omega^2 \quad (3.6.4)$$

$$\boxed{\bar{F}_{constraint} = mR\omega^2} \quad (3.6.5)$$

Equation (3.6.2) states that the constraint force is equal to the vector sum of the vertical and horizontal reaction forces. From the free body diagram in figure 3.6-2, the reaction forces are equal to normal force acting between the rod R and the mass m.

Since the rod can only provide a force in its axial direction. The normal force F_n must equal the normal component of the inertial force of the rotating mass.

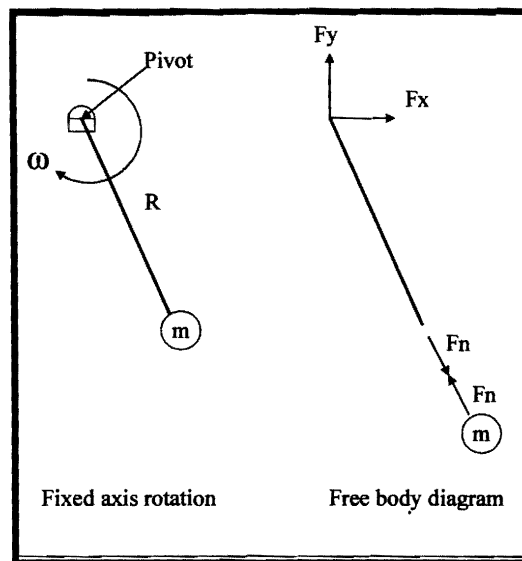


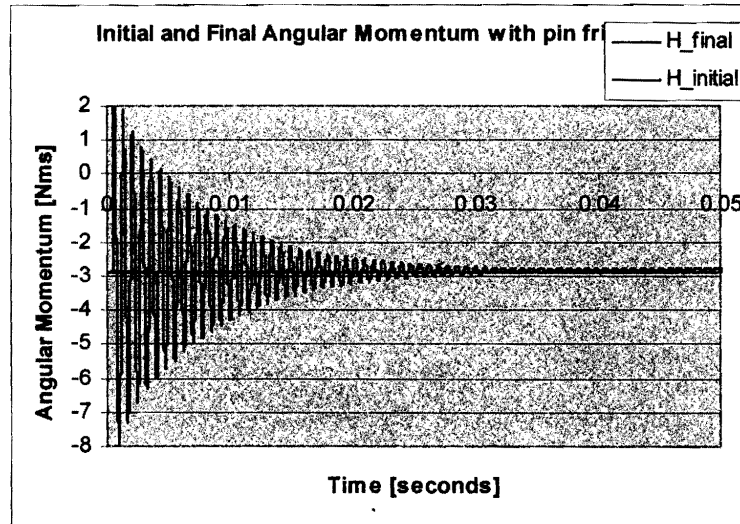
Figure 3.6- 2 Constraint Force for Fixed Axis Rotation

The figure the right shows a mass rotating about a fixed axis. The figure on the left shows the free body diagram of the system. F_y and F_x are the vertical and horizontal constraint forces, respectively. F_n is the normal force acting on mass, m .

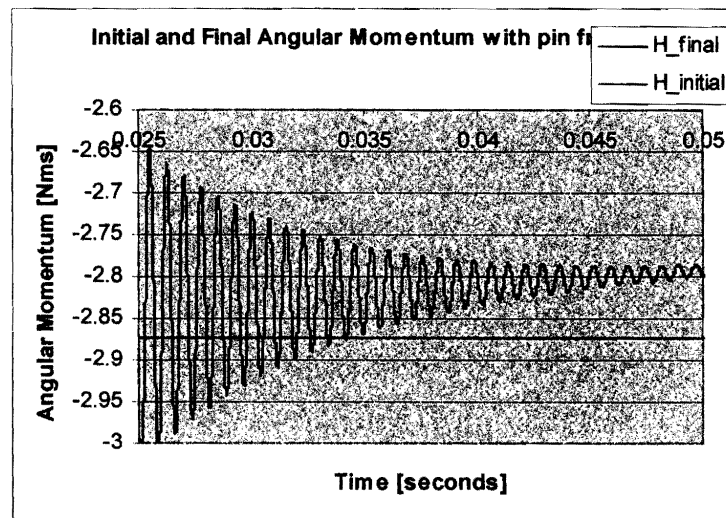
3.6.2 Friction Model Simulation

The pin friction was applied to the elastic bat model and the angular momentum of the impact response was analyzed. Like in the frictionless model, the initial and final angular momenta were plotted on the same axis for comparison; see figure 3.6-3. The transient response of the final angular momentum resembled the frictionless model, exhibiting large oscillations about the initial angular momentum. The effects of the pin

friction were apparent at steady state, where there was an offset between the initial and final angular momentum.



(a)



(b)

Figure 3.6- 3 Angular Momentum of Elastic Bat Model (with pin friction)

Figure (a) shows the full time span and (b) shows a close-up near steady state. Note the offset between the initial and the final angular momentum.

	% Difference in Rebound Velocity
No Friction	0.36
Coulomb Pin Friction	15.52

Table 3.6- 1 Rebound Velocity Error of Model with and without Friction

The table shows the percent difference between the direct rebound velocity and the rebound velocity calculated using the ASTM method for the simulation data with and without friction.

Table 3.6-1 shows the percent difference in the ball rebound velocity between the ASTM method and the direct method for the Working Model simulation with and without pin friction.

With friction the bat system must be described as an impulse-momentum problem where the final momentum is the sum of the initial momentum and the applied impulse. Therefore, the initial angular momentum was divided between the sections of the bat as well as dissipation through pin friction. Diminishing the recoil velocity of the bat was the net effect of the friction force. Equation (3.6.3) shows the ball rebound velocity from the impulse-momentum problem.

$$H_{\text{initial}} + \int_{t_0}^{t_f} M_{\text{ext}} dt = H_{\text{final}}$$

$$H_{\text{final}} = H_{\text{initial}} + \int_{t_0}^{t_f} M_{\text{ext}} dt$$

$$m_{\text{ball}} v_{\text{ball},2} R_{\text{COP}} + I_{\text{bat}} \omega_{\text{bat}} = m_{\text{ball}} v_{\text{ball},1} R_{\text{COP}} + \int_{t_0}^{t_f} M_{\text{external}} dt$$

$$m_{\text{ball}} v_{\text{ball},2} R_{\text{COP}} = m_{\text{ball}} v_{\text{ball},1} R_{\text{COP}} - I_{\text{bat}} \omega_{\text{bat}} + \int_{t_0}^{t_f} M_{\text{external}} dt$$

$$v_{\text{ball},2} = v_{\text{ball},1} - \frac{I_{\text{bat}} \omega_{\text{bat}}}{m_{\text{ball}} R_{\text{COP}}} + \int_{t_0}^{t_f} M_{\text{external}} dt \quad (3.6.6)$$

H_{initial}	initial angular momentum
H_{final}	final angular momentum
M_{ext}	external moments
m_{ball}	ball mass
R_{COP}	distance from the pivot to the center of percussion of the bat
I_{Bat}	moment of inertia of the bat
ω_{Bat}	angular velocity of the bat
$v_{\text{Ball},1}$	velocity of the bat before impact
$v_{\text{Ball},2}$	velocity of the bat after impact

The external moment is the additional friction term defined by equation (3.6.6).

3.7 Error as a Function of Approach Velocity

The next goal of the simulation was to model or recreate the trend in the ball rebound velocity with increasing approach velocity. Recall that the error in the rebound velocity, between the measured and calculated values increased with increasing approach

velocities. The approach velocities tested were 85, 86, 87, 88, 89, 90, and 91 ft/s, corresponding to the ± 3 ft/s about 88 ft/s. For this analysis, the Working Model data were exported to a file and then loaded into Matlab for processing.

7000 samples were taken with a sampling period of 0.00001 seconds, providing 0.07 seconds of data—with 1000 data points corresponding to 0.01 seconds. The Matlab m-file calculated the angular velocity of the handle section using the i -th and the $(i+3000)$ -th sample of the angular position data. This routine calculated the angular velocity at 0.3-second intervals, providing the angular velocity as a function of time for 0.04 seconds. The routine was executed for the data at each of the approach velocities and plotted the results together. The plot illustrated the transient oscillations due to the time lag of the momentum transfer as well as the deceleration of the bat due to pin friction.

Figure 3.7-1 shows the angular velocity of the bat, calculated as described above, for the range of approach velocities with and without pin friction. After the transient vibrations were attenuated, the angular velocity of the handle section remained constant in the frictionless model while in coulomb damped model the angular velocity decreased immediately after impact and continued to decline as the transient vibrations were attenuated.

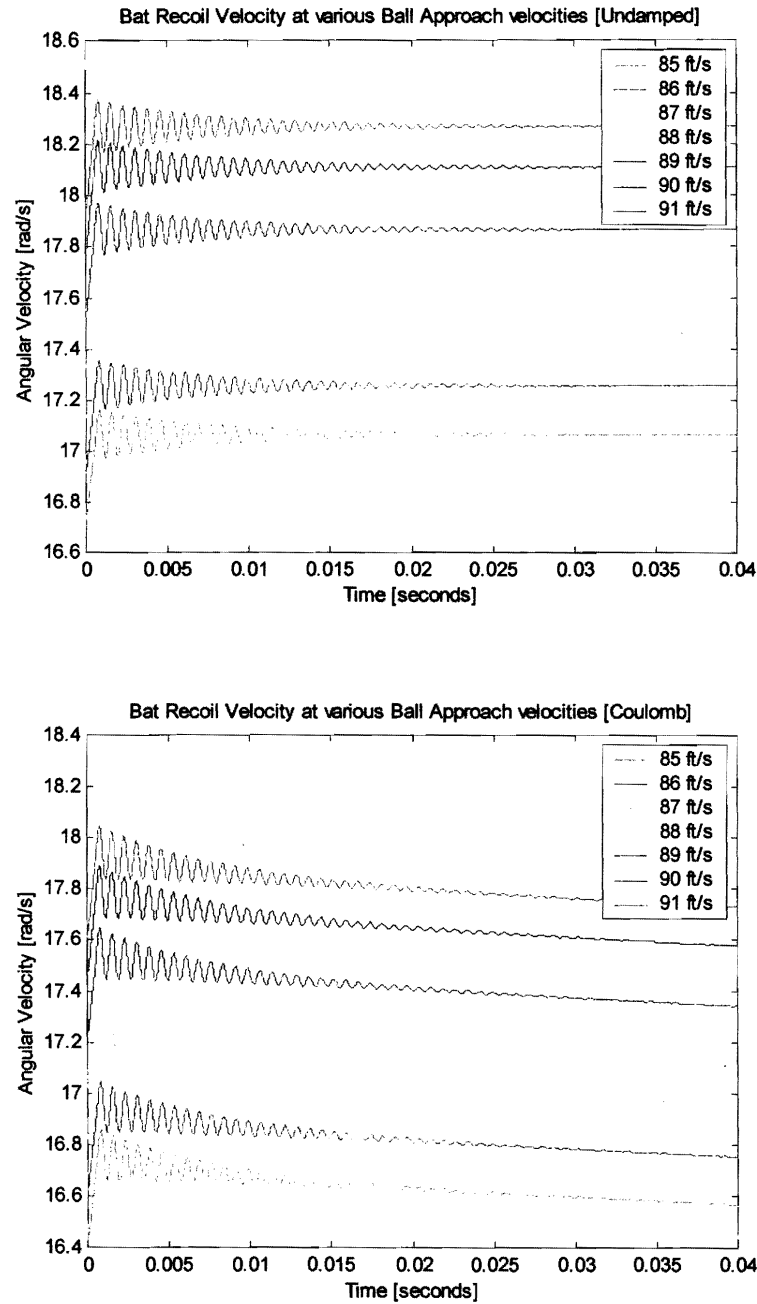


Figure 3.7- 1 Angular Velocity of Bat (with pin friction)

These velocities were calculated with angular position data over 0.03-second intervals throughout the data set. The top graph on depicts the frictionless pivot and the bottom graph depicts the pivot with coulomb damping. Note that after the transient oscillation the damped model continues to decrease while the frictionless model becomes constant.

The Matlab m-file also extracted the angular velocity of the handle section calculated between $t = 0.02$ seconds and $t = 0.05$ seconds, corresponding to the instances when the bat positions were measured in the actual experiment. The angular velocity calculated between $t = 0.04$ seconds and $t = 0.07$ seconds was also extracted to examine the response when the bulk of the transient vibrations were attenuated.

These velocities were used to calculate the rebound velocity of the ball with the conservation of angular momentum equation. The calculated values were compared to the actual rebound velocity, as calculated from Working Model, primarily defined by the COR of the system. The percent differences between the velocities were plotted against the approach velocities to examine the trends.

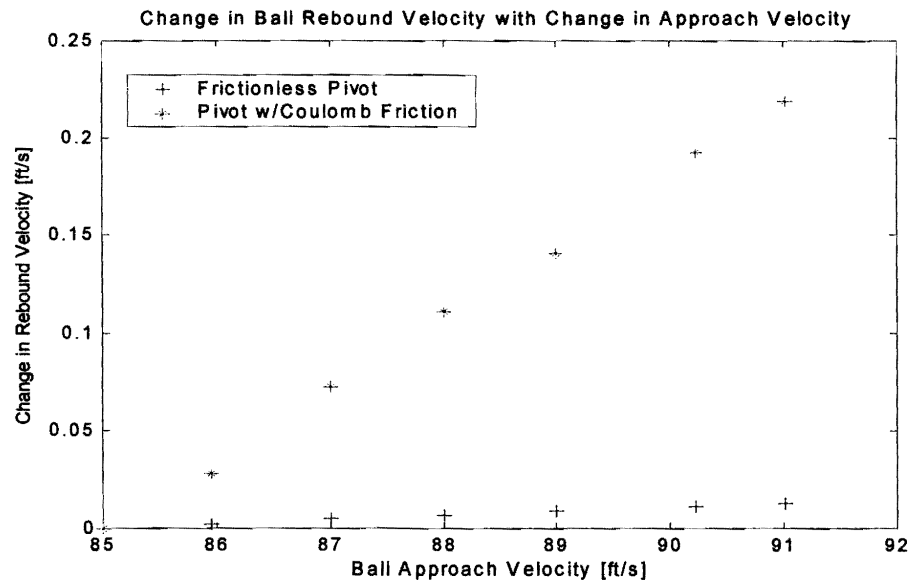


Figure 3.7- 2 Change in Rebound Velocity with Approach Velocity

This plot shows the trend for the model with and without pivot friction. The undulations are due to sampling error of the minor oscillations of the angular position data.

Figure 3.7-2 shows the error in the ball rebound velocity as a function of approach velocity for the models with and without pin friction. The errors were normalized to start at zero. The friction model clearly exhibits an increasing error with increasing approach velocity. In the frictionless model, however, the trend reflects only the sampling error associated with small amplitude undulation of the angular position measurement. Note that this undulation is seen in the friction model response as well.

The trend in the model with friction was attributed to the nature of the coulomb friction force at the pin. As described in section 3.6.1, the friction force was proportional to the square of the angular velocity of the body. A higher approach velocity translated into a higher recoil velocity. Consequently, a higher recoil velocity caused a higher normal reaction force at the pin, thereby dissipating more energy through the resulting friction torque at the pivot.

3.8 Results and Conclusions

This analysis deduced that the discrepancy in the ball rebound velocity between the ASTM method and direct method was attributed to friction at the pivot. Percent difference results of the analytical model and the experimental data are summarized in tables 3.8-1 and 3.8-2.

	% Difference in Vball2
Bat 1	33.24
Bat 2	23.59
Bat 3	9.48
Bat 4	20.95
Working Model bat w/friction	15.50

Table 3.8- 1 Rebound Velocity Error for Experimental and Analytical Results

The table shows the percent difference in the ball rebound velocity for the four bats tested as well as for the analytical model with coulomb friction at the pivot.

	% Difference in BPF
Bat 1	13.32
Bat 2	8.44
Bat 3	3.33
Bat 4	4.16
Working Model bat w/friction	5.64

Table 3.8- 2 BPF Error from Experimental and Analytical Results

The table shows the percent difference in the BPF for the four bats tested as well as for the analytical model with coulomb friction at the pivot.

Table 3.8-1 compares the percent differences in the ball rebound velocity between the ASTM method and the direct method for the four bats tested and the analytical model. Table 3.8-2 compares the corresponding BPF percent differences. The results show that the model with friction gave values that were in the same range as the experimental data.

Measurement of the ball rebound velocity using the direct method eliminated the need to apply conservation of angular momentum and, thus, the need to account for all the components of the system, such as the external moment caused by the friction. Neglecting friction does affect both methods because it effectively changes the momentum, and therefore, the velocity of the bat. The error in BPF associated with this change in bat velocity is minimal in the direct method. However, this same error is magnified when the bat velocity is used to derive the ball rebound velocity in the ASTM method.

Chapter 4: Summary and Conclusion

This project of developing the bat performance factor (BPF) test designed by the ASTM consisted of three phases. The first phase involved developing the test equipment for the experiment, including designing a precision ball launcher, a bat pivot stage, and all the instrumentation for velocity measurement. The main challenge was designing and fabricating the ball launcher. The final revision of the device was a pneumatic cannon with the structural characteristics of a commercial hydraulic cylinder. An important feature of the design was the lightweight sabot that cradled the ball during launching. With the precision design and careful planning, the cannon satisfied all the specifications set by the ASTM. Furthermore, the design allowed the ball rebound velocity to be measured directly.

Phase two involved a careful analysis of the BPF equation and the collection of velocity data to make the calculation. The ASTM method essentially used conservation of angular momentum to derive the ball rebound velocity from the other velocities. Consequently, the BPF involved the ball approach velocity, the bat recoil velocity, and several geometric and inertial terms. The analysis further revealed that the BPF was very sensitive to measurement errors. That is, the BPF calculated using the ASTM method had magnification factors that were between 2 and 3. Consequently, an error in the moment of inertia, for example, of 5 percent caused an error in the BPF of almost 15 percent. The direct method, on the other hand, had magnification factors between 0

and 1.0. Such values show that the direct method is relatively insensitive to measurement errors.

Since the apparatus developed in this project could measure the ball rebound velocity, the data revealed a discrepancy between the calculated value and the measured value. This discrepancy was the focus of phase three of the project. This discrepancy was analyzed by recreating the BPF test in an analytical model.

Two conjectures were tested with the simulation. The first conjecture attributed the discrepancy to deformation of the bat due to the impact. It was presumed that vibrations and material damping constituted a loss of energy. However, these forces were found to be internal, and therefore did not change the momentum of the system. The motion of the bat sections did exhibit high frequency but small amplitude oscillation about its radial center mass. Consequently, a rigid body assumption for the bat introduced transient errors in the calculation of the final angular momentum. But, the local displacements due to vibrations were small compared to the net angular rotation of the bat. Therefore using the angular displacement to calculate the velocity bypassed the transient errors associated with the oscillation of the velocity measurement.

The second conjecture attributed the error to dissipation through friction at the pivot. By experimentally determining the Coulomb friction coefficient and applying that pin friction to the pivot, it was verified by the simulation that friction could cause the discrepancy between the calculated and measured ball rebound velocity.

Application of the conservation of angular momentum equation to calculate the ball rebound velocity required that there be no external moments in the system. However, friction at the pivot acts as an external moment, retarding the motion of the recoiling bat. Consequently the system must be analyzed as an impulse-momentum problem. The impulse was the friction torque, which was proportional to the normal reaction force at the pivot. Furthermore, this reaction force was proportional to the square of the angular velocity of the bat. This fact explained why the error in the rebound velocity increased with increasing approach velocity.

The simulation also illustrated that calculating the BPF using the direct method minimized the error caused by friction. Because the friction affects the bat recoil velocity regardless of which method was used, using the bat recoil velocity to derive ball rebound velocity, as in the ASTM method, propagated the error. More specifically, adding friction to the model introduced a 7.10-percent error in the BPF using the ASTM method and only a 1.67-percent error using the direct method.

After determining that pivot friction was a significant contribution of the error in the BPF using the ASTM method, it is now possible to correct for that error. According to equation (3.6.1), correcting for the friction involves precise determination of the friction coefficient associated with the ball bearings at the pivot and precise measurement of the instantaneous angular velocity of the recoiling bat. This information would be used to determine the external moment term in equation (3.6.6).

Analysis of the discrepancies in the ASTM testing standard can be addressed in two ways. First, the direct method can be used in place of the ASTM method in calculating

the BPF. Alternatively, the ASTM method can be corrected by accurately characterizing the friction force.

REFERENCES

1. ASTM Designation: F 1890 - 98, *Standard Test Method for Measuring Softball Bat Performance Factor*, Annual Book of ASTM Standards.
2. *Balls and Strikes Softball: Online Edition*, "ASA To Begin Bat Testing in 2000," March 1999.
3. Cory, Stanley A., *Machine Design*, "The Nature of Linear Induction Motors", August 23, 1984 p111.
4. Denny, Pacific Machinery and Tool Steel, 3445 NW Luzon Street., Portland, OR 97210.
5. Editors of Modern Plastics Encyclopedia, *Guide to Plastics*, McGraw Hill, New York, 1979.
6. Fluid Technologies, www.fluidtechnologies.com/service_softballbat.html.
7. Air Oil Products Corporation, 2400 E Burnside, Portland, OR 97214, (503) 234-0866.
8. SMC Pneumatics, 14107 NE Airport Way, Portland, OR 97230.
9. Kraige, L.G. and J.L. Meriam, *Engineering Mechanics: Dynamics*, Fourth Edition, John Wiley and Sons, New York, 1997.
10. Mims, Forrest M. *Engineer's Mini Notebook Series*, Llh Technology, 1984.
11. Mooney, David A., *Mechanical Engineering Thermodynamics*, Prentice Hall, New Jersey, 1953.
12. Patent search engine, Delphion Incorporated, www.delphion.com/simple.
13. Parker Motion and Control, Pneumatic Cylinder Products, Catalog 0900P, Parker Hannifin Corporation, 1997.
14. Popov, Egor P., *Engineering Mechanics of Solids*, Prentice Hall, New Jersey, 1990.
15. Staff Reporter, *Machine Design*, "Linear Motors: simplicity motion," Penton Media, October 7, 1999 p135.

-
16. Staff Reporter, *Machine Design*, "Comparing the attributes of linear drives", Penton Media, February 11, 1999.
 17. Sun, C. T., Y. P. Lu, *Vibration Damping of Structural Elements*, Prentice Hall, New York, 1995.
 18. Zalud, Todd, *Machine Design*, "Blasting Speed into Amusement Park Rides," August 6, 1988 p58.